Structure-Function Relationships of Nanomaterials and Their Applications

For the Development of Sustainable Environmental Engineering

by

Ana Cecilia Barrios

A Dissertation Presented in Partial Fulfillment
of the Requirements for the Degree
Doctor of Philosophy

Approved March 2021 by the
Graduate Supervisory Committee:

François Perreault, Chair
Otakuye Conroy-Ben
Morteza Abbaszadegan
Qing Hua Wang

ARIZONA STATE UNIVERSITY

May 2021

ABSTRACT

This dissertation focuses on the structure-function relationships of nanomaterials (NMs) and some of their applications in environmental engineering. The aim is to investigate NMs of different surface chemistries and assess their interactions with biological models, evaluate the weathering impact and degradation parameters to improve polymer coatings, test their efficiency for contaminant removal and provide further understanding in the safe design of nanomaterials. Nanoecotoxicological risk assessment currently suffers from a lack of testing procedures adapted to nanomaterials. Graphene oxide (GO) is a carbon nanomaterial (CNM) that consists of a single layer of carbon atoms arranged in a hexagonal network. It is decorated with a high density of oxygen functional groups including epoxide and hydroxyl moieties on the basal planes and carboxylic and carbonyl groups at the edges. The changes in surface chemistry give GO unique properties that can be tailored for a function. Additionally, because of its simple synthesis and flexible chemistry, GO has been a popular building block of many composite CNMs. In environmental engineering, specifically, water treatment, GO has been studied by itself or as a composite for pollutant removal, biofouling reduction, and as an antimicrobial agent, just to name a few. Like GO, silver (Ag) is another NM widely used in water treatment for its biocidal properties. Despite the recent growth in this field, a fundamental understanding of the function-structure relationships in NMs is still progressing. Through a systematic set of experiments, the structure-properties-function and structure-properties-hazard relationships were investigated. These relationships can be used to establish guidelines to engineer “safe-by-design” functional nanomaterials, where materials are tailored to enhance their function while minimizing their inherent biological or environmental hazard.

DEDICATION

To my parents Sergio and Cecilia for supporting me through every crazy decision I have made and for being present every time I needed them.

To my siblings Brenda, Elena, and Sergio for their advice and constant uplifting. For believing in me even when I doubt myself.

ACKNOWLEDGMENTS

I would like to thank Dr. François Perreault for his mentorship and continuous support throughout my graduate studies at Arizona State University. I am very thankful that you stopped by my poster at that conference. It changed my life ever since. Thank you for all your positive energy and constructive feedback. I would also like to thank my committee members: Dr. Morteza Abbaszadegan for providing me with sound advice and one of the most incredible microbiology classes; Dr. Otakuye Conroy-Ben for always giving me someone to look up to and say “I want to be like her”; and Dr. Qing Hua-Wang for your energetic nature and friendly attitude, thank you for your support throughout these years.

I would also like to thank Arizona State University’s Fulton Schools of Engineering, the National Science Foundation’s Center for Nanotechnology-Enabled Water Treatment, the P.E.O. Sisterhood Arizona Chapter, and the Achievement Rewards for College Scientists Foundation for providing financial support and other opportunities throughout graduate school. Similarly, I thank Stan Klonowski for always making sure that I had everything I needed for my experiments and for helping me build various setups. This work would not have been completed without your help.

Even though it is me presenting this work, the truth is that I would not have succeeded without the love and support from my family, friends, and colleagues. It has been, at the end of the day, a group effort. I am thankful for having a very supportive family who I admire and love. I am thankful to all my colleagues and lab mates who have shared the struggles but also the rewards that come from graduate school. Thank you for providing a safe network where we can grow as individuals and professionals.

TABLE OF CONTENTS

Page

CHAPTER

CHAPTER Page

CHAPTER Page

APPENDIX

LIST OF TABLES

Table Page

Table Page

Table Page

LIST OF FIGURES

Figure Page

Figure Page

Figure Page

CHAPTER 1

INTRODUCTION

1.1. Nanotechnology and nanomaterials. The field of nanotechnology is one of the most popular areas for current research and development in basically all technical disciplines.[1] Nanomaterials (NMs), as defined by the National Nanotechnology Initiative includes any material with "dimensions between approximately 1 and 100 nanometers."[2] These materials exhibit different chemical and physical properties that can be tailored for multiple applications. Carbon is a great example of a material that once in the nanoscale, can form a wide range of structures with fundamentally different properties. Fullerenes, carbon nanotubes (CNTs), and graphene are all carbon nanomaterials (CNMs) with different structures that have outstanding features as promising materials for numerous applications fields.[3]

In water and wastewater treatment, for example, CNMs and metal nanoparticles (NPs), have drawn wide attention due to their small size and high surface area, thus giving them strong adsorption capacities and reactivity. In addition to CNMs, some of the most popular NPs in this field include silver NPs (Ag NPs), zinc (Zn) and zinc oxide (ZnO) NPs, titanium dioxide (TiO_2) NPs and iron oxide (Fe_2O_3) NPs,[4] all of which could be used as individual materials or as part of composites for the removal of pollutants,[5] heavy metals,[6] inorganic anions,[7] and inactivation of bacteria.[8,9]

Despite the fact that CNMs and NMs in general promote industrial progress in water treatment and other sectors, there are concerns about a potential environmental hazards and interactions of released NMs with living organisms with yet unknown consequences.[10] To overcome the concerns aforementioned, the rational chemical design of NMs has stimulated an impressive body of work in which the function and hazard of chemicals are decoupled at the molecular level.[11] This approach aims to differentiate between NMs' structures and properties that are related to both the material function and hazard as observed in figure 1.1.

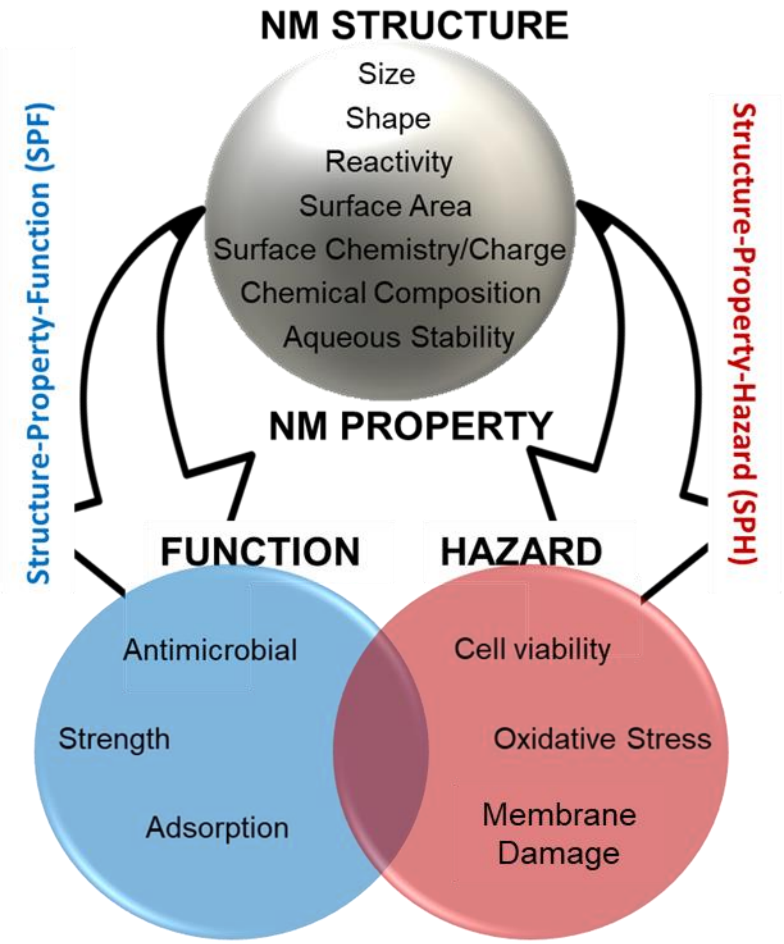

Figure 1.1. Schematic representation of parametric relationships between NM structure, physicochemical properties, and their functional performance and hazard profiles. The application of these design principles aims to maximize function and minimize hazard through rational design and control of nanomaterial structure. Figure adapted from Gilbertson et al. 2015.

Given the current state of knowledge and lack of established structure-property-function and structure-property-hazard relationships, the NMs' function and hazard cannot be differentiated by a given structure-property. However, as research progresses, we seek to resolve these relationships. If a specific structure-property is related to both the desired function and hazard, meaning there is an overlap between these parameters, then the goal is to manage the risk of these materials through exposure controls because the inherent nature of the NM will be toxic in order to perform as desired. However, if the desired application of that NM requires a hazard outcome (i.e., antibacterial applications), then, the established relationships are to be used to inform a rational design for that targeted hazard. In another scenario, if the function and hazard do not overlap, then the identified structure-property-function and structure-property-hazard relationships can be used to inform the design of NMs and nano-enabled products that meet their aimed objectives while decreasing their potential harm. In its majority, this dissertation will cover structure-property-function and structure-property-hazard relationships of graphene- and silver-based materials for environmental applications, with the goal to promote the sustainable design of NMs.

1.2. Structure-function relationships in graphene-based materials. Graphene-based materials are CNMs that are currently being investigated for environmental applications particularly in the water treatment, agriculture, and energy sectors.[10] Graphene (G), in its pristine form, consists of a single layer of carbon atoms arranged in a sp^2-bonded structure.[12] Upon chemical oxidation, graphene can be transformed into graphene oxide (GO). GO, is a sheet-like structure with a high density of oxygen functionalities including carboxyl, hydroxyl, epoxy, and carbonyl groups in the carbon lattice. There are, however, multiple methods to synthesize GO which yield different extents of oxidation on the material's surface.[13] Figure 1.2. shows different graphene-based materials and their structural differences and properties.

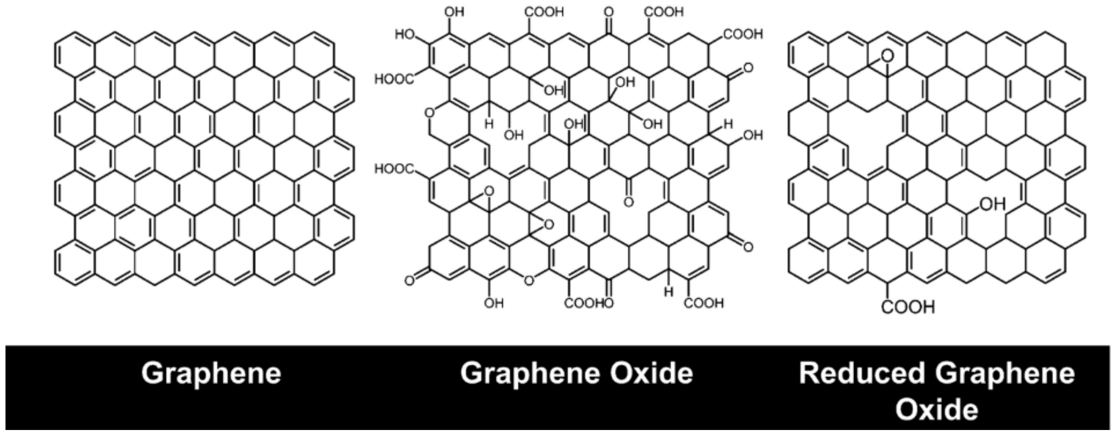

Figure 1.2. Overview of structurally different graphene-based NMs and some of their properties. Figure retrieved from Perreault et al.[12]

These differences alter the materials' interactions with biological models and their behavior in environmental matrices, thus influencing their applications. The oxygen functionalities in GO allow for rapid functionalization and the versatility and possibility of tuning the primary GO properties (flake size, quantity of functional groups) for desired applications. In environmental engineering, for example GO has been investigated for plant protection, its antimicrobial properties, environmental sensing, as a sorbent for pollutant removal, just to name a few. More applications and sectors are highlighted in Figure 1.3.

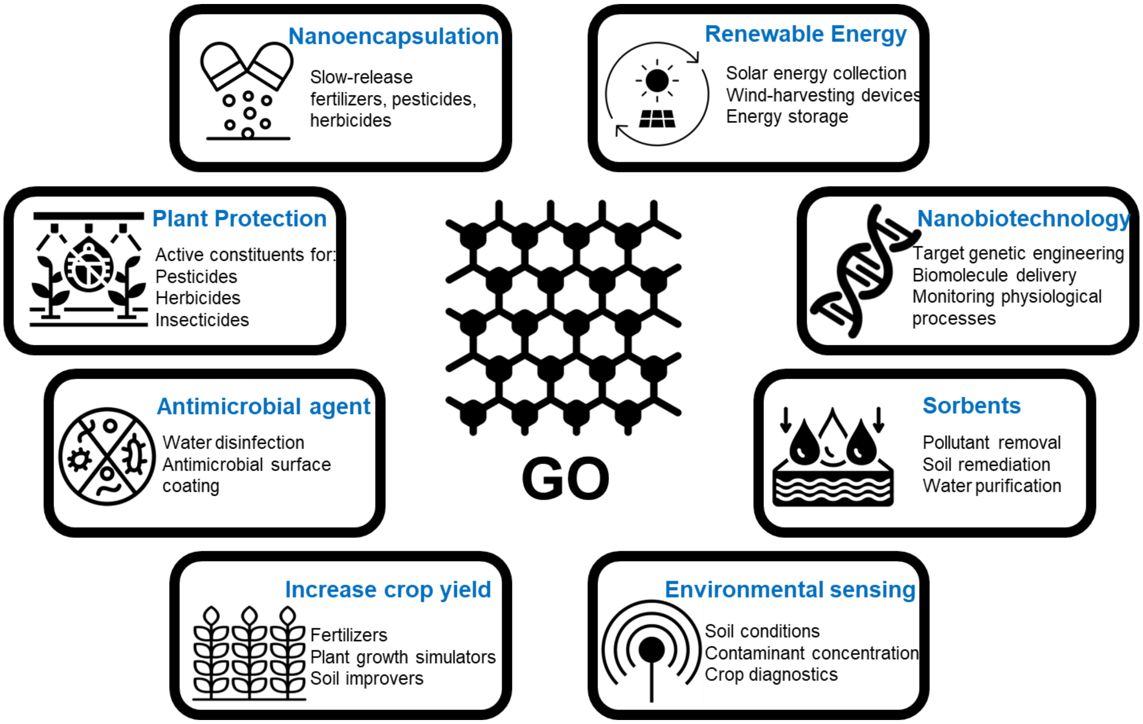

Figure 1.3. Potential graphene oxide applications in environmental engineering and agricultural sectors. Figure is adapted from Zaytseva et al.[10] and Perreault et al.[12]

1.2.1. Graphene-based materials as antimicrobial agents.

Amongst the many applications mentioned above, the antimicrobial properties of graphene-based NMs are widely studied.[14–16] Although the exact mechanism of bacterial inactivation by graphene and its derivatives is still a matter of investigation, several effects of graphene NMs have been proposed as possible pathways for antibacterial activity. These graphene-bacteria interactions include two main mechanisms: 1) physical mechanisms like sheet adsorption on the cell membrane’s surface or membrane puncturing and penetration through the lipid bilayer, and 2) chemical mechanisms like lipid extraction by the graphene sheets and oxidative stress generation as observed in Figure 1.4.

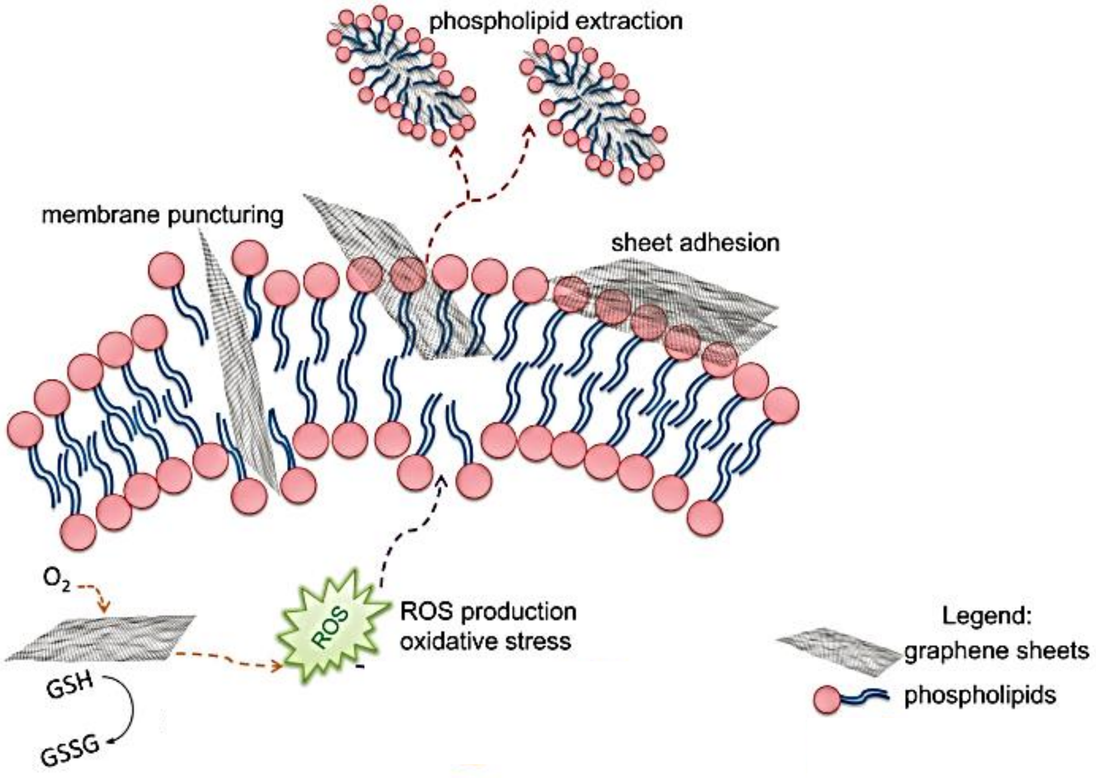

Figure 1.4. Mechanisms of cellular interactions of graphene-based NMs with bacteria. Bacterial inactivation by graphene-based NMs may involve direct puncturing of the cell membrane, generation of reactive oxygen species (ROS), extraction of phospholipids from the lipid bilayer, and adhesion of graphene sheets on the cell surface. Figure adapted from Perreault et al. [17]

1.3. Evaluating the structural differences of graphene-based NMs after heat, moisture, and UV exposure

1.3.1. Carbon nanomaterial/polymer nanocomposites. Polymer nanotechnology is a broad interdisciplinary area of research, development, and industrial activity, that involves the design, manufacture, processing, and application of polymer materials filled with NMs.[1] These NMs exploit novel properties and functions that occur at this scale because the high-surface-to-volume ratio enhances surface reactivity of the nanosized systems.

Polymers supplemented with CNMs are investigated for their antistatic, anticorrosion, and antifriction properties in paintings, coatings, and packaging.[18,19] The CNM/polymer composites can be altered over time by environmental conditions, changing their structural and surface properties.[20] Sunlight is known to result in the oxidation and degradation of polymers. This photodegradation is detrimental to the mechanical properties of a polymer and can lead to an early failure.[20] Thus, understanding the transformation of these polymeric materials is essential to predict their performance over time and service life. Polymers supplemented with graphite and GO have shown to significantly improve the electrical and mechanical properties of the composites.[21] The hydroxyl, carboxylic and/or epoxide groups in GO make it more reactive toward curing moieties in epoxy adhesive formulations.[22] Such functional groups can improve interactions between the GO nanosheets and polar groups of polymer chains.[23,24]

1.4. Applying the structure-function relationships of NMs in water treatment.

1.4.1. GO-silver composites for bromide removal. Brominated disinfection by-products (DBPs) are cytotoxic and genotoxic compounds formed during drinking water disinfection.[25,26] While they are known to be more toxic than chlorinated DBPs,[27] few water treatment systems target bromide (Br^-) removal due to poor selectivity and the interference of competing ions.[28] The available technologies able to remove Br^- typically require the implementation of new treatment systems and infrastructures, which come at high capital costs. For many utilities, high Br^- concentrations is a seasonal and temporary issue; as such, a flexible and easily adaptable solution that does not need specialized equipment is preferable. Previous studies have employed other carbon sorbents like granular and powdered activated carbon (GAC) or GO impregnated with silver ions (Ag^+) to remove Br^- from surface waters.[28,29] Ag^+ has been used mainly due to its high affinity to Br^- to form silver bromide salts ($k_{sp} = 5.2 \times 10^{-13}$). However, we believe that by using Ag NPs, the Br^- removal capacity can be increased due to their smaller size which enables a higher surface to volume ratio and more sorption sites to where the Br^- ions can adsorb. Additionally, using a carbon support (like GO) can provide higher NP stability and enhance Br^- removal.

The most common method of producing AgNPs is the chemical reduction of a silver salt (often $AgNO_3$) dissolved in water with a reducing agent such as sodium borohydride, citrate, glucose, hydrazine and ascorbate[30] There is, however, a wide array of different manufacturing methods (including spark discharging, electrochemical reduction, solution irradiation and cryochemical synthesis) some of which have been outlined by Marambio-Jones and Hoek.[30] In addition to different manufacturing methods, different capping or stabilizing agents may be used; these are generally used to prevent the AgNPs from aggregating or agglomerating.[31] The different synthesis methods usually result in Ag NPs with different particle sizes.

Current Br- removal technologies are often non-specific and costly due to the need of specialized equipment. Recently, the use of silver (Ag) to precipitate Br- as insoluble AgBr salts was proposed as an alternative to traditional adsorbents; however, the cost of Ag and competition from other ions reduce the applicability of silver for Br- removal. In this study, we report a new alternative: an Ag-impregnated graphene oxide (GO) nanocomposite that reduces the amount of silver needed for Br- removal. GO was impregnated with ionic Ag (GO-Ag^+) or nanoparticulate Ag (GO-nAg) to obtain two different nanocomposite materials and identify design properties that enhance the Br-removal efficiency.

1.4.3. Sulfidation of Ag NPs to reduce biofouling in reverse osmosis membranes. Biofouling involves the growth of biologically active structures called biofilms which pose operational and public health issues.[32] Reverse osmosis (RO) is a membrane separation technology used for desalination that encounters the formation of biofilms on the membrane's surface.[33] Like GO, one of the most popular applications for Ag NPs rely on their biocidal properties, which have been used in clothing, food packaging, or biomedical devices.[34] In water treatment, Ag NPs can also be used to reduce biofouling in membrane modules by incorporating them on or into the polymer matrix during or after membrane fabrication. [35,36] The mechanisms behind the Ag's biocidal properties are described below.

Silver as a biocide. The biocidal mechanisms of Ag at the macroscale are attributed to the release of Ag^+ and their interactions with various components of the microbe. For example, Ag^+ can interact with sulfhydryl groups on the cell surface, where the subsequent formation of the Ag-S bonds block respiration and electron transfer, leading to cell death.[37] Another Ag^+ toxicity mechanism relates to the ion's small radius (0.115 nm), which makes it possible for the ion to travel through transmembrane proteins such as porins (with pore sizes between 1-3 nm)[38] and once inside the cell, Ag^+ may react with thiol functional groups in proteins and nucleic acids, which interferes with DNA replication and leads to enzyme function deactivation.[34,37] Overall, Ag^+ increase oxidative damage by increasing the ROS levels inside the cell due to the deactivation of thiol-containing antioxidant enzymes, intensifying the damage done to proteins, lipids, and nucleic acids.

Ag NPs, compared to bulk Ag, display greater ion release per unit mass mainly due to an increased surface area to volume ratio. Yet, the precise mechanism(s) of Ag NPs toxicity remain uncertain, particularly the dynamic contribution of Ag as an ion or as a NP. There are three proposed mechanisms for Ag NPs biocidal properties: 1) Ag NPs are a Ag^+ reservoir which will passively be released and will induce antibacterial activity;[37,39,40] 2) the biocidal activity of Ag NPs is a result of particle effects only (i.e., physical disruption or alteration of the phospholipid cell membrane, generation of ROS) thus questioning the requirement of Ag^+ and their claim as the main agent of cellular impact;[37,40] or 3) a synergistic effect between the Ag^+ and the particle effect. In the literature reports, there is support for all three possibilities.[37]

One of the main limiting factors, however, is that Ag NPs tend to undergo rapid dissolution in aqueous environments and eventual depletion of Ag^+ from the surface may occur. Ag^+ has a very strong affinity to sulfur ions (S^{2-}), where Ag^+ reacts with inorganic sulfide to form Ag_2S (s). This interaction has also been observed for Ag NPs, where the elemental silver in Ag NPs is oxidized to Ag^+ and react with sulfide to form Ag_2S NPs or a core Ag NP with a Ag_2S shell.[41] Metal sulfidized NPs have been found in wastewater treatment biosolids, suggesting that Ag NPs that eventually enter the environment via sludge will be transformed into sulfidized of partially sulfidized particles.[42,43] While a number of studies have demonstrated that the toxicity of Ag NPs is decreased by sulfidation, no studies have focused on the effect of the extent of sulfidation in Ag NPs to slow down Ag^+ release or the impact on the biocidal properties of Ag NPs to reduce biofilm formation.

1.5. Overarching goal and research needs. Nanomaterials are being investigated to address challenges encountered by society in the fields of medicine, electronics and water treatment. The potential synthesis processes and functionalization opportunities in the nanotechnology field are endless, but this can lead to a misuse of materials and unrealistic applications. Additionally, the environmental impact associated with NMs could potentially offset the intended benefits. The overarching goal of evaluating the structure-function relationships of NMs, is to provide further understanding into the safe and sustainable design of nanomaterials based on their performance, and hazards to reduce their environmental impact. Additionally, further economic considerations regarding their production costs and applications are required.

1.6. Research questions and hypotheses.

The primary research questions and hypotheses addressed in this proposal are:

Questions:

Q1) What are the structure-property-hazard relationships that govern the chemical and biological reactivity of graphene oxide to bacteria? (CHAPTER 2)

Q2) Can the material properties and biological reactivity observed in bacteria be translated to other model organisms? (CHAPTER 3)

Q3) Does a graphene nanofiller result in less degradability by solar irradiation compared to oxidized GB NMs in an epoxy composite? (CHAPTER 4)

Q4) Can a graphene oxide – silver nanoparticle composite remove bromide more efficiently from complex water matrices than a graphene oxide-silver ion composite? (CHAPTER 5)

Q5) In a reverse osmosis membrane, can sulfidation of silver nanoparticles slow down the release of ions to reduce biofouling while maintaining the membranes performance? (CHAPTER 6)

Hypotheses:

H1) The material's surface chemistry plays a dominant role in GO-bacteria interactions. The GO with a more hydrophobic surface will enhance material-bacteria interactions whereas the more hydrophilic one reduces them.

H2) The GO interactions will differ amongst organisms due to the differences in aggregation kinetics that occur within each experimental media in addition to the inherent biological properties of each model.

H3) Incorporation of a graphene nanofiller into a polymer decreases the polymer matrix photodegradation due to graphene's higher photostability under UV exposure compared to a more oxidized GB NM

H4) Surface-mediated interactions between bromide and Ag NPs enhance bromide removal capacity in a size-dependent manner compared to ionic silver even in the presence of competing ions due to the NPs' high surface area.

H5) The solubility of silver nanoparticles can be reduced to slow down its depletion from the surface without impacting the anti-biofouling properties of the membrane.

1.7. Thesis Organization

Chapter 1 provides an overview of the different concepts covered throughout the proposal. It starts by introducing nanomaterials, particularly graphene-based materials and silver and their applications. Furthermore, it explores the structure-function relationships of nanomaterials and their importance in environmental engineering applications. Finally, it states the research questions, and hypotheses for each chapter in this proposal. The goal is to provide concise yet concrete information to help the reader familiarize with the studies done in each chapter.

Chapter 2 investigates the inherent properties of four GB-NMs to elucidate structure-property-hazard relationships. The chapter explores the interactions of four structurally different GO materials with *Escherichia coli (E. coli)*. The general antibacterial mechanisms of GO are described and tested. A dose-response curve was done to calculate the half maximum effective concentration (EC_{50}). The results demonstrate that at this biological endpoint, the extent of GO oxidation plays an important role in determining the GO-bacteria interactions. There was a linear relationship between carbon:oxygen ratio (C/O) and EC_{50}, indicating that the most oxidized GO caused the lowest toxicity to *E. coli*, whereas the most reduced GO was the most toxic. However, a GO-bacteria wrapping mechanism was demonstrated via microscopy studies that reveal an apparent toxicity exerted by GO that, when in contact with *E. coli* decreases cell viability but upon sonication, viability is restored.

Chapter 3 expands upon the structure-property-hazard relationships observed in Chapter 2 to test whether these relationships exist in other organisms. Chapter 3 then, explores the interactions of the GO materials tested in Chapter 2 with four model organisms: *E. coli*, *Microcystis aeruginosa*, *Scenedesmus obliquus*, and *Daphnia magna*. These organisms were chosen due to their different biological complexities and environmental relevance. The same biological endpoint, EC_{50} was determined after a set of dose-response experiments to evaluate the changes in GO-organism interaction. Findings in these studies reveal that the role of surface chemistry on the mechanisms of interaction with organisms of different biological complexity differ significantly. Upon comparisons between the bacteria and cyanobacteria models, which had the most contrasting EC_{50} and C/O relationships, results show oxidative stress generated by ARGO in bacteria and a decrease in metabolic activity in cyanobacteria. These differences emphasize the need to differentiate the safe-by-design guidelines made for GB NMs in relation to the potential organisms exposed.

Chapter 4 explores the other side of the structure-property relationships. Unlike Chapters 2 and 3, which focus on the structure-property-hazards. Chapter 4 focuses on the structure-property-function. This chapter investigates the ultraviolet (UV)-induced degradation of graphene-based/polymer nanocomposites with different surface chemistries. The nanocomposites were tested under four weathering conditions: Dry UV, Humid, UV, Dry Dark, and Humid Dark, utilizing the NIST SPHERE (Simulated Photodegradation via High Energy Radiant Emission), which accelerates outdoor weathering of test materials. UV radiation is one of the most common polymer degradation processes, upon supplementing a polymer with graphene-based materials, the service life of the polymer could be improved. By using GB NMs as "nanofillers" the barrier properties of the polymer matrix are enhanced, increasing the tortuous pathway by which gaseous photoproducts would be released after photodegradation. Results show that Humid UV and Dry UV conditions are detrimental to the neat epoxy composite as shown by an increase in gaseous photoproducts being released after 30 days of UV light exposure. GB NMs as fillers increase the photostability due to their ability to absorb UV light, with graphene being the most effective one compared to GO and RGO.

Chapter 5 explores the functionalization of three GO materials with silver ions (Ag^+) or silver nanoparticles (Ag NPs) for bromide removal. This is the first chapter dealing with the application of a GO based composite in water treatment while also dealing with the composites' optimization by attempting to establish structure-property-function relationships. The study focuses on the optimization of a GO-silver composite to remove Br^- from water reducing the formation of halogenated DBPs. Particle size, silver loading, and removal capacity were monitored throughout. The presence of silver as Ag NPs instead of ions is found to increase the selectivity towards bromide in the presence of competing ions. Results show that a GO support loaded with Ag NPs has a similar efficiency as Ag NPs at removing Br^- from water while having the lowest Ag remaining in the water after coagulation. Anoxic results confirm the higher removal efficiency of Ag NPs by removing the dissolution effect of Ag NPs in aerobic conditions, thus emphasizing the direct interaction between the Ag and the Br ions.

Chapter 6 is a perfect example of how a NM's structure can be engineered to reduce the inherent NM's hazard while optimizing its function for a particular application, thus combining both the hazard- and the function-property relationships. Chapter 6 investigates how sulfidation of Ag NPs reduce Ag leaching while retaining the performance of a reverse osmosis (RO) membrane. As another application for Ag as an antimicrobial agent, Ag NPs are ideal candidates to reduce biofouling in RO systems. However, one of the main challenges of Ag NPs is their rapid ion release to the water streams and the need to regenerate them upon membrane functionalization. Findings reveal that partial sulfidation of Ag NPs prepared *in-situ* create an external silver sulfide (Ag_2S) layer with a Ag core that allows for the slow release of silver ions while retaining Ag attached to the membrane, thus, improving the lifetime of the functionalized membrane. This study then, hopes to integrate the structure-property-hazards (inherent of the Ag NPs) with the structure-property-function by reducing the hazards while attempting to optimize those Ag NPs' properties for a particular function.

All references are located at the end of this thesis.

CHAPTER 2: STRUCTURE-PROPERTY-TOXICITY RELATIONSHIPS OF GRAPHENE OXIDE: ROLE OF SURFACE CHEMISTRY ON THE MECHANISMS OF INTERACTIONS WITH BACTERIA

Published in *Environmental Science & Technology*

Graphical Abstract

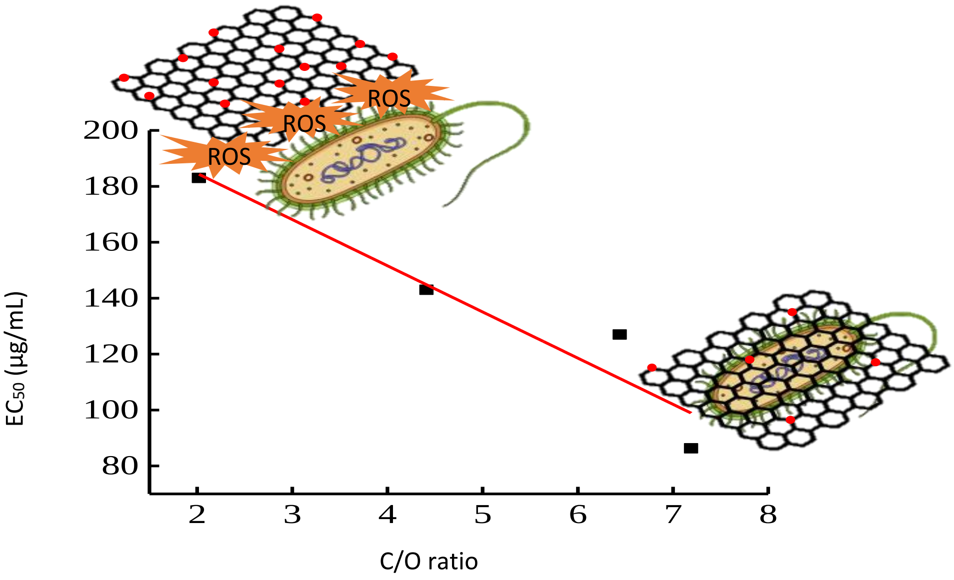

Abstract

Graphene oxide (GO) is an antimicrobial with tunable surface chemistry. To identify the physicochemical determinants of GO's antimicrobial activity, we generated different modified Hummer's GO materials thermally annealed at 200, 500, or 800 °C (TGO200, TGO500, and TGO800, respectively) to modify the surface oxygen groups on the material. Plating assays show that as received GO (ARGO) and TGO200, TGO500 and TGO800 reduce *E. coli* viability by 50% (EC_{50}) at 183, 143, 127 and 86 µg/mL, respectively, indicating higher bacterial toxicity as ARGO is reduced. To uncover the toxicity mechanism of GO, fluorescent dye-based assays were used to measure oxidative stress at the EC_{50}. ARGO showed an increase in intracellular reactive oxygen species (ROS), measured as an increase in 2',7'-dichlorodihydrofluorescein diacetate fluorescence, whereas TGO500 and TGO800 induced an increase in the fluorescence of fluorescein diacetate by 30 and 42%, suggesting a decrease in cell permeability. Due to a possible wrapping mechanism, plating assays after post-exposure sonication were performed to explain TGO's low oxidative response and high FDA levels. Results show no difference in colony forming units, indicating that cell entrapment and inhibition of cell growth by GO are present. By comparing different GO samples at their EC_{50}, this study reveals that reduction of GO alter both the mechanisms of cellular interaction and the degree of toxicity to bacteria.

2.1. Introduction

Carbon can take multiple allotrope forms, ranging from the three-dimensional diamond to the zero-dimensional fullerene; each with unique physicochemical properties.[44] Since the first isolation of graphene in 2004[45], a two-dimensional (2-D) allotrope of carbon, graphene has gained popularity due to its high electron mobility, thermal conductivity, mechanical strength, and surface area.[17,46] Graphene oxide (GO), the oxidized form of graphene, is a carbon nanomaterial (CNM) that consists of a single layer of carbon atoms arranged in a hexagonal network where most of the carbon atoms preserve sp^2 hybridization. It is decorated with a high density of oxygen functional groups including epoxide and hydroxyl moieties on the basal planes and carboxylic and carbonyl groups at the edges.[47] The presence of oxygen in the carbon structure greatly reduces the conductivity and mechanical properties of GO compared to graphene. However, because of its simple synthesis and flexible chemistry, GO has been a popular building block of many composite CNMs.[17]

In the last decade, several studies have shown the antimicrobial properties of GO when exposed to a wide array of microorganisms, including Gram-positive and –negative bacteria.[48–51] Multiple mechanisms are involved when bacterial cells come in contact with graphene-based materials i.e., membrane stress, oxidative stress, and/or wrapping isolation.[14,15,52] Each of these mechanisms can act independent of each other or together to inhibit bacterial growth through chemical or physical interactions.[15,52–55] Cellular injury might occur from the impact of physical membrane disruption, creating an irreversible destruction of the cells after exposure to CNMs.[54] The action of oxidative stress on bacteria results in the oxidation of lipids, nucleic acid and proteins which can eventually lead to cell membrane destruction and cellular growth inhibition through the generation of reactive oxygen species (ROS).[15] Lastly, bacterial cells can be biologically isolated from their growth medium when graphene sheets enclose them, thus preventing nutrient consumption and growth, leading to cell death.[56,57] However, cell inhibition by GO wrapping seems reversible and the viable cells may be recovered when separated from GO via sonication.[15,57]

The structure and surface chemistry of CNMs play an important role when determining their antimicrobial mechanism. Previous research on carbon nanotubes (CNTs) and fullerenes has demonstrated that their toxicity is linked to their physicochemical properties and changes in size, functionalization, and oxidation levels alter their toxicity potential.[58–62] Arias and Yang found that SWCNTs with hydroxyl and carboxylic surface groups exhibited stronger antimicrobial activities towards *Salmonella typhimurium*, *Bacillus subtilis*, and *Staphylococcus aureus* when compared to SWCNTs functionalized with amines.[63] Gilbertson et al. demonstrated that by manipulating the surface chemistry of MWCNTs, one can control the electrochemical and biological activities of the material.[58,62] Recently, multiple studies have focused on developing a framework that serve as guidelines for the sustainable selection and design of nanomaterials, including CNTs.[11,64–66]

Based on the synthesis method used, GO materials can have large differences in oxygen content, sheet size, morphology, hydrophilicity, and dispersibility[52] that may impact GO-bacteria interactions and consequently, GO’s toxicity towards microorganisms. When the effect of GO and reduced GO (RGO) (0-200 µg/mL) were compared using

Pseudomonas aeruginosa as a model organism, Gurunathan et al. observed a loss in cell viability in a dose- and time- dependent manner through the generation of ROS and a significant production of superoxide radical anion (O^{2-}).[54] A study by Liu et al. showed that a GO dispersion had the highest antibacterial activity towards *Escherichia coli* (*E. coli*) with 89.7% loss of viability at 40 µg/mL, followed by rGO, graphite, and graphite oxide. The toxicity was attributed to the smaller size of GO sheets compared to the other materials, as well as membrane and oxidative stress.[67] Similarly, Perreault et al. observed a 4-fold increase in the antimicrobial effect of a GO-coated surface when the sheet area decreased from 0.65 to 0.01 μm^2.[15] Additionally, Akhavan and Ghaderi showed that rGO nanowalls were more toxic towards both *E. coli* and *S. aureus* than the unreduced GO nanowalls where only 41% and 16% of the bacteria survived after 1h contact with GO and rGO nanowalls, respectively.[68] This effect was attributed to the better charge transfer between the bacteria and the sharper edges of the reduced nanowalls.[68] However, using lipid bilayers to study the interaction of 2-D nanomaterials with membranes, Zucker et al. showed that physical interactions leading to lipid extraction were more important than chemical mechanisms for membrane disruption.[69] Therefore, multiple studies related the material's structure to its antimicrobial potency, often with contradictory findings. A direct comparison between oxidized and reduced form of GO can be challenging because of the effect of GO's surface chemistry on aqueous stability, electron conductivity, and mechanical properties, all of which influence cellular interactions. As a result, how the properties of GO change the way this material interact with cells remains unresolved.

In this study, we investigate how changes in the surface chemistry of a modified Hummer's graphene oxide (ARGO) and thermally annealed GO (TGO200, 500, and 800) alter the mechanisms of antimicrobial activity towards *E. coli*. The dependency between oxygen content and antimicrobial activity is demonstrated by calculation of the effective concentration (EC_{50}). Then, by comparing materials on the same biological endpoint (i.e. EC_{50} concentration), the mechanisms involved in GO-bacteria interactions could be examined and explained using fluorescent-dye assays indicative of oxidative stress and membrane permeability. The findings in this study aim to highlight the antimicrobial properties and mechanisms of graphene-based materials, which can then provide insights into the safe design of CNMs through the establishment of relationships that relate the materials' chemical structure and properties to their function and inherent hazard.

2.2. Materials and Methods

2.2.1. Materials and Chemicals

2.2.1.1. Chemicals.

The fluorescent dyes: propidium iodide (PI) and SYTO® 9 (from the LIVE/DEAD™ *Bac*Light™ bacterial viability kit), BODIPY™ 493/503 (4,4-Difluoro-1,3,5,7,8-Pentamethyl-4-Bora-3a,4a-Diaza-*s*-Indacene), 2',7'-dichlorodihydrofluorescein diacetate (H_2DCFDA), and fluorescein diacetate (FDA) were obtained from Thermo Fisher Scientific (Molecular Probes, Eugene, OR). Unless specified, all chemicals were dissolved in deionized (DI) water obtained from a GenPure UV xCAD plus ultrapure water purification system (Thermo Scientific, Waltham, MA).

2.1.1.2. Graphene oxide (GO).

A modified Hummer's powdered single layer GO (~99% pure) was purchased from ACS Materials LLC (Medford, MA, USA, product no. GNOP10A5) and used as received (ARGO).

2.2.1.3. Thermally reduced GO (TGO).

Surface modification on the GO was prepared by thermally treating the ARGO under helium (He) gas flow in a tube furnace (Thermo Scientific Lindberg/Blue M TF55035A-1) with a custom-built quartz tube at increasing temperatures 200, 500, and 800 °C.[11] The ARGO was added to the quartz tube and heated at a rate of 5 °C min^{-1} to the maximum temperature, held for 30 min, and left to cool at room temperature under He flow. These thermally reduced GO samples are referred to as TGO200, TGO500, and TG800, respectively.

2.2.2. Material Characterization.

ARGO and TGOs were characterized using X-ray photoelectron spectroscopy (XPS) to quantify the surface chemistry and distribution of functional groups and scanning electron microscopy (SEM) to determine GO size flake. For XPS analysis, the sample holder was covered in double-sided copper tape and dusted with enough GO powdered material. The sample was then loaded into a Thermo Scientific ESCALAB 250Xi that uses a monochromatic Al Kα X-ray source with the following parameters: 1486.7 eV and a spot size of 650 μm. Survey spectra were collected using a 150 eV pass energy and a 1.0 eV step size. The high-resolution C 1s spectra was collected using a 50 eV pass energy and a 0.1 eV step size. Three measurements in different locations of each sample were collected.

The Thermo Scientific Avantage software was used for peak fitting and to calculate the atomic percentage.[11] SEM images were taken with an Amray 1910 FE-SEM using 10 eV. For sample preparation, 3 µL of a diluted 50 µg/mL GO stock solution was drop-casted on a 1 cm × 1 cm silicon wafer previously cleaned via UV-ozone treatment for 20 min (UV/Ozone ProCleaner, BioForce Nanosciences, Ames, IA).[15] The software ImageJ was used to process the SEM images and measure GO dimensions.

2.2.3. Antimicrobial Activity of GO in suspension.

Before the microbiological tests, all glassware and media were sterilized by autoclaving at 120 °C for 2 h. *Escherichia coli* W3110 (American Type Culture Collection ATCC 11303) were grown overnight in Lysogeny Broth (LB) at 37 °C on a shaker plate at 140 rpm in an Isotemp incubator (Fisher Scientific). This bacteria was selected for its wide applications in environmental engineering as a model indicator[70] and its well documented interactions with carbon nanomaterials, simplifying the comparison between previously published research and this study. The culture was then diluted in fresh LB (1:25) and grown under the same conditions until the optical density (OD) reached 1, indicating log phase (~2 h). Bacterial cells were washed by centrifugation three times with sterile 0.9% NaCl solution before being diluted to 10^7 colony-forming units (CFU)/mL in sterile saline solution.

For GO exposure to the bacteria, stock suspensions of ARGO and each TGO materials were made in nanopure water (5,000 µg/mL) and bath sonicated for 1 h (M3800 Branson Ultrasonic Corporation, Danbury, CT). In 7 mL scintillation vials, 3.5 mL of sterile 0.9% NaCl, 0.5 mL of clean bacteria solution and the required volume of each GO suspension were added to reach concentrations from 1, 10, 50, 150, 250, and 500 µg/mL in a total volume of 5 mL. For all experiments, a negative control (no GO added) treatment was created by adding 1 mL of sterile DI water. The positive control was prepared by adding 500 µL of a 50 mM $CuCl_2$ and 500 µL of sterile DI water for a total concentration of 5 mM $CuCl_2$ in a volume of 5 mL. $CuCl_2$ was used as a positive control because it is known to be an antimicrobial agent.[71] Vials were placed on a horizontal shaker (Branstead Lab-Line) at 80 rpm for 3 h and kept at room temperature. After the 3 h contact time, the bacteria-GO suspensions were diluted (1:10) in Eppendorf tubes, vortexed, and 50 µL of each suspension was spread on a LB agar plate and incubated overnight at 37 °C for CFU enumeration. To assess GO entrapment around bacteria cells, a post-sonication experiment was done. After the 3 h contact time and plating, each Eppendorf tube containing the diluted bacteria-GO suspension was bath sonicated for 10 min as previously described[57] and 50 µL of the suspension was immediately plated and incubated in the same conditions.

2.2.4. Effective concentration calculation.

The half maximum effective concentration (EC_{50}) was determined in OriginPro 8.5.1 software using a sigmoidal fit of the dose-response function with the equation[72]:

$$y = A1 + \frac{A2 - A1}{1 + 10^{(log_x 0 - x)p}} \tag{1}$$

Where A1 = bottom asymptote, A2 = top asymptote, $log_x 0$ = center, p = hill slope, and EC_{50} is given by:

$$EC_{50} = 10^{log_x 0} \tag{2}$$

2.2.5. Determination of Viable Cells after GO Exposure.

Cell viability in GO-bacteria suspensions was determined by LIVE/DEAD fluorescent staining. After the 3 h exposure time, cells were stained by adding 1 µL of 3.34 mM SYTO 9 and 1 µL of 20 µM propidium iodide (PI) to 1 mL of suspension.[15] The samples were incubated for 30 min in the dark before pipetting 5 uL of each sample in a microscope slide for epifluorescence microscopy. Ten pictures per replicate were taken with a Leica DM6 epifluorescence microscope (Leica Microsystems Inc. Buffalo Grove, IL). A visual confirmation of the association of *E. coli* with GO was obtained using SEM images with a JSM 6300 SEM (JEOL USA, Peabody, MA) operated at 15 kV and images were captured with an IXRF Systems model 500 digital processer (IXRF System Inc., Austin, TX). Briefly, for sample preparation, samples were suspended in 2% glutaraldehyde buffered with 0.1M sodium phosphate, pH 7.2 overnight at 4_oC and then washed 3x in the same buffer. Secondary fixation was done with 1% osmium tetroxide in buffer for 1h at room temperature. The samples were washed 3x with diH_2O and adhered to poly-lysine coated coverslips, then washed and treated with an ascending series of acetone solutions leading to complete dehydration. Critical-point drying was done with a CPD-020 unit (Balzers-Union, Principality of Liechtenstein) using liquid carbon dioxide. The dried samples on coverslips were mounted on aluminum stubs and coated with approx. 10-12nm of gold-palladium using a Hummer II sputter coater (Technics, San Jose, CA).

2.2.6. Esterase activity after GO Exposure.

Changes in esterase activity or membrane damage in GO-bacteria suspensions was estimated using the fluorescein diacetate (FDA) fluorescent dye.[73] Fluorescein diacetate is a non-polar ester that passes through cell membranes. Once inside the cell, FDA is hydrolyzed by esterase, an enzyme present in viable cells, to produce fluorescein, which accumulates inside the cell and fluoresces under UV light [74] T After the 3 h exposure time, cells were stained with 5 mM of FDA in 1 mL of GO-bacteria suspension. The samples were incubated for 30 min in the dark before pipetting 200 µL of each sample in a 96 well plate. The fluorescence was measured using an excitation wavelength of 490 nm and an emission wavelength of 526 nm. All the fluorescence data was collected using a fluorescence plate reader (Synergy H1, BioTek). Data was expressed as the mean fluorescence intensity and the results as a percentage with respect to the control.

2.2.7. Reactive Oxygen Species Generation after GO Exposure.

ROS formation was measured using the cell permeable indicator 2’,7’-dichlorodihydro fluorescein diacetate (H_2DCFDA).[75] Cellular esterases hydrolyze the probe to the non-fluorescent 2’,7’-dichlorodihydrofluorescein (H_2DCF), which is better retained in the cells. In the presence of ROS and cellular peroxidases, H_2DCF is transformed to the highly fluorescent 2’,7’-dichlorofluorescein (DCF). An H_2DCFDA stock solution (10 mM) was prepared in ethanol in the dark. After the 3 h exposure time, 1 mL of bacterial samples were exposed to 0.2 mM H_2DCFDA and incubated for 15 min in the dark before pipetting 200 µL of each sample in a 96 well plate. The DCF fluorescence was measured using an excitation wavelength of 495 nm and an emission wavelength of 527 nm.

2.2.8. Determination of Lipid Peroxidation after GO Exposure.

Lipid peroxidation was measured using the cell permeable indicator BODIPY^{TM} 493/503. After the 3 h exposure time, 1 mL of bacterial samples were exposed to 10 µL of a 2 mM BODIPY solution.[73] The samples were incubated for 30 min in the dark before pipetting 200 µL of each sample in a 96 well plate. The fluorescence was measured using an excitation wavelength of 488 nm and an emission wavelength of 510 nm.

2.2.9. Glutathione (GSH) Oxidation after GO Exposure.

Thiol concentration was quantified following Ellman's assay[76] as per previous studies.[11,15,58,59] GO dispersions of 50 µg/mL were prepared by bath sonication (VWR Aquasonic 150T) for 30 min in a 33 mM bicarbonate buffer with a pH of 8.6. A stock GSH solution was added to the triplicate samples to reach a final concentration of 0.4 mM. The samples were covered with aluminum foil to avoid oxidation induced by the light and placed on a rotator at room temperature until the experiment was done (6 h). An aliquot was removed at 0, 1, 2.5, 4, and 6 hours and filtered using a 0.22 µm syringe filter. Ellman's reagent (5,5'-dithiobis(2-nitrobenzoic acid), DTNB), which reacts with thiol groups of GSH to produce 3-thio-6-nitrobenzoate (TNB), was added. The absorbance was measured at 412 nm, using an extinction coefficient of 14150 $M^{-1}cm^{-1}$ and then used to calculate the concentration of GSH remaining in solution. The percent loss of GSH was calculated by comparing the results with the negative control (no GO).

2.2.10. Data Analysis and Statistics.

All treatments were prepared in triplicate and repeated at least in three independent experiments. Means and standard deviations were calculated for each treatment. Significant differences between control samples (no GO) and GO exposed bacterial samples were determined via a one-way analysis of variance (ANOVA), followed by a Tukey post-hoc test where a p value less than 0.05 was considered to be significant. Statistical analysis was done using the Statistical Package for Social Sciences (SPSS) software version 25.

2.3. Results and Discussion

2.3.1. Surface Chemistry Characterization of ARGO and TGOs.

The different GO materials were characterized by XPS to identify how the surface chemistry of GO influence the interactions of GO with bacteria. XPS offers a quantitative approach to evaluate the reduction degree of GO and the changes in types of oxygen functionalities as a function of thermal reduction. Table 2.1 shows the relative percentage of carbon, oxygen, and their different bonds for all samples. The relative percentage of carbon (C%) in all annealed materials increase significantly with increasing the annealing temperatures, and ranges from 66% to 83% from ARGO to TGO800, accompanying with a decrease of percent oxygen (O%) from 33% to 12%. The observed increase in C/O ratio confirms successful deoxygenation of the GO surface and indicates restoration of the conjugated carbon structure.[77]

Table 2.1. Compiled XPS data representing the atomic percent of the carbon and oxygen content and the C/O atomic ratio, determined from the component fitting of the C 1s envelope for ARGO and TGO samples. Different letters represent statistical significance between materials at $p \leq 0.05$ (n=3). Trace amounts of impurities were also found and compiled in Table S1.

Samples	ARGO	TGO200	TGO500	TGO800
C%	65.85 ± 0.80 ^{c}	80.36 ± 0.21 ^{b}	84.76 ± 1.39 ^{a}	83.30 ± 0.44 ^{a}
O%	32.53 ± 0.54 ^{a}	18.23 ± 0.10 ^{b}	13.16 ± 1.09 ^{c}	11.59 ± 0.18 ^{c}
C/O	2.02 ± 0.06 ^{c}	4.41 ± 0.03 ^{b}	6.48 ± 0.62 ^{a}	7.19 ± 0.11 ^{a}
%sp^2 C	37.23 ± 1.14	70.76 ± 0.01	75.75 ± 1.43	84.71 ± 0.22
%C-O	41.89 ± 0.66	18.35 ± 0.30	16.67 ± 1.62	9.09 ± 0.36
%C=O	15.66 ± 2.09	5.22 ± 0.08	5.06 ± 0.18	4.58 ± 0.37
%COOH	5.24 ± 0.29	5.68 ± 0.23	2.53 ± 0.01	1.62 ± 0.24

Moreover, peak deconvolution of the C1s spectra can determine the relative presence of different carbon-oxygen bonds in GO. The deconvolution of C1s results in four peaks approximately located at binding energies of 284.8, 286.3, 287.5, and 288.8 eV which are assigned to single and double carbon bonds (sp^2 C), epoxide and hydroxyl (C-O), carbonyl (C=O), and carboxylate (COOH) functional groups, respectively (Figure A.1.). The assignments and binding energies are in agreement with previous studies.[11,47,78–81] The content of C-O groups, including epoxide and hydroxyl groups on the GO basal plane, decreases from 41.89% for ARGO to 9.09% for TGO800 upon thermal annealing. This decrease can be attributed to the reduction of epoxide groups, which are the most abundant on GO surfaces[11,77] and lack chemical and thermal stability.[11] At higher temperatures (800°C), C-O bonding contributes the highest fraction (9.09%) compared to C=O and COOH (4.58 and 1.62%, respectively). This has been observed in previous studies and is attributed to the higher thermal stability of C-OH groups intercalated into graphene interlayers.[11,77] The C=O and COOH groups, which are mostly found in the edges of the GO structure, exhibit a steady decrease upon thermal reduction.

In addition to surface chemistry analyses, potential changes in the GO sheet size was evaluated due to its role in the antimicrobial activity of GO.[15,54,56,67] SEM imaging showed that thermal annealing of GO had no significant effect on the sheet size. The average lateral size of ARGO and TGO800 were 1.19 ± 0.71 and 1.11 ± 0.74 µm, respectively. The size and image processing was done using ImageJ and is based on analysis of approximately 100 sheets captured from multiple images (Figure A.2).

2.3.2. Antimicrobial Activity of ARGO and TGOs Relates to Surface Chemistry.

The antimicrobial properties of as received GO and thermally annealed GO were assessed by mixing *E. coli* with GO suspensions of concentrations ranging from 0 to 500 µg/mL for 3h. A reduction of bacterial cell viability was observed at the lower concentrations, followed by a significant decrease at higher concentrations when compared to control ($p<0.05$). Figure 2.1.a shows that all materials inhibit 50% of the bacterial growth

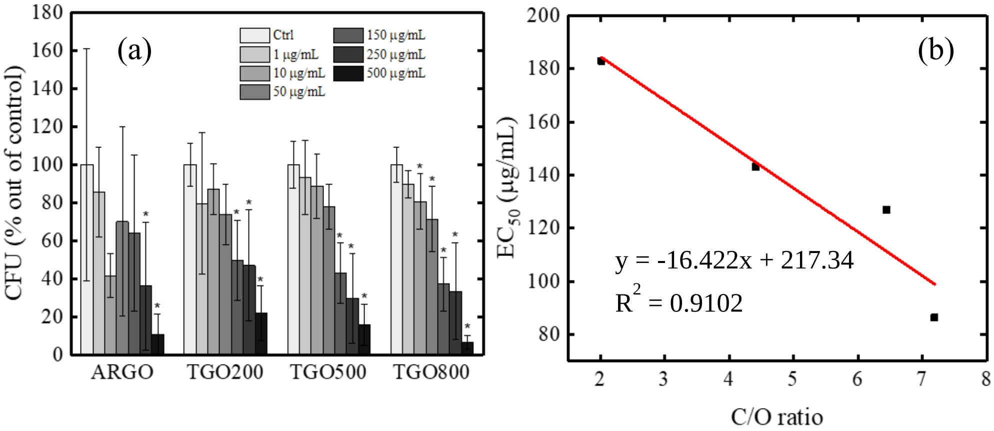

Figure 2. 1. Antimicrobial activity of GO to *E. coli*. A) Plating assay results after 3h of contact time between GO and *E. coli* using 0-500 µg/mL of material. B) Linear fit of EC_{50} values of ARGO and annealed GO and C/O ratios. Stars (*) represent statistical difference with respect to control. All experiments are compared to the negative control (no GO) whereas the positive control ($CuCl_2$) is not shown because there was no bacteria growth (n=9).

at different concentrations. From the dose-response data collected, the EC_{50} values were determined to be 183 ± 33.9, 143 ± 24.8, 127 ± 11.0, and 86.3 ± 28.9 µg/mL for ARGO, TGO200, TGO500 and TGO800, respectively.

These results indicate that the antibacterial activity of these materials are in the order of TGO800>TGO500>TGO200>ARGO, where TGO800 shows the highest toxicity and ARGO the lowest. The sigmoidal dose-response curves using both average values and individual data points are depicted in Figure A.3. These results exhibit a statistical difference between the EC_{50} values of all the thermally annealed materials compared to ARGO (Table A.2). Additional statistical information and other parameters are shown in Table S3. The difference in antimicrobial properties can be attributed to the extent of oxidation of each of the materials. ARGO has the lowest extent of oxidation with a C/O ratio of 2.02 and the highest EC_{50} value; whereas TGO800 has the opposite trend with the highest C/O ratio of 7.19 and lowest EC_{50} value. The relationship between these two parameters is observed in Figure 2.1.b with an R^2 value of 0.9102. There is a linear decrease in the EC_{50} value as the material is reduced indicating an increased inherent hazard.

Previous studies have shown that surface modification can play a role when determining the antimicrobial activity of GO. Akhavan and Ghaderi compared the toxicity of GO and rGO, where it was observed that rGO was a stronger antimicrobial against *E. coli* and *S. aureus*.[68] Similarly, in a later study, they found that rGO prevented the proliferation of *E. coli*, whereas GO was biocompatible with the microorganism.[57,82] The GO antimicrobial activities can be subject to the changes in oxygen-containing groups, which can alter the GO surface and edges. The relationship of EC_{50} values and other surface functional groups were investigated and can be observed in Figure S4. Both the basal groups (%C-O) and the edge groups (%C=O and %COOH) appear to influence the antimicrobial activity. In both cases, there is a strong linear increase with R^2 values >0.85 where the antimicrobial potency decreases as the percent of functional groups increases. These functional groups can affect bacterial interactions in two different ways. The more hydrophobic nature of annealed GO increases the microbe-GO interactions by decreasing the dispersibility of the materials[83], while removing oxygen functionalities on the edges and basal planes can enhance electron transfer capacity and antibacterial activity. These reduced GOs also introduce holes or defects in the carbon lattice due to CO and/or CO_2 liberation, and reduce surface charge and water dispersibility.[11,83] It is important to note that, although size plays a role in the GO's toxicity mechanisms as described in previous studies[15,56], ARGO and TGOs had a very similar lateral size and it did not play a significant role when assessing the toxicity of the materials in this study.

2.3.3. Oxidative Stress Generated by ARGO and TGOs.

The antimicrobial activity of GO can be mediated by both physical and chemical interactions that promote direct contact between the GO sheets and the bacterial cells.[15,17,84] The cell membrane is considered as the main target in these interactions. According to previous studies, oxidative stress is considered the dominant mechanism of toxicity for graphene based nanomaterials; however, other studies in bacteria or lipid bilayer models emphasize physical mechanisms over chemical ones.[50,83,85] Most graphene toxicity studies rely on testing multiple concentrations of GO/rGO and examining the biological response towards them (i.e., ROS generation, loss of glutathione). In this study, different fluorescent dye assays were performed at the EC_{50} concentration for each material to better understand the mechanisms of GO interaction with bacteria. This approach integrates any potential

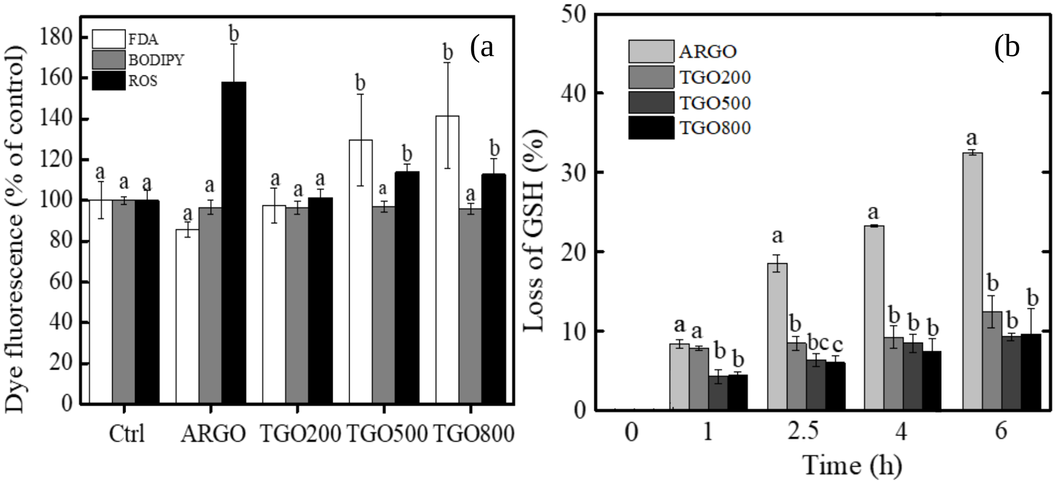

Figure 2.2. Biochemical response of ARGO and annealed GO in *E. coli* after 3h of exposure at the EC_{50} concentration. A) Fluorescent dye assays showing esterase activity, lipid peroxidation, and ROS generation. A 5 mM $CuCl_2$ was used as a positive control depicted as (+) whereas the negative control (Ctrl) had no GO). B) Time-dependent GSH oxidation mediated by GO materials. The mass loading of the materials is 50 µg/mL. Different letters represent statistical difference at $p \leq 0.05$ when compared to the control (n=9). All experiments are compared to the negative control (no GO).

effects of colloidal stability or hydrophobicity of the different materials by comparing them at the same biological endpoint, the EC_{50}, to better resolve the mechanisms of GO-cell interactions at the concentration where 50% of bacterial cells elucidate a response (in this case a reduction in cell viability) regardless of the material's surface chemistry.

The oxidative stress mechanism is often mediated by the generation of ROS upon bacteria-GO contact. An overproduction of ROS can cause the cells to enter a state of oxidative stress that results in damage to cellular components like proteins, lipids, and nucleic acids.[86] In this study, ROS generation was tested using a dichlorofluorescein fluorescent probe (H_2DCFDA), which is a general oxidative stress indicator and is sensitive to a wide range of free radical oxidizing species.[87] As shown in Figure 2.2.a, ARGO, TGO500, and TGO800 increase intracellular ROS formation, as shown by 58, 14, and 13% increase in H_2DCFDA, respectively, compared to the control. Even though the annealed materials TGO500 and TGO800 had an increase in ROS, the higher ROS generation by ARGO suggests that the more oxidized the material, the higher its capacity to induce oxidative stress. Lipid peroxidation levels were measured as a biomarker to further assess oxidative stress using the BODIPY dye. However, none of the materials induced an increase of peroxidase levels when compared to the control. This discrepancy between ROS generation and lipid peroxidation suggests that although ROS formation was induced by GO exposure, the oxidative stress resulting from this exposure was either mild or targeting cellular components other than lipids.

The esterase activity responses of *E. coli* after ARGO and TGOs exposure were quantified and are shown in Figure 2.2.a. After a 3 h GO exposure, there is an increase in esterase activity in the two most reduced materials TGO500 and TGO800 by 30 and 42%, respectively. Increase in FDA fluorescence may be attributed to an increase in intracellular FDA concentration, which can be the result of membrane hyperpolarization[88,89] induced by the interactions between nanomaterials and the cell surface,[90] or an increase in dye retention due to a decrease in cell permeability in GO-covered bacterial cells. These results suggest a possible cell wrapping mechanism for the annealed GOs (TGO500 and TGO800), as observed in previous studies.[15,57,91] A comparison of all the dyes with both the positive control (5 mM $CuCl_2$) and the negative control (no material) is shown in Table A.4.

Glutathione oxidation serves as another way to corroborate cellular oxidative stress. GSH is the most abundant low molecular weight antioxidant synthesized in cells and plays a role in keeping an intracellular oxidative equilibrium. The acellular oxidation of GSH was tested to investigate the oxidative potential of the materials. As shown in Figure 2.2.b, the loss of GSH was measured after GSH was exposed to the GO materials at different time intervals (0-6 h). The extent of reduction of the materials influenced the GSH oxidation response. For ARGO, the most oxidized material, GSH oxidation increased from 8 to 33% after 6 h of exposure. In comparison, at 6 h exposure, the TGO materials resulted in 12, 9.6 and 9.3% GSH oxidation for TGO200, TGO500, and TGO800, respectively. The higher GSH oxidation by ARGO indicates that this material has a higher biological reactivity when compared to all TGOs even after 1 h of exposure. This change can be attributed to the higher amount of surface oxygen in ARGO. In the basal plane of GO, carbon atoms bonded with C-O-C and C-OH groups decrease from 41.89% for ARGO to 9.09% for TGO800 upon thermal annealing, which translates to a greater defect density in

ARGO compared to the TGO samples. Additionally, an increase in %O enhances ARGO's dispersion in water (more active sites available) and it has an abundance of epoxy (C-O-C) groups, which are very reactive.[11] Previous studies have linked a higher GSH oxidation to defect density or oxidation debris in graphene materials.[11,15,55,92] ARGO, with a highly oxidized surface, facilitates the adsorption of oxygen on defect sites, generating surface oxides and eventually releasing ROS like peroxide (H_2O_2) or superoxide (O_2^-), promoting GSH oxidation.[11,15,54,93]

Oxidative stress generated by ARGO and TGO materials have distinct responses related to their surface chemistry and oxidation extent. On one hand, the most oxidized material, ARGO, leads to the highest oxidative potential demonstrated by the highest ROS generation and GSH oxidation. Higher defect densities in ARGO may explain its higher oxidative potential. These results suggest that chemical interactions between ARGO and *E. coli* are more important in oxidized GO materials. On the other, the thermally annealed GOs, particularly TGO500 and TGO800, have a higher wrapping capacity than ARGO and TGO200 by decreasing cell permeability, which suggests that a physical mechanism is the dominant mode of interaction. Although GO-bacteria interactions have been studied under various experimental conditions in previous studies,[51,68,92,94,95] this is the first study that reveals a shift in mechanism as the material's surface chemistry changes from oxidized to reduced graphene.

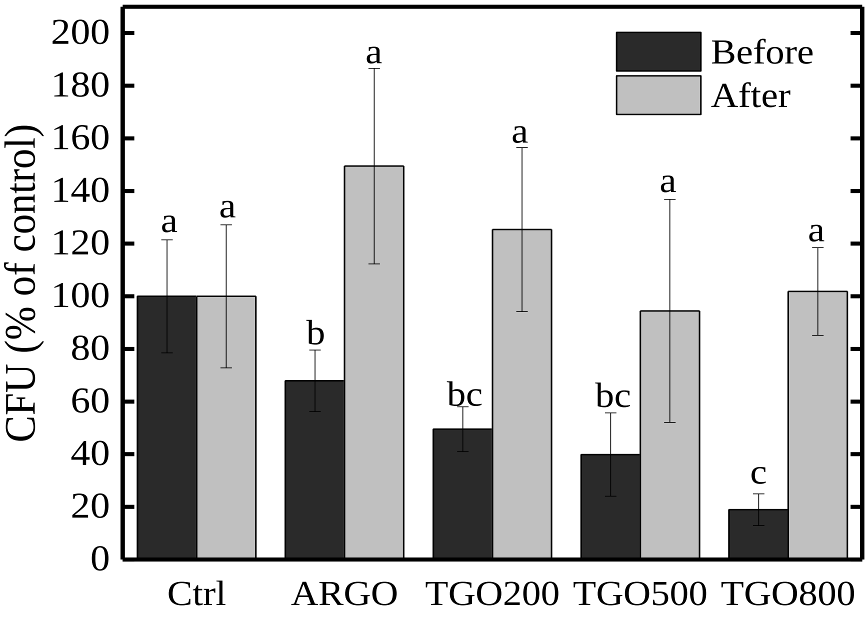

Figure 2.3. Viable colony forming units (CFU) count for E. coli after 3h of exposure to GO sheets, before and after bath sonication. Plating assay results using the EC_{50} concentration of each material before and after 10 min of bath sonication. Different letters represent statistical difference between materials at $p \leq 0.05$ (n=9). All experiments are compared to the negative control (no GO).

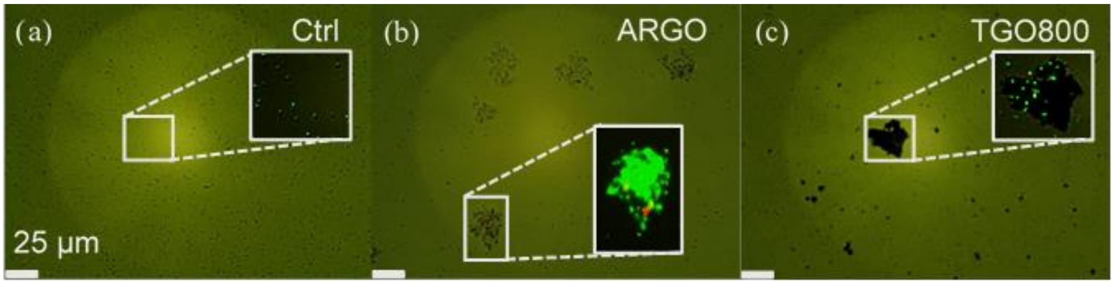

Figure 2. 4. GO-bacteria interaction. A-C) Representative epifluorescence microscopy images of E. coli cells after 3 h of exposure to no GO (ctrl), and 250 μg/mL of ARGO and TGO800, respectively. Main panels show bright field microscopy mode and the close-up panels show fluorescent mode using the green and red fluorescent channels. 1×10^8 cells/mL were stained with Syto9 and propidium iodide (PI) to show live (green) and dead (red) cells, respectively.

2.3.4. Mechanism of Interaction between ARGO and TGOs towards *E. coli*.

The antimicrobial properties of GO are attributed to a combination of mechanisms as explained in the previous section. A post-exposure sonication experiment was done to examine the possibility of a wrapping mechanism between GO and bacteria. Figure 2.3.shows cell viability after *E. coli* was exposed for 3 h to ARGO and TGOs in suspension at their EC_{50} values. As expected, all materials decrease the CFU counts significantly with respect to control (dark gray columns). In contrast, after 10 min of bath sonication and immediate re-plating, results reveal no significant changes in cell viability with respect to the control.

To confirm this observation, SEM and epifluorescence microscopy were done to assess cell viability. Figure 2.4.a-c show representative epifluorescent micrographs of *E. coli* stained with Syto9 and PI to show live and dead cells, respectively. As expected, the control sample had only viable cells represented in green bright fluorescent spots (Figure 2.4.a). After exposure to ARGO, it is observed that most of the cells are viable, with only a few dead cells (red spot), and more importantly, cells are present all over the ARGO sheets and somewhat "adsorbed' by the material. This is exemplified in the zoomed-in panel in Figure 2.4.b where cells are present where ARGO is present. Moreover, after exposure to TGO800, *E. coli* cells remain viable and in close contact with the material. Similarly, SEM micrographs support the adsorption abilities of GO towards E. coli as observed in Figure A.5.(a-b). The two panels show bacteria cells in contact with well-distinguished ARGO and TGO800 sheets, respectively. Results indicate that the bacteria is trapped or adsorbed by both materials with no major physical disruption of the cell.

Interestingly, ARGO and TGO800 have different morphologies, whereas ARGO is lighter and more porous and stable in aqueous solutions, TGO800 looks darker and aggregates easier which may alter GO-bacteria interactions.

In the literature, the cell recovery is attributed to a wrapping mechanism that occurs when GO sheets act as a flexible blanket that can cover the microorganisms. This effect can isolate microorganisms from the external environment, limit access to nutrients, and prevent proliferation.[57] Cell entrapment in GO sheets was first reported by Akhavan et al. where they showed that *E. coli* cells could be reactivated via a mechanical separation of the sheets using sonication.[57] Liu et al.[56] have shown that sheet size impacts GO wrapping around bacteria: large GO sheets completely covered *E. coli* cells and prevented bacteria proliferation, whereas small GO sheets did not fully cover the cells and allowed nutrient transport. Similarly, Perreault et al.[15] observed that the number of viable cells decreased from 55 to 0.5% when the GO sheet area increased. They also observed that GO, when coated on a surface, has a different antimicrobial potency than when applied in suspension; thus, sheet orientation and way of exposure (dispersion vs. static) can also impact the GO-bacteria interactions.[15,85,96–99] If the GO orientation is orthogonal with respect to the bacteria; the sharp edges of GO can penetrate the cells. However, the wrapping mechanism of GO towards bacteria might require stronger interactions with GO basal planes.[96,98]

2.4. Conclusion

The surface chemistry of GO was found to have an important influence on its antimicrobial activity. Highly oxidized GO generated the highest response from intracellular ROS and loss of glutathione, suggesting a chemically driven GO-microbe interaction. However, the EC_{50} value decreases as the oxygen content of the material decrease in thermally annealed GOs. The lower defects in their carbon surface, despite lowering ROS formation in the cell, promotes a trapping mechanism where TGOs adsorb bacteria cells, reduce cell permeability, and prevent them from proliferating. These findings reveal an important shift in mechanism upon changes in the surface chemistry of GO-based materials, with physically dominated interactions as the oxygen content decreases. This new understanding of the biological interactions of GO sheets with bacteria provides useful guidelines to tailor the function of GO materials based on its chemical composition.

Supporting Information

Impurities in ARGO and TGOs (Table S1); XPS peak deconvolution of ARGO and TGOs (Figure S1); EC_{50} values of ARGO and TGOs (Table S2); Statistical data and parameters of ARGO and TGOs after Sigmoidal dose-response fit (Table S3); Dye fluorescence of FDA, BODIPY and ROS with statistical data (Table S4); SEM micrographs and size distribution histograms of ARGO and TGO800 (Figure S2); Sigmoidal fit of dose-response curves for ARGO and TGOs (Figure S2); and linear fit of EC_{50} values for ARGO and TGOs with respect to oxygen functional groups (Figure S4). Epifluorescence micrographs of *E. coli* cells exposed to ARGO and TGO800 (Figure S5). This material is available free of charge via the Internet at http://pubs.acs.org.

Acknowledgements

This work was supported by the National Science Foundation through the CBET-1708681 award and the Nanosystems Engineering Research Center for Nanotechnology-Enabled Water Treatment (EEC-1449500). A.B. acknowledges the support of a Dean's Fellowship from the Ira A. Fulton Schools of Engineering and a Scholar Award given by the International Chapter of the P.E.O. Sisterhood. The authors gratefully acknowledge the use of the characterization facilities within the Electron Microscopy division of the CLAS Bioimaging Facility at ASU, particularly Dr. David Lowry for his help with the TEM images.

CHAPTER 3: A MULTISPECIES ANALYSIS OF THE RELATIONSHIP BETWEEN OXYGEN CONTENT AND TOXICITY IN GRAPHENE OXIDE

Graphical Abstract

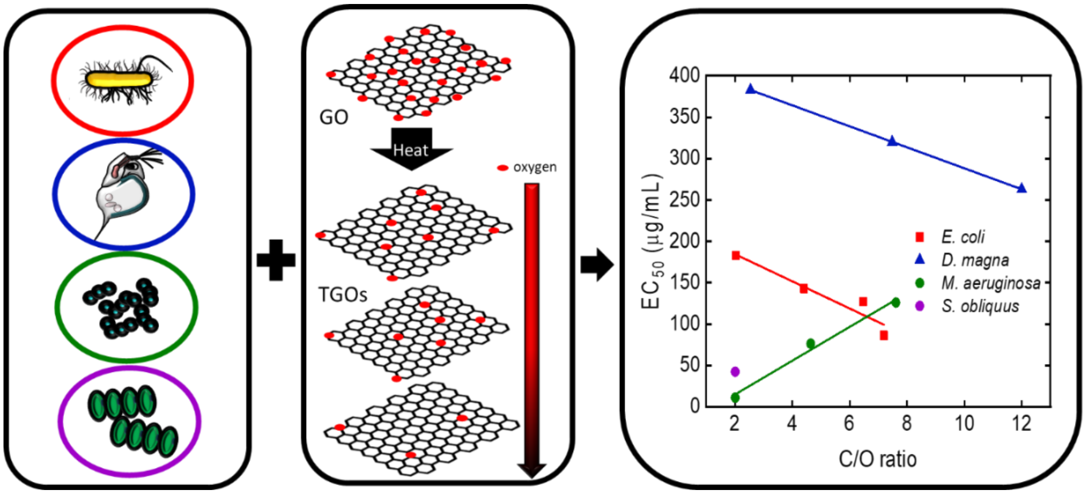

Abstract

The toxicity of graphene oxide (GO) has been documented for multiple species. However, GO has variable surface chemistry, and it is currently unclear whether changes in oxygen content impact GO-organism interactions the same way across species. In this study, a modified Hummer's GO (ARGO) was systematically reduced by thermal annealing at 200, 500, or 800 ºC and toxicity towards bacteria (*Escherichia coli*), alga (*Scenedesmus obliquus*), cyanobacteria (*Microcystis aeruginosa*), and invertebrates (*Daphnia magna*) was assessed by measuring the effective concentrations inducing 50% inhibition (EC_{50}). The EC_{50}-carbon/oxygen ratio relationships show similar trends for bacteria and invertebrates, where toxicity increases as the material is reduced. Conversely, cyanobacterial inhibition decreases as GO is reduced. Further testing supports differences in cell-GO interactions between bacteria and cyanobacteria. Cyanobacteria showed a decrease in metabolic activity, evidenced by a 69% reduction in esterase activity, after ARGO exposure but no oxidative stress, measured by 2',7'-dichlorodihydrofluorescein diacetate (H_2DCFDA) fluorescence and catalase activity. In contrast, ARGO induced a 55% increase in H_2DCFDA fluorescence and 342% increase in catalase activity in bacteria. The differences in GO toxicity observed in different organisms emphasize the need to differentiate the safe-by-design guidelines made for GO in relation to the potential organisms exposed.

3.1. Introduction

Carbon nanomaterials (CNMs) have gained popularity due to their unique electrical, optical, and mechanical properties, leading to their widespread use in all fields of technology, from electronic systems to biomedical devices.[17,100,101]A class of CNMs that has been growing significantly due to the increasing number of applications is graphene-based nanomaterials (GBNMs). Their popularity is such that in 2019, the global graphene market size was estimated at 78.7 million USD and is expected to expand at a compound annual growth rate of 38.7% in the next 7 years.[102] These GBNMS include graphene, graphene oxide (GO) and their derivatives. Graphene oxide (GO) is a highly oxidized, monolayer CNM characterized by the presence of hydroxyl, epoxy, and carboxyl functionalities along the basal plane or the edges of the graphenic structure, typically resulting in carbon to oxygen ratios (C/O) between 2-4.[103,104] GO is hydrophilic and can be easily dispersed in polar solvents (i.e., water) as opposed to graphene, which has no oxygen functionalities and is hydrophobic. Reduced GO's (rGO) properties lie somewhere in between, with fewer oxygen functional groups on the carbon lattice yielding C/O ratios above 8.[17]

The wide production and application of GBNMs inevitably raised concerns regarding the potential to impart adverse consequences in the event of the unintended release to aquatic ecosystems.[11,105,106] The structural changes described above significantly alter the stability of GBNMs in complex environmental matrices and their interactions with microorganisms. GO has been reported to cause acute toxicity to multiple aquatic organisms including bacteria,[85,107,108] protozoans,[109] zooplankton,[110] adult zebrafishes,[111] zebrafish embryos,[112,113] bivalves,[114,115] algae,[105,116,117] and invertebrates.[117–119] The mechanisms of interaction of GO with these different organisms have been described either as physical or chemical interactions, leading to membrane damage, cell entrapment, or oxidative stress.[48,50] However, the dominant toxicity mechanisms and material-organism interactions remain unclear and require further investigation.

Previous studies have shown that surface chemistry and presence or absence of functional moieties in CNMs play an important role in establishing their biological activities.[11,49,62,66,120,121] Gilbertson et al. for example, demonstrated the ability to control the biological activities of oxygen functionalized multi-walled carbon nanotubes (O-MWCNTs), another type of CNMs, by controlling their surface chemistry with either strong acids or high temperature annealing.[58,62] In a similar study, Wang et al. performed a systematic reduction of GO materials through thermal annealing to vary the C/O ratio from 1.58 to 5.80 to further understand the relationships that correlate the materials' properties to both their performance and inherent hazards.[11]

Given the wide diversity in GBNMs' structure, morphology, and composition, it is of upmost importance to understand the structure-activity relationships that underline the potential toxicity of nanomaterials (NMs). Unraveling how changes in the structural or morphological properties of GBNMs can affect their interactions with living cells will help us estimate the biological hazard and subsequent risk of new NMs. With this in mind, we recently investigated the structure-property-toxicity relationships for a suite of GO materials, systematically reduced using thermal annealing, in a bacterial model, *Escherichia coli* (*E. coli*). This previous study demonstrated higher bacterial toxicity as

GO is reduced, with lower effective concentration inducing 50% decrease in bacteria viability (EC_{50}) as the C/O ratio increased.[120] This structure-property-toxicity relationship, however, was only demonstrated in bacteria, which is one type of microorganism present in aquatic environments. Whether the same responses can be translated to other aquatic organisms or not is still unknown.

In this study, we compare how the differences in oxygen content of a modified Hummer's GO (ARGO) and three thermally annealed GOs (TGO200, 500, and 800) alter the toxicity towards multiple aquatic species including a bacterium, a green alga, a cyanobacterium, and an invertebrate. The selected model organisms are *E. coli, Scenedesmus obliquus (S. obliquus), Microcystis aeruginosa (M. aeruginosa*) and *Daphnia magna (D. magna*), which are all organisms that are commonly used for aquatic risk assessment thanks to their sensitivity, ecological relevancy, and short generation spans.[122] With this suite of biological assays, we show that the structure-property-toxicity relationships established in one model may not always be applicable to other organisms due to the differences in the model-specific mechanisms of interactions involved.

3.2. Materials and methods

3.2.1. Chemicals.

All the fluorescent dyes were obtained from Thermo Fisher Scientific (Molecular Probes, Eugene, OR). The dyes include fluorescein diacetate (FDA), and 2',7'-dichlorodihydrofluorescein diacetate (H_2DCFDA). Unless specified, all chemicals were dissolved in deionized (DI) water obtained from a GenPure UV xCAD plus ultrapure water purification system (Thermo Scientific, Waltham, MA). A modified Hummer's powdered single layer GO (~99% pure) was purchased from ACS Materials LLC (Medford, MA, USA, product no. GNOP10A5) and used as received (ARGO). Surface modification on the GO was prepared by thermally treating the ARGO under helium (He) gas flow in a tube furnace (Thermo Scientific Lindberg/Blue M TF55035A-1) with a custom-built quartz tube at increasing temperatures 200, 500, and 800 °C.[11] The ARGO was added to the quartz tube and heated at a rate of 5 °C min^{-1} to the maximum temperature, held for 30 min, and left to cool at room temperature under He flow. These thermally reduced GO samples are referred to as TGO200, TGO500, and TG800, respectively.

3.2.2. Material characterization.

All the GBNMs were characterized using X-ray photoelectron spectroscopy (XPS) and Scanning Electron Microscopy (SEM) to quantify the surface functional groups and size of GO sheets, respectively. For XPS analysis, the sample holder was covered with double-sided copper tape and dusted with enough GO powdered material to cover the surface. The sample was then loaded in a Thermo Scientific ESCALAB 250Xi that uses a monochromatic Al Kα X-ray source with the following parameters: 1486.7 eV and a spot size of 650 µm. Survey spectra were collected using a 1.0 eV step size and 150 eV pass energy while a 0.1 eV step size and 50 eV pass energy were used for the high resolution spectra. Three measurements in different locations were collected per sample. The Thermo Scientific Avantage software was used for peak fitting and to calculate the atomic percentage.[11] The SEM images were taken with an Amray 1910 FE-SEM using 10 eV. For sample preparation, 3 µL of a diluted 50 µg/mL GO stock solution was drop-casted on a 1 cm × 1 cm silicon wafer previously cleaned via UV-ozone treatment for 20 min (UV/Ozone

ProCleaner, BioForce Nanosciences, Ames, IA). The ImageJ software was used to process the SEM images and measure GO dimensions.

3.2.3. Toxicity of GBMNs to *E. coli*.

The antimicrobial suspension assays were done according to Barrios et al.[120] *E. coli* W3110 (American Type Culture Collection ATCC 11303) was grown overnight in Lysogeny Broth (LB) on a shaker plate at 140 rpm in an Isotemp incubator (Fisher Scientific) at 37 °C. Then, the culture was diluted in fresh LB (1:25) and grown until the optical density (OD) reached 1 (~2 h). Cells were washed with sterile 0.9% NaCl solution three times by centrifugation. The bacterial solution was then diluted to 10^7 colony-forming units (CFUs)/mL in sterile saline solution.

For GO exposure to the bacteria, stock suspensions of ARGO and each TGO materials were made in nanopure water (5,000 µg/mL) and bath sonicated for 1 h (M3800 Branson Ultrasonic Corporation, Danbury, CT). The exposure took place in a total volume of 5 mL, where 3.5 mL of sterile 0.9% NaCl, 0.5 mL of clean bacteria solution, and then supplemented with the required volume of each GO suspension to reach concentrations of 1, 10, 50, 150, 250, and 500 µg/mL in 7 mL scintillation vials. A negative control (no GO added) treatment was created by adding 1 mL of sterile DI water. Vials were placed on a horizontal shaker (Branstead Lab-Line) at 80 rpm for 3 h and kept at room temperature. After the 3 h contact time, the bacteria-GO suspensions were diluted (1:10) in Eppendorf tubes and vortexed, and 50 µL of each suspension was spread on a LB agar plate and incubated overnight at 37 °C for CFU enumeration.

3.2.4. Toxicity of GBNMs to aquatic photosynthetic microorganisms.

The freshwater cyanobacteria *M. aeruginosa* (UTEX LB 3037) and green alga *S. obliquus* (UTEX 3031) were both grown and maintained in sterile Bold Basal Medium (BBM) with a pH of 6.8, at a controlled temperature of 28 ± 2 °C, and a constant illumination of 4.85 ± 0.31 mW/cm^2 (Thorlabs, NJ, USA), as previously described.[123] Constant aeration was provided by air bubbling, filtered by a 0.20 µm sterile cellulose filter (VWR, USA), using an aquarium pump (Whisper Air Pump, Tetra, USA). The cultures were diluted once a week with fresh BBM medium to maintain a constant algal growth in the stock solution. To assess the cultures' growth, the relationship between cell density and optical density at 750 nm was measured. Cell density was measured by adding 5 µL of each culture in a hemocytometer and counting the cells with a Leica DM6 epifluorescence microscope (Leica Microsystems, Inc. Buffalo Grove, IL) in bright field mode.

For GO exposure, the algal cultures were diluted to 5×10^5 cells/mL and allowed to grow until mid-exponential phase (~ 2h, monitored by optical density at 750 nm). Stock suspensions of ARGO and each TGO materials were made in nanopure water (2,000 µg/mL) and bath sonicated for 72 h (M3800 Branson Ultrasonic Corporation, Danbury, CT). In 50 mL Erlenmeyer flasks, 18 mL dilution of 2×10^6 cells/mL is made from the stock solution of *M. aeruginosa* and BBM medium. Then, a volume of the stock GO suspension was added to reach concentrations from 1, 5, 10, 25, 50, and 100 µg/mL in a total volume of 20 mL, supplementing with sterile BBM to 20 mL, as needed. A control (no GO added) treatment was made by adding 2 mL of sterile BBM into the 18 mL algal dilution. Flasks were kept at a constant temperature (28 ± 2 °C) on a shaker at a speed of

60 rpm for 96 h. After the 96-h contact time, 1.5 mL of the algae-GO aliquots were collected in 2 mL Eppendorf tubes, centrifuged for 10 min, and the supernatant was removed, keeping the algal cells and the GO in the pellet. Then, 0.5 mL of methanol were added to the Eppendorf tubes, vortexed, placed on a digital dry bath (Fisher Scientific Waltham, MA) set at 70°C for 10 min, and centrifuged again for 10 min to pellet the cell debris. A 0.2 mL volume of the pigment extract (supernatant) was placed in a transparent microplate to measure chlorophyll *a*, chlorophyll *b*, and total chlorophyll concentrations on a microplate reader (Synergy H4, BioTek) according to Lichtenthaler.[124]

3.2.5. Toxicity of GBNMs to *D. magna*.

The freshwater microcrustacean *D. magna* was maintained according to ISO 6341[125] and NBR 12.713.[126] The organisms were kept in M4 medium at controlled temperature (20 ± 2 °C) and diffuse luminosity with a photoperiod of 16h of light and 8h of darkness. The *D. magna* was fed three times a week with approximately 10^6 cells/mL per organism using *Scenedesmus subspicatus* algal culture.

Prior to the acute toxicity tests with *D. magna*, ARGO and each TGO samples were diluted in ISO medium, according to NBR 12.713.[126] The stock suspensions (500 mg/L) were bath sonicated (Ultrasound bath, model Q3360, QUIMIS, São Paulo, Brazil) at 70 W for 4h. In the assays, offspring of *D. magna* (2-26h old) were exposed to concentrations of 12.5, 25, 50, 100, 200, and 400 mg/L. The negative control was conducted with ISO medium only (no GO added). For each dilution, 20 *D. magna* offspring were exposed (duplicates of ten organisms) for a period of 48 h. The toxicological endpoint was the immobilization of the organisms. The data were statistically analyzed using the Trimmed Spearman-Karber method and the results were expressed as $EC_{50,48h}$.

3.2.6. Aggregation experiments.

Aggregation experiments were performed with ARGO in the respective media used for toxicity assays: 0.9% NaCl (bacteria), BBM (algae/cyanobacteria), and ISO medium (invertebrate). No organisms were included, and experiments were performed at ambient temperature. ARGO stock solutions (2000 µg/mL in DI water) were bath sonicated for 1 h (150HT Ultrasonic Cleaner, Aquasonic, USA). An experimental concentration of 100 µg/mL was used in all media. Additional concentrations of 200 µg/mL for 0.9% NaCl, 10 and 40 µg/mL for BBM (for *M. aeruginosa* and *S. obliquus* respectively), and 400 µg/mL for ISO medium were studied, representing the respective EC_{50} values. Hydrodynamic diameter (D_h) was analyzed 5 min after the addition of ARGO stock and at the end of the respective toxicity assay duration: 3 h for bacteria, 96 h for algae, and 48 h for daphnia. All experimental samples were agitated according to details specified in toxicity assays. Experiments were performed in triplicates with 5 mL solution in 7 mL scintillation vials for ISO medium and 0.9% NaCl, and 20 mL solution in 50 mL Erlenmeyer flasks for BBM. The respective volumes were selected based upon the experimental setups of the toxicity assays. In the interest of conserving materials, the volume of ISO medium differed based on the lack of motion limiting the potential for variability. The ARGO aggregate size was measured using dynamic light scattering (DLS, Litesizer 500, Anton-Paar, Austria) to obtain D_h. All measurements were determined at a 90° detection angle. Spectra were averaged over 12 scans. UV-vis analysis of sample solutions was performed, showing negligible absorption at the LiteSizer 500 light wavelength (658 nm).

3.2.7. Effective concentration calculation.

The software OriginPro 8.5.1 was used to calculate the EC_{50} in bacteria and alga/cyanobacteria experiments. Data fitting was done using a sigmoidal fit using the dose-response function with the following equation:[72]

$$y = A1 + \frac{A2 - A1}{1 + 10^{(log_x0 - x)p}} \quad (1)$$

Where A1 = bottom asymptote, A2 = top asymptote, $\log_x 0$ = center, p = hill slope, and EC_{50} is given by:

$$EC_{50} = 10^{log_x 0} \quad (2)$$

For invertebrates, the EC_{50} values were calculated through the Trimmed Spearman-Karber method, after Hamilton et al.[127]

3.2.8. Fluorescent dye assays after GBNMs exposure.

To further investigate biochemical responses of bacteria and cyanobacteria to GO, a set of fluorescent dyes were used at the EC_{50} concentrations of either *E. coli* or *M. aeruginosa* after exposure to ARGO and TGO800 (bacteria) or TGO500 (cyanobacteria). Changes in esterase activity and membrane damage and oxidative stress were evaluated using the FDA and H_2DCFDA fluorescent dyes, respectively.[73] Stocks solutions for each dye were prepared according to the manufacturer specifications (Molecular Probes^{TM}, Thermo Fisher, Waltham, MA): 10 mM for FDA and H_2DCFDA and kept at -20^{o}C in the dark. After the exposure time (3h for bacteria, 96h for cyanobacteria), 1 mL of the cells were stained with a final concentration 5 mM of FDA or 0.2 mM H_2DCFDA. The samples were incubated for 30 min in the dark before pipetting 200 µL of each sample in a 96 well plate. The fluorescence was measured using excitation/emission wavelengths of 490/526 nm for FDA and 495/527 for H_2DCFDA on a multi-mode microplate reader (Synergy H1, BioTek). Data was expressed as the mean fluorescence intensity and the results as a percentage with respect to the control.

3.2.9. Catalase activity after GBNMs exposure.

CAT activities were measured for *E. coli* and *M. aeruginosa* after exposure to ARGO and TGO800 (bacteria) or TGO500 (cyanobacteria) at their EC_{50} concentrations. For the antioxidant enzyme measurements, 2 mL of either bacterial or cyanobacterial cell suspensions were collected in Eppendorf tubes after the allocated contact time (3h or 96h). Samples were centrifuged (5,000×g, 1 min) to form a pellet and then washed three times with 1 mL of 50 mM phosphate buffer (pH = 7.4). Cells were homogenized using bath sonication (M3800 Branson Ultrasonic Corporation, Danbury, CT) for 30 min kept at 4 °C using ice and then centrifuged at 5,000×g at 4 °C for 1 min. The supernatant was used for biochemical analysis. CAT activity was evaluated spectrophotometrically by the decomposition rate of hydrogen peroxide (H_2O_2) at 240 nm at 25 °C according to Aebi.[128] Total soluble protein was measured using the Pierce^{TM} BCA Protein Assay Kit (Thermo Scientific No. 23225).

3.2.10. Electron microscopy of cells after GBNMs exposure.

The effect of GO exposure on cell morphology was evaluated for *E. coli* and *M. aeruginosa* after contact to ARGO and TGO800 (bacteria) or TGO500 (cyanobacteria) using SEM and TEM imaging. Cultures were prepared depending on the parameters used for the toxicity assays using the 3h and 96h EC_{50} concentrations. At the end of the contact time, cells were collected by centrifugation (5,000×g, 1 min) and the pellet fixed in Karnovsky's fixative (2% paraformaldehyde, 2.5% glutaraldehyde in 0.2 M Sorenson's buffer, pH= 7.2) overnight at 4°C.

For SEM imaging, the fixed cells were washed once with Dulbecco's Phosphate Buffered Saline (DPBS), adhered to poly-L-lysine coated coverslips, and then washed two additional times with DPBS. Secondary fixation was done with 1% OsO_4 in DPBS for 1h at room temperature, followed by three washes with DI water. Cells were dehydrated with an ascending series of ethanol solutions followed by critical-point drying using a CPD-020 unit (Balzers-Union, Principality of Liechtenstein) with liquid CO_2 as the transition fluid. The dried samples were mounted on aluminum stubs and coated with 10-12 nm of gold-palladium using a Hummer II sputter coater (Technics, San Jose, CA). Imaging was done on a JSM 6300 SEM (JEOL USA, Peabody, MA) operated at 15 kV and images were captured with an IXRF Systems model 500 digital processer (IXRF System Inc., Austin, TX).

For TEM imaging, the fixed cells were pelleted and entrapped in 0.8% agarose before washing three times with DPBS. Cell pellets were then fixed with 1% OsO_4 in DPBS for 2h at room temperature and rinsed four times with deionized water. The cells were stained overnight at 4°C using 1% aqueous uranyl acetate and washed the following morning with 4 changes of DI water. Cells were dehydrated with an ascending series of ethanol concentrations (20, 40, 60, 80, 100% ethanol), rinsing three times with 100% ethanol. Then, the 100% ethanol was replaced twice with propylene oxide before infiltrating the samples in increasing concentrations of Spurr’s standard mixture epoxy resin[129] using 25% increments. Embedded samples were polymerized at 60°C for 24 hrs. Resin blocks with microtomed to 70 nm sections with a Leica Ultracut-R microtome (Leica Microsystems, Buffalo Grove, IL) and collected on formvar-coated copper slot grids. Microtomed sections were stained with 2% uranyl acetate in 50% ethanol for 6 min followed by Sato's lead citrate[130] for 3-4 min. Images were obtained using a Philips CM12 TEM (Philips, Eindhoven, Netherlands) operated at 80kV. Micrographs were acquired with a Gatan model 791 CCD camera.

3.2.11. Data analysis and statistics.

All experiments were done using triplicate samples and in three independent experiments at a minimum. Data is shown as means and standard deviation, calculated for each treatment. A one-way analysis of variance (ANOVA) followed by a Tukey post-hoc test with $p<0.05$ was done to determine significant differences between control samples and GO treated samples. These differences were indicated using different letters in the figures. Statistical analysis was done using the Statistical Package for Social Sciences (SPSS) software version 26.

3.3. Results and discussion

3.3.1. Experimental conditions.

A literature review was performed to compile the different experimental conditions commonly used for studying the toxicity of GO and its material derivatives (i.e., reduced GO, graphene) for each organism (*E. coli*, *M. aeruginosa*, *S. obliquus*, or *D. magna*), including parameters and endpoints employed (Table B.1.). Three main observations emerged: 1) Experimental conditions (time and manner of exposure, and materials' concentrations) vary across organisms; 2) The extent of material characterization is not uniform; and 3) There are many toxicity endpoints used to measure the response of an organism towards a material. This data collection informed our selection of conditions for this study facilitating comparison to the existing literature (Table 3.1). The four organisms were selected to represent their respective taxa. Bacteria, algae, and aquatic invertebrates are attractive for toxicity characterization because their generation spans are shorter than those of higher organisms like fish.[122] Additionally, toxicity tests using these organisms usually require smaller volumes and thus, require smaller quantities of NMs. The range of GBNMs' concentrations we investigated showcase the different sensitivities of each organism towards GO.

The literature survey also highlighted the gaps in materials characterization reporting in GBNMs' toxicity studies. While it is common practice to report characterization parameters like GBNMs' thickness, lateral size, and defect density (i.e., D/G ratio), the focus on surface chemistry is less frequently found. The carbon-to-oxygen ratio or C/O ratio has been identified as a key parameter to better understand the relationship between surface chemistry and toxicity for GBNMs[120] but it is not comprehensively studied. Moreover, the type of oxygen functional groups (i.e., epoxides, hydroxides) in GBNMs play a role in the materials' interactions as the surface chemistry changes.[120,131] Wang et al. for example, found a direct correlation between the epoxide groups of GBNMs with different surface chemistries and glutathione.[132] Thus, suggesting that thorough material characterization is necessary to identify further indicators that will help in safer material design. This study utilizes the same material set, ARGO and thermally annealed ARGOs, which are compared across all the chosen organisms that represent different taxa. The systematic reduction of ARGO produces GBNMs of different surface chemistries. To the authors' knowledge, this is the first study to date, that focuses on surface chemistry impacts across multiple species.

Table 3.1. Experimental conditions for each organism tested.

Organism	Taxon	Medium	Contact time (h)	Concentrations (μg/mL)	Parameter used for EC_{50}
E. coli	Bacteria	0.9 % NaCl	3	0-500	CFU enumeration
M. aeruginosa	Cyanobacteria	BBM	96	0-100	Chlorophyll
S. obliquus	Algae	BBM	96	0-100	Chlorophyll
D. magna	Invertebrate	ISO	48	0-400	Immobilization

3.3.2. Surface chemistry characterization of GBNMs.

The different GBNMs were characterized by XPS to identify how the surface chemistry of ARGO and TGOs influence their interaction with different organisms. XPS offers a quantitative approach to evaluate the reduction degree of ARGO as a function of thermal annealing. Further, multiple batches of each material were prepared for carrying out the toxicity assays, making sure to use the same batch for each taxon studied. Surface characterization is important to ensure that the desired trend in O% is attained (Table 3.2 for C/O ratio and Table B.2. for full chemical composition). The C% in all annealed materials increased significantly as the annealing temperatures increased. The C% were in the ranges of 66-71% for ARGO, 80-82% for TGO200, 85-88% for TGO500, and 83-92%

for TGO800. These results were accompanied by a decrease in O% with ranges of 28-33% for ARGO, 17-18% for TGO200, 12-13% for TGO500, and 7.5-12% for TGO800.

The C/O ratio (Table 3.2) serves as an indicator of the degree of surface reduction. The increase in C/O ratio from ARGO<TGO200<TGO500<TGO800 confirms successful deoxygenation of the ARGO surface and indicates restoration of the conjugated carbon structure.[77] These results are in accordance with previous studies, where thermal annealing systematically reduces the O% of ARGO as the temperature increases.[11,120] Furthermore, peak deconvolution of the C1s spectra determined the relative presence of different carbon-oxygen bonds for all GBNMs (Table B.2.). The deconvolution of C1s resulted in four peaks located approximately at binding energies of 284.8, 286.3, 287.5, and 288.8 eV which are commonly assigned to single and double carbon bonds (C-C/C-H), epoxide and hydroxyl (C-O), carbonyl (C=O), and carboxylate (COOH) functional groups, respectively.[11,120] The content of C-O groups, including epoxide and hydroxyl groups on the GO basal plane, decreases consistently across batches from 41.89% for ARGO to 8.18% for TGO800 upon thermal annealing. This decrease can be attributed to the reduction of epoxide groups, which are the most abundant on GO surfaces[11,77] and are not chemically or thermally stable.[11] At the highest temperature used (800°C), C-O bonding contributes the highest fraction (in a range from 8.18 to 9.75%) compared to C=O (from 3.53 to 4.58%) and COOH (from 1.49 to 1.62%) across batches. This has been observed in previous studies and is attributed to the higher thermal stability of hydroxyl groups intercalated into graphene interlayers.[11,77] The carbonyl and carboxylate groups, mostly found in the edges of the GO structure, exhibit a steady decrease upon thermal reduction.

Elemental survey by XPS also revealed the presence of other residual elements on the materials' surface: sulfur (S%), nitrogen (N%), and sodium (Na%) (Table B.3.). These impurities are most likely from the precursors used during the synthesis of the GO. A commercial GO material synthesized by a modified Hummers method was used, and typical reagents used for the modified Hummers reaction include H_2SO_4, $NaNO_3$, and $KMnO_4$.[13] All ARGO materials were of 98.5% purity or higher before thermal annealing. Thermal annealing of ARGO at any of the temperatures used (200, 500, or 800 ºC) had no significant effect on the materials' sheet size and the average lateral sheet was of 1.2 ± 0.7 µm for the most oxidized material (ARGO) and 1.1 ± 0.7 µm for the most reduced material (TGO800).[120]

Table 3.2. Compiled XPS data representing the C/O atomic ratio for ARGO and TGO samples. Data is shown as means ± standard deviations of triplicate measurements.

	Bacteria	Algae/Cyanobacteria	Invertebrates
ARGO	2.02 ± 0.06	2.01 ± 0.07	2.54 ± 0.47
TGO200	4.41 ± 0.03	4.64 ± 0.09	4.70 ± 0.13
TGO500	6.48 ± 0.62	7.61 ± 7.48	7.48 ± 0.59
TGO800	7.19± 0.11	11.7 ± 1.68	12.0 ± 1.00

3.3.3. Toxicity of GBNMs differs across species.

The toxicity of the GBNMs to *E. coli*, *M. aeruginosa*, *S. obliquus*, or *D. magna* was characterized according to the parameters shown in Table 3.1. For all species, the EC_{50} was selected as the biological endpoint to compare toxicity. For bacteria, the antimicrobial properties of ARGO and TGOs were assessed by mixing *E. coli* with GBNMs suspensions of concentrations ranging from 0 to 500 µg/mL for 3h to generate a dose-response curve. A sigmoidal fit was used to calculate the EC_{50} value per material. The EC_{50} was characterized by a reduction of bacterial cell viability determined by a decrease in colony forming units (CFU). Figure 3.1 shows that each material reduced bacterial viability by 50% at different concentrations (red squares). According to the dose-response curves, the calculated EC_{50} values were 183 ± 33.9 for ARGO, 143 ± 24.8 for TGO200, 127 ± 11.0 for TGO500, and 86.3 ± 28.9 µg/mL for TGO800.

D. magna, a model organism for aquatic invertebrates, was exposed for 48h to GBNMs suspensions with concentrations from 0 to 400 µg/mL. The calculated EC_{50} values were 383 ± 29.9 for ARGO, 187 ± 18.3 for TGO200, 319.8 ± 14.4 for TGO500, and 263.2 17.0 µg/mL for TGO800 (blue triangles). It is worth noting that the TGO200 value for *D. magna* was found to be an experimental artifact due to the high variability in the results for this test condition and thus, the TGO200 data point is not shown in Figure 3.1 (see Table B.4. for all data). For both green algae and cyanobacteria, the toxicity of GBNMs was determined by changes in chlorophyll *a* (Chl *a*) concentration, as an indicator of biomass, after a 96h exposure with the GBNMs at concentrations from 0 to 100 µg/mL. The Chl *a* extraction method used to assess algal toxicity was chosen to avoid artefacts that could arise if using optical based methods such as optical density measurements.[133] Based on the dose-response curves, the EC_{50} values for *M. aeruginosa* were 11.1 ± 2.36 for ARGO, 76.3 ± 12.6 for TGO200, and 126 ± 78.2 µg/mL for TGO500 (green circles). The EC_{50} value for TGO800 was not included in Figure 3.1 because the calculated value (45.5×10^3 µg/mL) was higher than any of the concentrations tested and therefore cannot be considered reliable. Similarly, for *S. obliquus*, only the EC_{50} value of ARGO could be calculated since, for all the TGO materials, there was no change in biomass at any of the tested concentrations (see Figure B.1.). The EC_{50} of ARGO for this specie was calculated as 42.4

± 15.1 µg/mL (Figure 3.1, purple dot). The absence of toxicity for the more reduced TGOs, compared to ARGO, do suggest a similar trend in *S. obliquus* as in *M. aeruginosa*: the reduction of ARGO to TGO reduces the toxicity of the material for both organisms.

The relationship between the C/O ratio of the different GBNMs and their toxicity to the different organisms is illustrated in Figure 3.1. For bacteria and invertebrates, the trend is similar, where the highest toxicity comes from the reduced materials and the lowest toxicity from ARGO. For both *E. coli* and *D. magna*, there is a strong linear relationship between reduction degree and toxicity with an $R^2 = 0.91$ for bacteria and an $R^2 = 0.99$ for invertebrates. Interestingly, for algae, the results show the opposite trend from those of *E. coli* and *D. magna*. Particularly, for *M. aeruginosa*, the strong ($R^2 = 0.97$) EC_{50}-C/O relationship shows that TGO500 (C/O = 7.61) is less toxic than ARGO (C/O = 2.01).

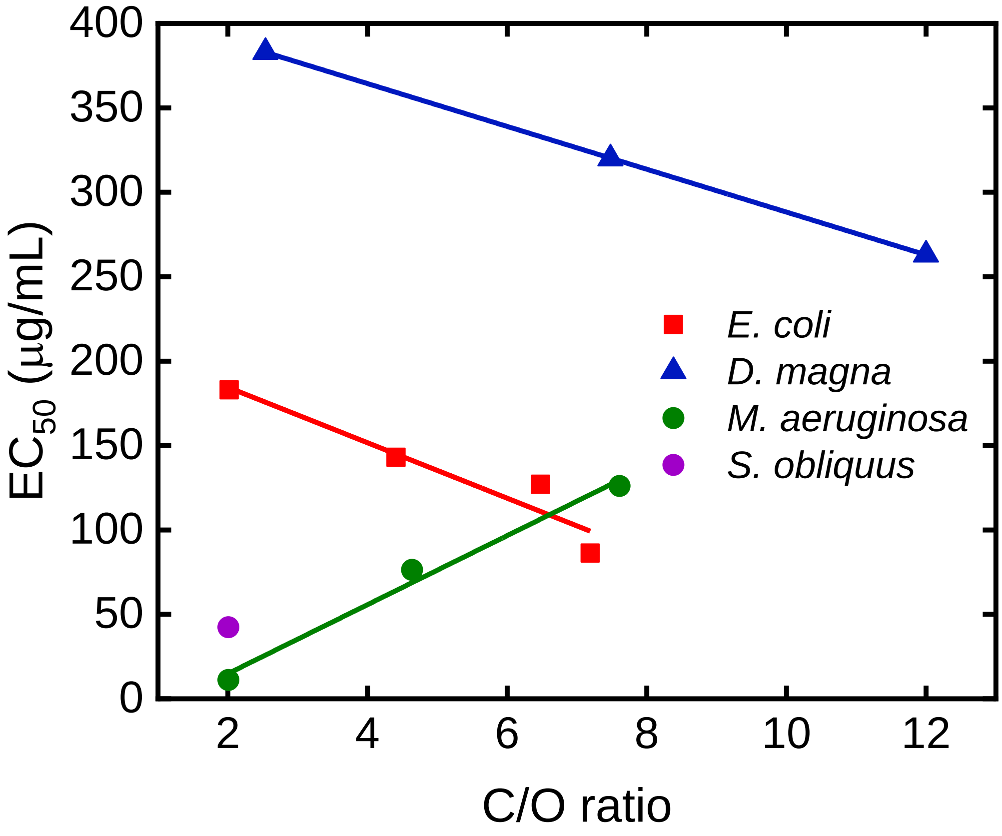

Figure 3.1. EC_{50} values of GBNMs of different C/O ratios for cyanobacteria (M. aeruginosa, 96h assay); green algae (S. obliquus, 96h assay); bacteria (E. coli, 3h assay), and invertebrates (D. magna, 48h assay). The exposure time is based on standard protocols for each model. The EC_{50} values of S. obliquus after a 96h contact time with the TGO materials could not be calculated as there was no response (Figure S1). Each point represents the average of three individual experiments with triplicate samples (n=9).

3.3.4. ARGO aggregation changes in different media.

The influence of ionic strength and media components on nanomaterial aggregation is well documented and has been proposed as influencing NMs' toxicity.[134] To determine whether the observed EC_{50} trends are governed by aggregation, we monitored aggregation of ARGO in the different test media. Each biological media has a different ionic strength and composition (Table B.4.) [135], which can influence the GBNMs aggregation.[135–138] Since the EC_{50} is significantly different for the different organisms (11.1 µg/mL for *M. aeruginosa* vs 383 µg/mL for *D. magna*), observing aggregation of ARGO in the different media will provide insight into its contribution to our observed trends. ARGO aggregation was analyzed at the beginning (5 min) and end of the toxicity assay durations (3h for bacteria, 48h for invertebrates, and 96h for algae) without organisms present. In addition to the EC_{50} concentration, changes in D_h were assessed at a constant ARGO concentration (100 µg/mL) to account for any concentration effects (Figure 3.2). Since determining D_h values by DLS and Stokes-Einstein equation assumes spherical particles, the values reported here are not representative of the real particle size since GO is not spherical. However, the change in D_h is an indicator of the relative GO aggregate size in the different media.[139]

When the ARGO concentration remained constant at 100 ug/mL, the initial D_h for BBM, 0.9% NaCl, and ISO were 0.13 ± 0.00, 0.58 ± 0.15, and 0.30 ± 0.04 µm respectively (solid bars) whereas the final were 0.26 ± 0.08, 0.80 ± 0.17, and 0.64 ± 0.18 µm (dashed bars) (Fig 3.2A). The 0.9% NaCl media used in the bacteria studies showed statistically significant differences in ARGO aggregate size compared to BBM and ISO ARGO aggregates (as D_h) in both initial and final measurements. The difference in aggregate size is attributable to the different ionic strengths and polyvalent cation composition and concentrations in the different media (Tables B.5. and B.6.). ARGO has the largest aggregate size in 0.9% NaCl media, with the highest ionic strength (147.9 mM) compared to BBM or ISO media (7.10 and 6.74 mM, respectively). Moreover, the initial and final D_h

values are statistically different for the BBM and ISO media. The change in aggregate size indicates that over time, the interaction between the aggregates and the organisms could change. These results suggest that the media composition differentially influences ARGO aggregation. Yet, 100 ug/mL is not representative of the ARGO concentration used in the respective toxicity assays and thus, does not capture the aggregation behavior of ARGO when in contact with the different organisms. We, therefore, also investigate the change in D_h at the respective EC_{50}.

When aggregation is considered at the same biologically relevant concentration, the EC_{50}, results show no statistical difference in ARGO D_h across media at the initial measurements, which range from 0.12 ± 0.04 µm to 0.23 ± 0.10 µm. However, when measured at the end of the exposure period for each organism, the D_h values increased to 0.21 ± 0.11, 0.42 ± 0.29, 0.66 ± 0.31, and 1.02 ± 0.61 µm for BBM (*M. aeruginosa, S. obliquus*), 0.9% NaCl (*E. Coli*), and ISO (*D. Magna*), respectively (Figure 3.2B). Only the D_h value at 96h in ISO medium is statistically different from the others and is explained by the higher concentration of polyvalent cations (Table B.6.), which are known to have a greater influence on the aggregation of GO.[135,140] The different media also had a slight difference in pH, ranging from 6.8 to 7.8 (Table B.6.). However, this range remains biologically relevant and the difference in pH is not expected to play a major role in the difference in D_h between the media.[136]

Aggregation can alter the way GBNMs interact with the different organisms. For example, cell wrapping, which is a common mechanism observed in *E. coli*,[67,120,141], *S. obliquus*[105,142] and *M. aeruginosa,*[142,143] would be affected by the decrease in available surface area caused by GO aggregation. Membrane damage and wall permeation is another commonly proposed mechanism that can be affected by aggregation, as the increased thickness of re-stacked GO can induce the nano-knife effect.[144] Internalization of the material via active uptake mechanisms will also be affected by the aggregate size, particularly in the invertebrate *Daphnia* model. Although *Daphnia* can take in materials from 0.4-40 µm,[105,145] the rate of uptake is significantly reduced outside of 0.24-0.64 µm.[146–148]

Since all the different organisms considered had different physiology, growth cycle, and media requirements, it was impossible to use homogeneous testing conditions. As a result, the ARGO aggregation behavior is expected to be different in the different assay conditions. However, characterizing the aggregation behavior in each media is important to understand the potential importance of aggregation in toxicity under the assay conditions. Based on the results (Figure 3.2A), there is no clear relationship between D_h and EC_{50} when the same ARGO concentration is used. The medium that induced the highest aggregation, the 0.9% NaCl medium, did not have the highest EC_{50} value (Figure 3.2A). At the ARGO EC_{50}, the D_h increases as the EC_{50} increases; however, this may be also related to the higher GO concentrations in the test medium, which lead to larger aggregate size (Figures 3.2B and B.2.). Therefore, while aggregation may influence the toxicity of GBNMs, species-specific factors are likely to have a more important impact on the measured EC_{50}.

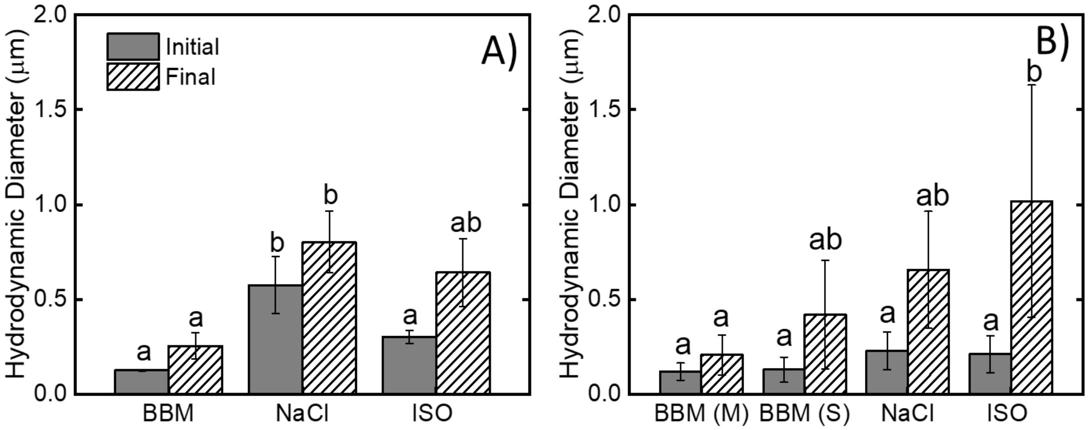

Figure 3.2. Hydrodynamic diameter (D_h) measurements for the initial (5 min) and final ARGO DLS measurements in 0.9% NaCl (3h), BBM (96h), and ISO (48h) for A) constant ARGO concentration of 100 ug/mL and B) EC_{50} ARGO concentration for M. aeruginosa (purple), *S. obliquus* (green), *E. coli* (red), and *D. magna* (blue). Solid and dashed bars represent initial and final DLS measurements, respectively. The letters in parenthesis in Fig 2B represent *M. aeruginosa* and *S. obliquus*, respectively since both algae used BBM media. Results are shown as average ± standard deviation (n=3). Different letters represent significant statistical differences ($p \leq 0.05$) across the different media.

3.3.5. Cellular response of bacteria and cyanobacteria to GBNMs.

The relationship between C/O ratio and EC_{50} in GBNMs was found to differ between organisms. Among the four organisms tested in this study, *E. coli* and *M. aeruginosa* have the most contrasting results and display opposite trends in toxicity (see Fig. 3.1) despite being the most closely related organisms (both gram negative prokaryotic organisms). To determine if these opposite trends are associated with a difference in how the materials interact with the cells, the response of each organism to oxidized (ARGO) and reduced ARGO (TGO500 or TGO800) was evaluated using fluorescent dye-based assays that probe different cellular responses characteristic of NMs exposure. The dyes used are fluorescein diacetate (FDA), and H_2DCFDA, which evaluate esterase activity or reactive oxygen species (ROS) levels, respectively (Fig. 3.3A-B). The materials were compared at their EC_{50} concentrations: 180 µg/mL for ARGO and 90 µg/mL TGO800 for *E. coli*; 11 µg/mL ARGO and 130 µg/mL TGO500 for *M. aeruginosa*. By comparing materials at their EC_{50} and not on a fixed nominal concentration, we integrate any effect of reduced bioavailability due to the differences in colloidal stability of the different materials in the different media to put the focus only on whether or not the same level of toxicity was induced by the same mechanisms in *E. coli* compared to *M. aeruginosa*.

In bacteria, the toxicity of ARGO was characterized by a 55% increase in intracellular ROS while, for TGO800, no significant ROS production was observed. However, FDA fluorescence, which is associated with metabolic activity and membrane integrity, increased by 74% (Figure 3.3A). These results are in agreement with the higher biological reactivity typically observed in more oxidized GBNMs[92,93,120]. Conversely, for *M. aeruginosa*, ARGO decreased intracellular ROS and FDA fluorescence levels by 31% and 69%, respectively, when compared to control, while TGO500 only had a significant effect on FDA fluorescence, reducing it by 28% with respect to the control (Figure 3.3B). These results show a contrasting response of the two models to the different materials, where ARGO increases oxidative stress in bacteria but reduces it in cyanobacteria while TGOs increase metabolic activity in bacteria but reduces it in cyanobacteria. These results agree with the results obtained by the dose-response curves and the opposite trends observed in Figure 1, supporting the hypothesis that the interaction mechanisms between ARGO and bacteria are different from those observed with cyanobacteria.

Previous studies have indicated that oxidative stress is an important mechanism of toxicity for GO in bacteria[67,92,120,149] and algae.[116,142,143,150,151] A rise of ROS production can cause damage to cellular components like proteins, lipids, and DNA [86]. Results show that ARGO, the most oxidized material in this study, has the highest potential of generating oxidative stress in bacteria compared to the thermally annealed TGOs. While CNMs have the capacity to directly generate ROS in a cellular environment or in the presence of light,[93,152] the increase in H_2DCFDA fluorescence may also be the result of an impact of ARGO exposure on the cell functions. In the cells, ROS are generated intracellularly during aerobiosis-fueled oxygen metabolism which generates superoxide ($O_2^{\bullet-}$), hydrogen peroxide (H_2O_2), and highly destructive hydroxyl radicals ($OH^{\bullet}$) [153]. The fluorescent dye H_2DCFDA however, is a general stress indicator and is sensitive to a wide range of ROS and as such, this method only provides information regarding a generalized quantification of ROS.

Even though cyanobacteria do not show an increase in H_2DCFDA fluorescence, it is worth mentioning that the dye's fluorescent response is dependent on the esterase enzymes, which hydrolyze H_2DCFDA. Thus, since there is a decrease in FDA fluorescence, which is related to esterase enzymes activity, the H_2DCFDA response may be affected.[154] FDA is a nonfluorescent molecule that is taken up by cells by passive diffusion to be hydrolyzed by the esterase enzymes into the fluorescent fluorescein molecule. As such, FDA fluorescence is dependent on both the esterase enzyme activity and the integrity of the cell membrane.[155] The increase in FDA fluorescence in bacterial cells is attributed to an increase in the interactions between GO and the cells' surface [90,120] leading to a decrease in cell permeability causing dye retention. In the case of a decrease in FDA, as is observed with *M. aeruginosa*, the response suggests a decrease in metabolic activity associated with reduced photosynthesis or a disruption of the membrane integrity.[122] Given this potential influence of esterase activity on the measured ROS level, the H_2DCFDA results were corroborated with a second assay, the measure of the intracellular catalase (CAT) activity (Fig. 3.3C-D). The CAT enzyme, along with superoxide dismutase (SOD), ascorbate peroxidase (APOX), and low molecular weight antioxidants (i.e., glutathione), constitute the antioxidant defense system developed by all organisms to protect themselves against ROS damage.[156,157] The CAT enzyme activity was chosen here as an indicator of oxidative stress because previous studies have shown that CAT is a more sensitive indicator of oxidative stress induced by NMs compared to the other enzymes.[73,158] The CAT enzyme dismutates H_2O_2 as given by the reaction below, where H_2O_2 is converted to water and oxygen:[157]

$$2H_2O_2 \rightarrow 2H_2O + O_2$$

Results show that in bacteria exposed to ARGO, there is a significant increase in CAT activity from 15.3 ± 4.13 mmol/min^{-1}•µg^{-1} in the control treatment to 52.4 ± 7.36 mmol/min^{-1}•µg^{-1} in ARGO treated bacterial cells (Fig. 3.3C). Additionally, there was no statistical difference between control and TGO800 treated cells. For cyanobacteria, cells treated with ARGO or TGO500 showed no difference in CAT activity when compared to controls (Fig. 3.3D). These results agree with the observations made with the fluorescent dyes and confirm that ARGO, the most oxidized material, induces the highest oxidative stress level in bacterial cells. Likewise, the catalase results in cyanobacteria confirm that oxidative stress is not a primary mechanism taking place between the GBNMs and the cells. Therefore, the two organisms show a clear difference in how they respond to change in oxygen content when exposed to GBNMs.

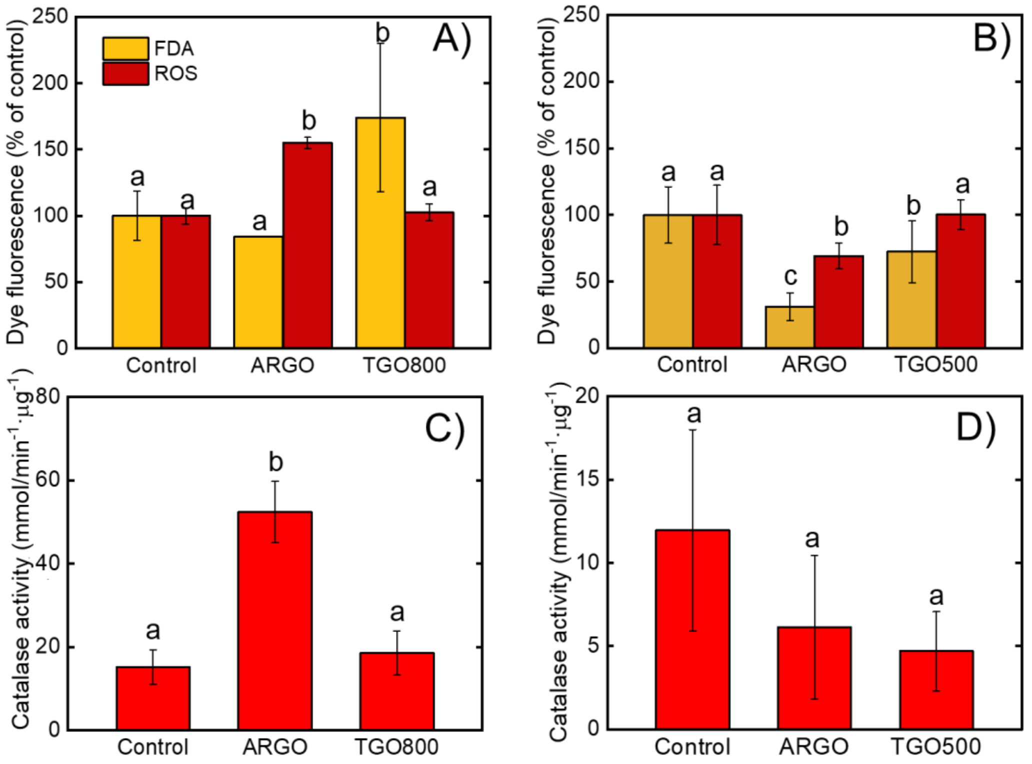

Figure 3.3. Biochemical responses of ARGO and TGOs in *E. coli* and *M. aeruginosa* after 3h and 96h of exposure at their EC$_{50}$ concentrations, respectively. Top panels are fluorescent dye assays showing esterase activity and reactive oxygen species generation for A) *E. coli* and B) *M. aeruginosa*. Data was normalized to the fluorescence response of the control. Bottom panels show catalase activity for C) *E. coli* and D) *M. aeruginosa*. Negative controls using only media (0.9% NaCl or BBM) and bacteria or alga were used throughout (no GO). Different letters represent significant statistical differences ($p \leq 0.05$) compared to the control (n=9).

3.3.7. Effect of GBNMs on cellular integrity.

Since membrane damage is often associated with the toxicity of GBNMs in microorganisms, changes induced by GBNMs exposure to the cellular structure or morphology were evaluated using electron microscopy (Figure 3.4). Cell morphology was evaluated by SEM (Fig. 3.4A-F) and TEM (Fig. 3.4G-I) for *E. coli* and *M. aeruginosa* after exposure to the EC_{50} concentrations of ARGO and TGOs for 3h and 96h, respectively. Figure 4A shows an SEM micrograph of *E. coli* cells not treated with NMs. They appear healthy and with their characteristic rod shape. After exposure to ARGO, however, cells are covered by the material. ARGO appears quite “fibrous” and seem to wrap around the bacterial cells (Fig. 3.4B). TGO800 sheets encounter aggregates of bacterial cells with no evidence of damage as observed in Fig. 3.4C.

The SEM micrograph in Fig. 4D shows control cyanobacterial cells as round and plump. Upon exposure to ARGO, *M. aeruginosa* cells appear to have a “velvet” or wrinkled texture due to a layer of ARGO deposited on the cells’ surface (Fig. 3.4E). All the cells have a similar wrinkled surface which indicates that ARGO interacts with cyanobacteria in a uniform manner. Conversely, cyanobacterial cells exposed to TGO500 show that the cells appear to be in contact with large TGO500 aggregates, and not covered by the material (Fig. 3.4F). For both materials, however, the cells-material interactions do not seem to alter the cells overall structure; they retain their shape, and no indications of membrane damage is evidenced. Similar results were observed in a study by Tang et al. where *M. aeruginosa* was exposed to GO and SEM imaging showed GO adhesion onto the cells’ surface and no morphological changes.[143] Other studies show internalization of GO in algal cells,[143,159] however, that is not the case in our conditions.

The effect of GBNMs to bacteria and cyanobacteria were further investigated by TEM imaging. The ultrastructure of *E. coli* cells after exposure to no NMs, ARGO, or

TGO800 are shown in Fig. 3.4G-I. Untreated cells (Fig. 3.4G and insert) have smooth and regular cell walls, with homogeneous cytoplasmic contents. However, treated cells with ARGO are evidently surrounded by the material (Fig. 3.4H), unlike TGO800, where cells come in contact with aggregates of the material (Fig. 3.4I). Even though no evident physical disruption is observed, some cells look elongated compared to the control, especially after ARGO exposure. These results indicate that GO sheets could wrap around the bacteria cells, which has been observed in previous studies.[57,120] The wrapping mechanism occurring between ARGO and *E. coli* cells may help explain the oxidative stress response observed. Although there is a significant increase in ROS and catalase activity, electron microscopy images show no major damage in cell morphology or cellular components. To this point, previous reports have shown that the wrapping mechanism can isolate bacteria from their environment, thus, limiting access to nutrients and preventing their growth but without immediate cell inactivation.[57] Therefore, an oxidative response may have been triggered without resulting yet to an oxidative damage to the membrane.

As shown in TEM images, most *M. aeruginosa* cells have intact cell membranes after exposure to both materials with a few exceptions (Fig. 3.4J-L, and inserts). Control cells (Fig. 3.4J and insert) have a normal intracellular structure with a three-layer cell wall, dense cytoplasm, and had the typical organelles: cyanophycin granules, lipid droplets, polyphosphate bodies, thylakoid, and ribosome clearly visible.[160] In contrast, cyanobacterial cells exposed to either ARGO or TGO500 show a less defined ultrastructure, with large vacuoles localized in the cell, and an overall smaller cell size (more noticeable with TGO500). For ARGO, cells are surrounded by the material (like in

SEM images and Fig. 3.4K), while for TGO500, the material appears to be concentrated as an aggregate (Fig. 3.4L). These results suggest that the reduction in FDA fluorescence is not due to membrane damage and that a lower metabolic activity may be involved. When exposed to CNMs, photosynthetic organisms were shown to experience lower photosynthetic activity due to a shading effect caused by the dark GBNMs in the medium and around the cells. Photosynthesis being the only source of cellular energy for cell division and growth, the shading effect could lead to a decrease metabolic activity and lower FDA fluorescence.[161] These observations agree with other reports where photosynthetic organisms were exposed to GBNMs.[162]

For both *M. aeruginosa* and *E. coli*, the cells do not appear to have the collapsed structure indicative of membrane disruption and cell damage observed in previous studies involving the interactions of bacteria with GBNMs.[92] This contrast may be attributed to species-specific differences like the different cell wall architecture between bacteria and cyanobacteria, where *M. aeruginosa* cell walls have a thicker peptidoglycan layer that can offer additional protection against membrane damage.[163]

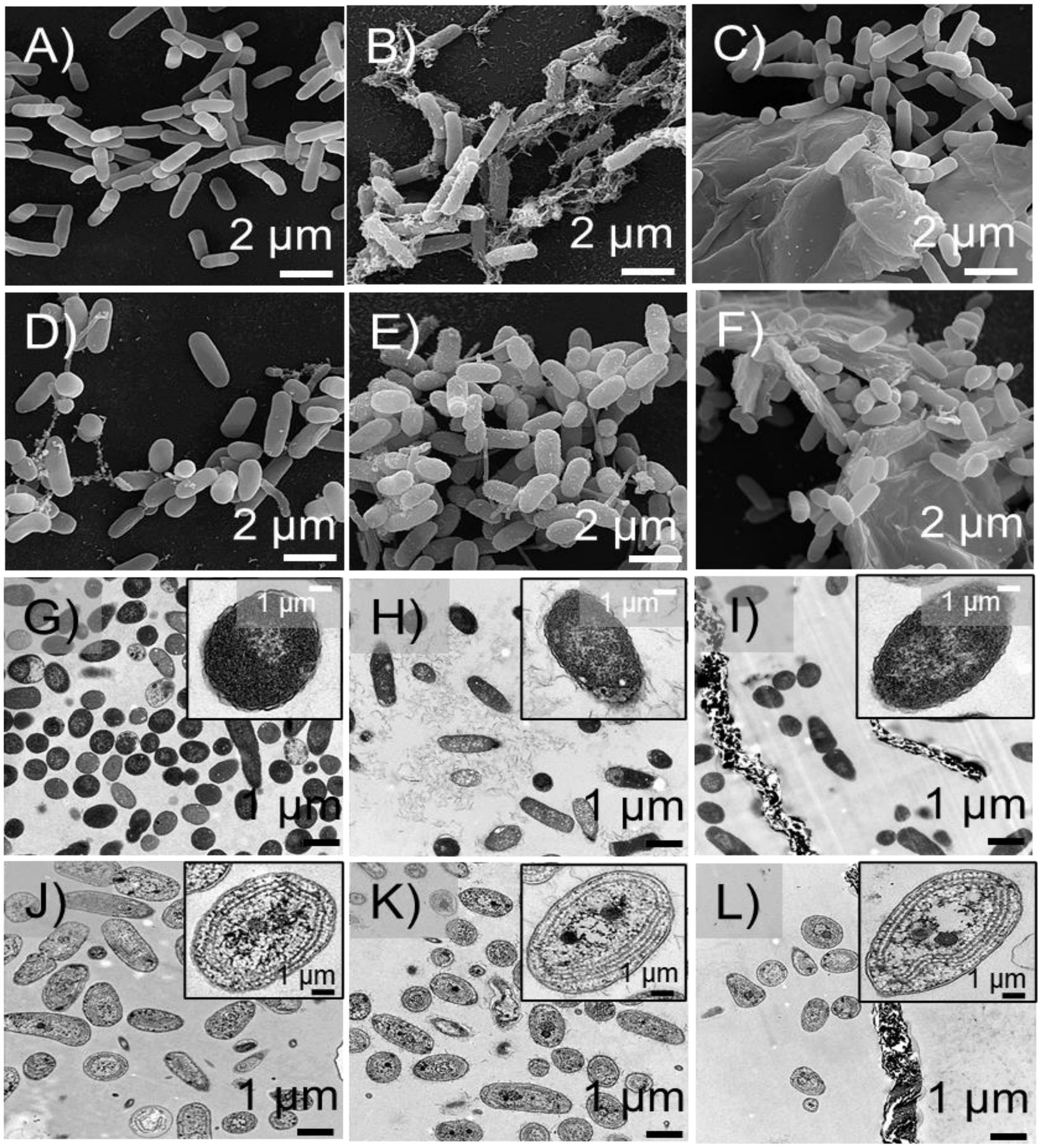

Figure 3.4. Scanning electron micrographs (A-F) and transmission electron micrographs (G-L) of *E. coli* and *M. aeruginosa* cells with and without GBNMs. First and third panels show *E. coli* cells with no GO (A, G); cells exposed to the ARGO EC_{50} concentration (B, H); and cells exposed to the TGO800 EC_{50} concentration (C, I) for 3h. Second and fourth panels show *M. aeruginosa* cells with no GO (D, J); cells exposed to the ARGO EC_{50} concentration (E, K); and cells exposed to the TGO500 EC_{50} concentration for 96h. Inserts in G-L are enlarged pictures of cells representative of the interaction observed.

3.4. Conclusions

Environmental risk assessment requires knowledge of GBNMs toxicity on different trophic levels. Yet current studies primarily focus on a single organism within one taxon. Our study contributes to the current body of knowledge on GBNM toxicity by using the same materials studied in multiple organisms across 3 taxa as well as focuses on the influence of surface chemistry (C/O ratio, specifically) on observed toxicity impacts. The present study, conducted on bacteria, photosynthetic microorganisms, and invertebrates provides valuable information on the individual response to different organisms to a suite of systematically reduced GO materials. Overall, results show that photosynthetic organisms have a higher sensitivity towards ARGO compared to bacteria and invertebrates as observed by lower EC_{50} values. Thermal annealing of the material reduced the toxicity in photosynthetic organisms but increased it in bacteria and invertebrates. These opposing trends between toxicity and oxygen content were investigated using *M. aeruginosa* and *E. coli* and clear differences in the mechanisms of interactions were found for the different materials in these two biological models. On one hand, the toxicity of the GBNMs towards *M. aeruginosa* was characterized by a decrease in overall cellular metabolic activity while, in *E. coli*, ARGO induced significant oxidative stress, evidenced by both H_2DCFDA fluorescence and CAT enzyme activity. These findings emphasize how different surface chemistries and species-specific parameters alter the toxicity of GBNMs and highlight the need to consider the specific response of each organism when developing safe-by-design guidelines for GBNMs, as different organisms will respond differently to changes in the materials' properties.

Supporting Information

Dose-response curves of *S. obliquus* after a 96h exposure with ARGO or TGOs (Figure B.1.); Relationship between GBNMs' hydrodynamic diameter and EC_{50} in each media (Figure B.2.); Compiled literature comparing graphene-based nanomaterials and different species (Table B.1.); XPS data representing the atomic percent of carbon and oxygen content, and carbon-oxygen functional groups (Table B.2.); XPS data representing trace impurities in GBNMs (Table B.3.); Immobilization responses of *D. manga* after exposure to GBNMs (Table B.4.); Chemical composition and concentrations for the preparations of 0.9% NaCl, ISO, and BBM medias (Table B.5.); Solution chemistry characteristics of the different media: BBM, 0.9% NaCl, and ISO (Table B.6.). This material is available free of charge.

Acknowledgements

This work was supported by the National Science Foundation through the CBET-1708681/1709031 awards and the Nanosystems Engineering Research Center for Nanotechnology-Enabled Water Treatment (EEC-1449500). A.B. acknowledges the support of a Dean's Fellowship from the Ira A. Fulton Schools of Engineering, a Scholar Award given by the International Chapter of the P.E.O. Sisterhood, and the Achievement Rewards for Collegiate Scientists Foundation. The authors gratefully acknowledge the use of the characterization facilities within the Electron Microscopy division of the CLAS Bioimaging Facility at ASU, particularly Dr. David Lowry for his help with the TEM and SEM images.

CHAPTER 4

DECOUPLING STRUCTURE AND SURFACE CHEMISTRY IMPACTS OF GRAPHENE-BASED/EPOXY NANOCOMPOSITES AFTER ULTRAVIOLET LIGHT DEGRADATION

Abstract

The ultraviolet (UV)-induced degradation of three structurally different graphene-based /polymer nanocomposites was investigated in this study. Specifically, graphene (G), reduced graphene oxide (RGO) and graphene oxide (GO) were used as nanofillers to assess their effect on the photodegradation of an epoxy coating with a stainless steel support. The polymeric nanocomposites (PNCs) G/epoxy (G/E), RGO/epoxy (RGO/E), GO/Epoxy (GO/E), and the neat epoxy composite were UV-exposed under both dry and humid conditions in the NIST SPHERE, a UV-weathering device that produces a highly uniform UV light, and can control UV dose, temperature, and relative humidity with high precision. The PNCs and neat epoxy were characterized over the time course of UV exposure (0, 3, 5, 10, 20, and 30) days using infrared spectroscopy to assess chemical changes pertaining in its majority to the polymeric chain. Results indicate an increase in absorbance intensity in the carbonyl region (1600-1900) cm^{-1}, more evident in the neat epoxy, RGO/E, and G/E PNCs. In all PNCs, the formation of new peaks in the 1658 cm^{-1} and 1741 cm^{-1} are indicative of photooxidation, yielding carbonyl-containing photoproducts. The effect of photodegradation across PNCs change depending on the nanofiller's surface chemistry, where G/E PNCs seem to be the most beneficial due to graphene's higher UV adsorption ability compared to GO and RGO and has the least release potential due to its hydrophobic nature. Conversely, GO/E PNCs seem to perform the worst, especially under humid UV conditions, where there is a higher potential for GO's release due to its hydrophilic nature.

4.1 Introduction

The stabilization of polymers against high-energy ultraviolet (UV) radiation can be accomplished by the addition of antioxidants and photo-stabilizers.[164] Graphene-based nanomaterials (GBNs) are additives that have been shown to stabilize polymers against UV radiation while providing unique antimicrobial and barrier properties.[165,166] GBNs have also been highlighted as strong candidates for gas-barrier materials because their layered structure does not allow diffusion of small gases through their plane, making gas molecules follow longer and more tortuous pathways to pass through the nanocomposite film.[167–170] Additionally, GBNs are being studied as fillers in polymeric matrices due to their extraordinary mechanical, electrical, thermal, and optical properties, not to mention their intrinsic unique layered structure, large surface area, high aspect ratio, and high compatibility with a broad range of polymers. These properties of GBNs make them ideal candidates when compared to other pigments and fillers.[165,171]

Epoxies are thermosetting polymeric materials that exhibit a high degree of crosslinking, which endows them with useful properties, such as high rigidity and strength. For this reason, epoxies are widely used as adhesives, coatings, and structural materials. The steel industry for example, uses commercial epoxy liners to protect biodiesel tanks against corrosion. Epoxy liners are characterized by their abiotic corrosion resistance and excellent mechanical strength; additionally, they can adhere to a variety of metal substrates [172]. In construction, epoxy adhesives are used in combination with fibers for the external reinforcement of concrete structures, to bond fiber optic or strain gages, to prevent the ingress of deicing salts like sodium chloride[173], to strengthen rebar rods[174], and used to repair concrete cracks and holes (epoxy paste).[175] However, surfaces coated with epoxy resins have free volumes in their structures which make them permeable against corroding agents[166] and often degrade after exposure to sunlight and other external stressors that induce chemical and physical changes.[176,177] Due to the presence of aromatic moieties in the epoxy resins, UV irradiation can be absorbed and lead to coating degradation evidenced by discoloration and chalking.[176] To overcome these limitations while simultaneously applying other beneficial properties (*e.g.*, mechanical strength and corrosion resistance), epoxies have been reinforced with nanomaterials such as nanoclays, nanoparticles, carbon nanotubes, and GBNs.[174,178–181]

GBNs exist in several forms based on their level of oxidation: graphene, reduced graphene oxide (RGO), and graphene oxide (GO). Each GBN form contains sp^2-hybridized carbon atoms linked to each other through a honeycomb lattice structure. Graphene is typically prepared via chemical vapor deposition, cleavage of graphite, or reduction of graphene oxide (GO).[182] GO is composed of a single sheet of graphenic carbon with oxidative modification of the basal plane, usually with a high oxygen content typically characterized by C/O ratios between 2 to 3.[104] The oxygen functional groups found in both GO and its reduced form (reduced GO or RGO) include hydroxyl, epoxy, and carboxyl groups distributed on the basal plane and edges of the carbon lattice, which provide high stability and reactivity. The different extent of oxygen moieties present in the GBN change its compatibility with the polymeric matrix. On one hand, GO is highly polar and can be well-dispersed in aqueous polar solvents, but it is significantly affected by relative humidity[169,183] due to its hydrophilic nature. On the other, graphene, is hydrophobic and provides the nanocomposites with outstanding mechanical properties and UV stability but the synthesis of a large-area, defect-free monolayer graphene is challenging[169] not to mention its hydrophobic nature, making it difficult to exfoliate and disperse in a polymer matrix. The properties of RGO lie between graphene and GO depending on its extent of oxidation, with fewer oxygen functional groups and a greater proportion of graphenic carbon. These chemical changes in the GBNs' structure will eventually change the nanocomposite's overall performance and weathering behavior. The systematic approach of reinforcing epoxy with either graphene, GO, or rGO to assess how the different structural chemistries influences photodegradation resistance has not been evaluated.

GBN/polymer composites can be altered over time by environmental conditions such as humidity, temperature, and UV light, changing their structural and surface properties. Only a few studies have addressed the effect of GBNs on polymer matrix degradation in nanocomposites. As mentioned earlier, one of the most common polymer degradation processes occurs from exposure to UV radiation. Under real environmental conditions, UV-induced degradation is a slow process that can last years. Therefore, to test UV degradation on an experimentally tractable timescale, accelerated weathering devices are used to assess the durability and environmental implications of polymeric nanocomposites. Recently, Goodwin et al. studied the effect of GBNs on polymer matrix degradation. In these studies, a UV weathering device called the NIST SPHERE (Simulated Photodegradation via High Energy Radiant Exposure) was used to simulate UV radiation from sunlight in a uniformed manner with controlled temperature and humidity conditions.[184] In the first study, GO increased the durability of waterborne polyurethane

(WBPU) under dry UV but not under humid UV conditions; additionally, GO became exposed on the nanocomposite's surface with possible release.[185] In another study with similar weathering conditions, the effect of graphene nanofillers on the degradation of a thermoplastic polyurethane (TPU) was investigated. Graphene was found to improve the service life of the polymer under both dry UV and humid UV conditions, but like GO, graphene also became exposed at the surface, with the potential for release.[186] When GO was used as a filler in polypropylene (PP), de Oliveira et al. observed a three-factor increase in photodegradation resistance compared to neat PP.[187] Similarly, high-density polyethylene (HDPE) reinforced with graphene provided higher degradation resistance, as observed by less pronounced changes in the crystallinity, lamellar thickness, molecular weight, and dynamic mechanical properties compared to neat HDPE.[188] Thus, understanding the transformation of polymeric materials containing nanomaterials is essential to predict their performance over time and to determine their useful service life.

Polymers supplemented with GBNs have been investigated for their anticorrosion, antistatic, or antifriction properties in protective paints and coatings applications.[19,189] GBNs provide an additional corrosion resistance to coatings used for corrosion protection which can enable the coatings to last much longer.[170] Singh et al. studied the corrosion resistance of a hydrophobic graphene oxide-polymer composite coating on the copper surface. They found that the GO filled coating behaved as an effective protective shield for oxidation and corrosion of the metal.[190] Similarly, Kirkland et al. investigated the potential for graphene-based coatings to provide barrier performance for aqueous corrosion. They observed that the deposited graphene layers on the metal surface can enhance the corrosion protection of pure metals effectively.[191] Chang et al. found that the addition of graphene into an epoxy coating enhanced its barrier properties and corrosion resistance.[172] No studies to date have shown how the barrier properties of GBN/polymer nanocomposites change as a function of UV weathering.

In this study, a systematic investigation of the UV degradation of GBN/epoxy-based nanocomposites containing three GBNs of different chemical structures (graphene, rGO and GO). The objective of this work was to identify the structural nanocomposite changes caused by solar irradiation that alter the degradability of GBN/polymeric nanocomposites. An accelerated UV-weathering device called the NIST Simulated Photodegradation by High-Energy Radiant Emission (SPHERE) was used to simulate highly uniform UV radiation from sunlight with controlled temperature and humidity conditions. GBN/epoxy nanocomposites were exposed to accelerated UV weathering under both dry and humid conditions and thoroughly characterized before and after UV weathering. Lastly, a comparison of the long-term weatherability of GBN/epoxy nanocomposites was made based on chemical changes of the polymeric matrix, accumulation of GBNs at the nanocomposite surface during weathering, and thickness loss.

4.2. Materials and methods

4.2.1. Reagents. Graphene Oxide (GO) Powder, S Method: GNOS0010 (diameter: [1 to 15] µm; thickness: [0.8 to 1.2] nm; C/O ratio: 1.94), reduced graphene oxide (rGO) GNCR0001 (Monolayer diameter: [0.5 to 10] µm; thickness: 1 nm; C/O ratio: 4.56), and single layer graphene powder GNP1F005 (1-5 atomic layer graphene nanosheets; lateral size: [0.5 to 5] µm; 7% oxygen) were all purchased from ACS Materials. Epoxy Ancarez

AR555 (epoxy resin, solid content: 55%, Part A) and Anquamine 419 (curing agent, solid content: 60%, Part B) were obtained from Air Products and the stainless steel: PRE16195 shim stock, 0.002 thickness and 6 " x 100 " dimensions was purchased from Precision Brand.

4.2.2. Nanocomposite preparation. The target of this study was to prepare polymer nanocomposite films coated on steel surfaces with CNMs loadings of 3 % by mass. Neat polymers (no CNMs) were also prepared as controls. A stoichiometric ratio of 1:1 (epoxy prepolymer:amine) was used to achieve the best corrosion resistance as per the manufacturer. A 3 % by mass CNM dispersion was prepared by adding a known mass of as received powder material directly to the epoxy resin (water based) in a 50 mL Falcon tube and immediately bath sonicating (M3800 Branson Ultrasonic Corporation, Danbury, CT) for 30 min to ensure material dispersion and reduce scission of polymeric chains. After sonication, the dispersion was mixed by hand for 20 min before adding the curing agent. The suspension was thoroughly mixed for another 20 min by hand using a glass-stirring rod and placed in an ice bath. Degassing was done by placing the suspension in a vacuum chamber for 1 h to make sure all the bubbles were removed completely. The mixture was then applied onto the stainless steel substrate using a casting knife and set to a 1 mm thickness. Once the steel was homogeneously coated with the suspension, the sheet was left to dry at room temperature overnight and cured at 110 °C for 30 min the next day. Nanocomposite-coated steel coupons with a 2.5 cm diameter were cut and stored in 50 mL falcon tubes until use. Control polymer-coated steel coupons were prepared in the same manner as described above without the addition of CNM (epoxy only). For brevity, neat epoxy and the nanocomposites will be denoted as E, G/E, RGO/E and GO/E for epoxy, graphene/epoxy, reduced graphene oxide/epoxy, and graphene oxide/epoxy nanocomposites respectively throughout the manuscript.

4.2.3. Nanocomposite exposure to UV radiation. All nanocomposites were UV-exposed at an approximate irradiance of 140 W/m^2 with wavelengths ranging from 295 nm to 400 nm under high temperature and relative humidity (RH) conditions to simulate the worst-case scenarios of degradation. Specifically, samples were UV-exposed at 55 °C under dry (≈ 0% RH) or high (≈ 75% RH) humidity, referred to as Dry UV (DU) and Humid UV (HU) throughout the manuscript. Samples were weathered for (0, 3, 5, 10, 20, and 30) days in the SPHERE, which is the UV dose equivalent ranging from 0 MJ/m^2 to 280 MJ/m^2. These exposure times represent a range between 0 d to about 1 year of outdoor exposure in Southern Florida, where 1 year of UV exposure ~ is approximately 280 MJ/m^2. For each sample type, triplicate specimens were placed on a 17-position sample holder wheel and were held in place using a cover. A circular area of each specimen (16 mm in diameter) was UV-exposed while the remaining outer rings were protected from UV light by the sample holder cover. At each time of exposure, unless specified, samples were removed from the sample holder for analysis. Figure 1 summarizes the experimental setup used in this study as well as the sample configuration in the SPHERE wheel. Samples were also exposed to the same conditions without UV radiation and referred to as Dry Dark (DD) and Humid Dark (HD) throughout the text and were used as a set of controls. Table 4.1. summarizes the different conditions referred to in this study.

Table 4.1. Sample exposure conditions used in this study.

Condition	**UV (%)**	**Temperature (°C)**	**Relative Humidity (%)**
Dry UV (DU)	100	55	0
Humid UV (HU)	100	55	75
Dry Dark (DD)	0	55	0
Humid Dark (HD)	0	55	75

4.2.4. Nanocomposite characterization after degradation. Nanocomposite degradation was assessed for all weathering conditions. Fourier transform-infrared spectroscopy in attenuated total reflection mode (ATR-FTIR) was used to assess changes in the chemical structure of the nanocomposite's polymer matrix. Triplicate specimens were measured with ATR-FTIR (4 cm^{-1} resolution, 128 scans/sample, Nicolet iS50 with diamond type IIa crystal; ThermoFisher Scientific, Whatman, MA). All spectra were baseline corrected with the same number of baseline points, only shifted when necessary (no more than 5 cm^{-1}) due to band broadening and/or band shifting in the infrared (IR) spectra from polymer degradation. All FTIR spectra were normalized to the 1508 cm^{-1} band, which changed minimally during UV irradiation.

Raman spectroscopy (Bruker Senterra XL Raman Microscope, Billerica, MA) was used to collect CNM concentration data at the composite's sub-surface (top 1 µm to 4 µm according to the manufacturer) as a function of UV exposure time. Raman measurements were done at each time point of UV exposure with triplicate samples using a 785 nm laser, 1 mW power, 5 co-additions and 10 s accumulation. Each Raman spectrum shown is the average measurement from three replicate samples, with four different spots measured per sample. Results were baseline corrected using a Concave rubber band method. The ratio of the D to G band intensities (D/G Ratio) was determined to evaluate if a chemical change occurred for the graphene-based NMs at or near the surface of the degraded nanocomposites for each UV exposure time point.

4.2.7. Data analysis and statistics. All experiments were done with at least triplicate samples for each condition arranged as described earlier. Data is shown as means ± standard deviation. Data was processed using Origin 8.5.1 software. The statistical package for social sciences (SPSS) software was used for statistical analysis. Statistically significant differences were determined via a one-way analysis of variance followed by a Tukey post-hoc test with a p-value <0.05.

4.3. Results and discussion

4.3.1. Transformations of the polymeric composite after UV exposure. ATR-FTIR spectroscopy was used to assess the degradation of neat Epoxy and GB PNCs as a function of UV exposure time under dry and humid conditions. The carbonyl region (1600 cm^{-1} – 1900 cm^{-1}) of the FTIR spectrum was used primarily to monitor polymer degradation by photooxidation (Fig. 4.1). Epoxy resins are characterized by a high evolution of CO and CO_2 when photolyzed in an oxygen atmosphere. Other photoproducts formed include ethane, propane and propylene which can all be formed after main chain scission, the primary process that happens after UV irradiation.[193] Under dry UV conditions, new bands in the neat Epoxy appeared as the exposure to UV dose increased (Fig. 4.1.A). This is due to the formation of various carbonyl groups (C=O) like aldehydes and ketones as mentioned earlier. These changes are due to the photodegradation of amine-cured epoxy by UV radiation in the 295-400 nm wavelength, leading to extensive scission of the main epoxy chains. Similar observations can be made in all the GB PNCs, where the same bands are appearing after UV exposure. However, each GB PNC shows a different increase in absorbance. For GO/E (Fig. 4.1.B), the increase in absorbance is not as significant when compared to that of the neat Epoxy (Fig. 4.1.A), indicating less photoproducts are being created in GO/E composites. RGO follows with a higher increase in absorbance as UV exposure increases (Fig. 4.1.B) and then G/E where the increase in absorbance is very similar to that observed in neat Epoxy. These observations align with previous studies where the intensity of the carbonyl region increased more rapidly for a 3% G/TPU PNC[194] than with neat TPU but decreased more slowly in a GO/WBPU compared to the neat WBPU.[195] Upon initial inspection, these results suggest that graphene accelerated Epoxy photooxidation. However, scanning electron micrographs of the previous studies with G/TPU, show that the material loss in neat TPU compared to G/TPU was an order of magnitude larger and that the larger photoproduct build-up observed in the G/TPU was most likely due to less conversion of photoproducts to gas.[194]

Exposure of neat Epoxy and GB PNCs to humid UV conditions led to the formation of the same peaks as those observed in dry UV conditions in the carbonyl region characteristic of epoxy photooxidation (Fig. 4.2.). Overall, the intensity increases in the FTIR spectrum indicated that the formation of photoproducts occurred to a lesser extent when compared to dry UV and followed the same trend where an increase in UV exposure led to an increase in absorbance intensity. However, all GB PNCs seem to have less photoproduct build-up compared to the neat Epoxy (Fig. 4.2.B-D). This is more evident for the GO/E PNCs, where the intensities from 1583 cm^{-1} to 1741 cm^{-1} remained constant with only marginal increases during continued humid UV exposure and very small differences compared to the humid dark controls (Figs. 4.2. B) and C.2.). The G/E PNC follows with a similar trend with almost no changes in intensity for the first exposure times but more evident increases after 20 and 30 days of UV exposure (Fig. 4.2.C)). The RGO/PNC is last with a more visible increase in absorbance intensity most noticeable after 10, 20, and 30 days but still lower than that of neat Epoxy (Fig. 4.2.C).

Interestingly, results indicate less degradation (in RGO/E), slight degradation (G/E), or even no degradation (GO/E) under humid UV conditions. The decrease in degradation of the G/PNC and perhaps on the RGO/E is expected and these results align with what was observed in dry UV conditions. In fact, for the G/TPU PNCs studied in very similar conditions, the addition of graphene slowed down the TPU photodegradation rate or improved the service life of TPU by ten times in both dry UV and humid UV conditions. The trends observed with the GO/E PNCs align with Goodwin et al. results where they observed no changes in absorbance intensity in a GO/WBPU PNC in humid UV after 140 days of exposure. They attributed this behavior to the steady-state photoproduct formation and their removal as gas. Thickness loss measurements in GO/WBPU indicated that these PNCs lost over 44 µm of material from humid UV degradation and that the photoproducts present in the FTIR spectrum were formed and removed over time in the presence of moisture.[195] This is an important observation because it indicates that the GO is being released, especially in humid UV conditions where the release of GO increased due to its hydrophilic nature which enables its interactions with moisture.

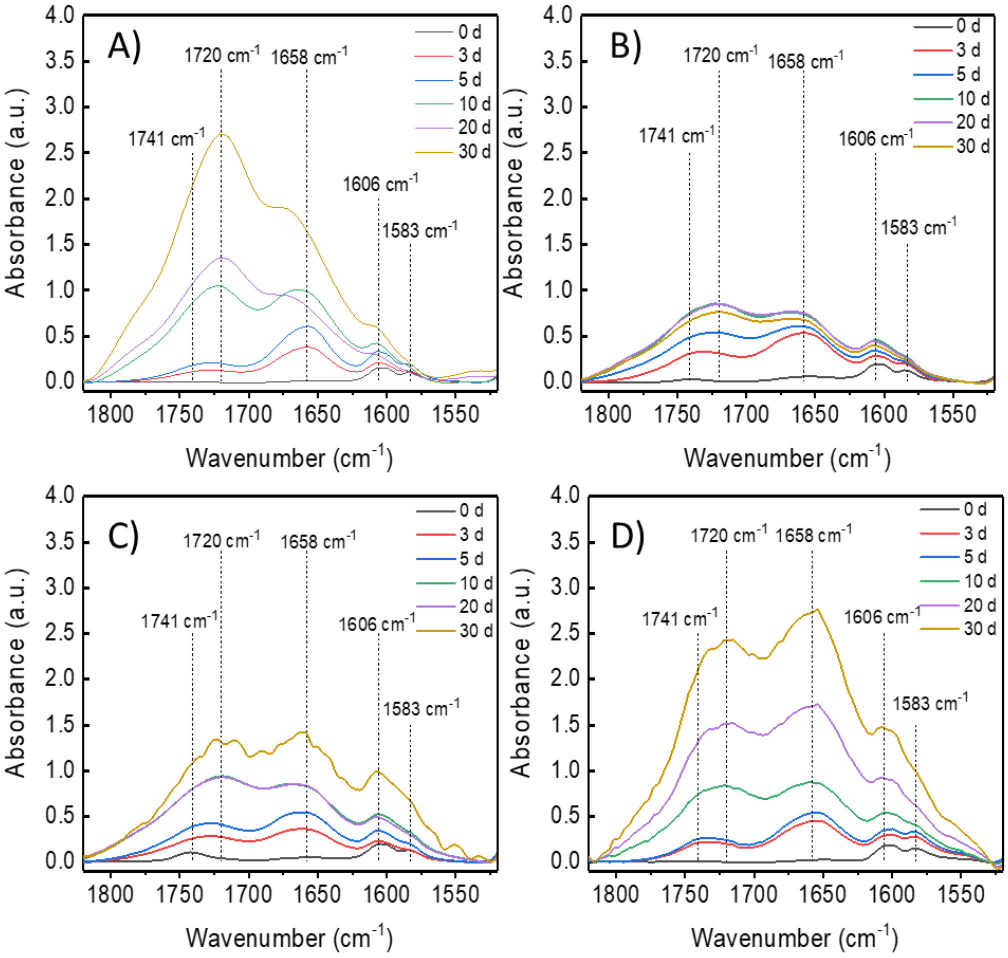

Figure 4.1. The carbonyl region in the FTIR Spectrum of neat Epoxy and GB/E PNCs at different time points of dry UV exposure. The neat epoxy A) and GO/E PNC B) are shown in the top panel and the RGO/E C) and G/E PNCs D) are shown in the bottom panels. The FTIR data is presented as the average of one measurement per specimen for triplicate specimens.

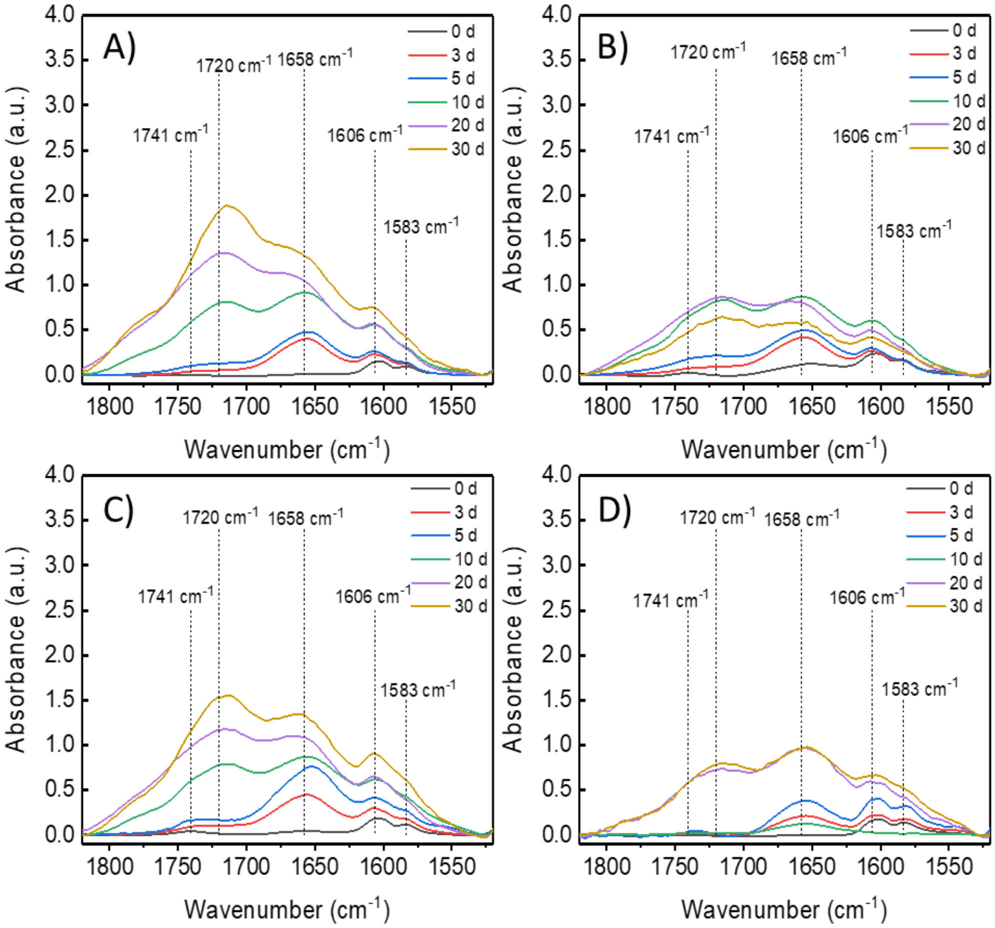

Figure 4.2. The carbonyl region in the FTIR Spectrum of neat Epoxy and GB/E PNCs at different time points of humid UV exposure. The neat epoxy A) and GO/E PNC B) are shown in the top panel and the RGO/E C) and G/E PNCs D) are shown in the bottom panels. The FTIR data is presented as the average of one measurement per specimen for triplicate specimens.

4.3.2. Transformation of GB-NMs after UV exposure. UV-induced transformations of the GB/NMs, on or near the nanocomposites' surface were assessed using Raman spectroscopy. The G/E PNCs show one peak at 1311 cm^{-1} attributable to the aromatic sp^2 carbon structure, or G band. In comparison, the GO/E and RGO/E PNCs show the emergence of a strong D band at 1602 cm^{-1}, originating from the presence of defects and disorder in the carbon aromatic structure.[196] These defects are identified as being oxygen-functional groups like hydroxyl, carbonyl, carboxyl, and epoxy groups. These functional groups, which are negatively charged, provide electrostatic repulsion between the GO sheets and allows for an easier dispersion in the polymeric matrix, compared to graphene. Based on X-ray Photoelectron Spectroscopy data, the carbon to oxygen (C/O) ratio of each GB NM is 12.9, 8.33, and 2.67 for graphene, RGO, and GO, respectively. To assess the relative amount of disorder present in the PNCs' surface (top 1 to 4 μm), the intensity ratio of the Raman D and G bands (I_D/I_G) was calculated in all weathering conditions (Figs. 4.3, 4.4, C3, and C4). Under both dry UV and humid UV conditions, a similar decrease in the I_D/I_G ratio was observed for GO/E and RGO/E, indicating some UV-induced chemical reduction of the GB nanofillers or the loss of oxygen functional groups on the nanofillers' surface.

In dry UV conditions (Fig. 4.3), the I_D/I_G ratio decreased significantly after 20 and 30 days of UV exposure both RGO/E and GO/E compared to before UV exposure (0 days). For RGO/E the I_D/I_G ratio changed from 1.65 ± 0.24 at 0 days to 0.97 ± 0.28 at 20 days and 0.72 ± 0.28 at 30 days of exposure (Fig. 4.3.B)). Similarly, for GO/E the I_D/I_G ratio decreased from 1.75 ± 0.16 for 0 days, to 1.36 ± 0.37 at 20 days, and to 1.02 ±0.35 after 30 days of exposure (Fig. 4.3.A). Additionally, in these PNCs, an increase in I_D/I_G ratio was observed at the earliest exposure times (3 and 5 days) perhaps due to GO fragmenting as observed elsewhere.[195] As stated earlier, the I_D/I_G ratio is an indicator to assess the relative amount of disorder, and with graphene, in the G/E PNC lacking a D band, the I_D/I_G ratio did not change (Fig. 4.3. C)and remained with an average of 1.53 ± 0.11.

The humid UV conditions showed a significant decrease in the I_D/I_G at an even earlier exposure time point for both RGO/E and GO/E PNCs (Fig. 4.4.). For RGO/E, the I_D/I_G ratio before UV exposure was 1.64 ± 0.35, but after 10, 20, and 30 days the ratio decreased to 0.72 ± 0.30, 0.99 ± 0. 43, and 0.73 ± 0.36, respectively (Fig. 4.4.B). For GO/E, the I_D/I_G ratio decreased from 1.77 ± 0.16 before UV exposure to 1.22 ± 0.22, 0.94 ± 0.94, and 0.84 ±0.41 after 10, 20, and 30 days of exposure. In the other two weathering conditions, the dry dark and humid dark, the I_D/I_G ratio did not change in any of the PNCs (Figs. C.3. and C.4.), thus indicating that the reduction of the GB NMs was attributed to the photoreduction generated by UV light.

Similar results have been observed in previous studies, where GO/WBPU was photoreduced after 140 days of UV exposure in both dry and humid UV conditions.[195] Moreover, studies have shown that GO phototransforms rapidly under UV exposure, resulting in reduced materials similar to RGO, CO_2, and low molecular weight (LMW) species.[197] A recent study, also shows that functional groups present in the GB NMs influence their degradability after UV exposure, where GB NMs with higher oxygen-containing functional groups on their basal planes (epoxy and hydroxyl groups) will photodegrade faster than those GB NMs with lower oxygen functional groups.[198]

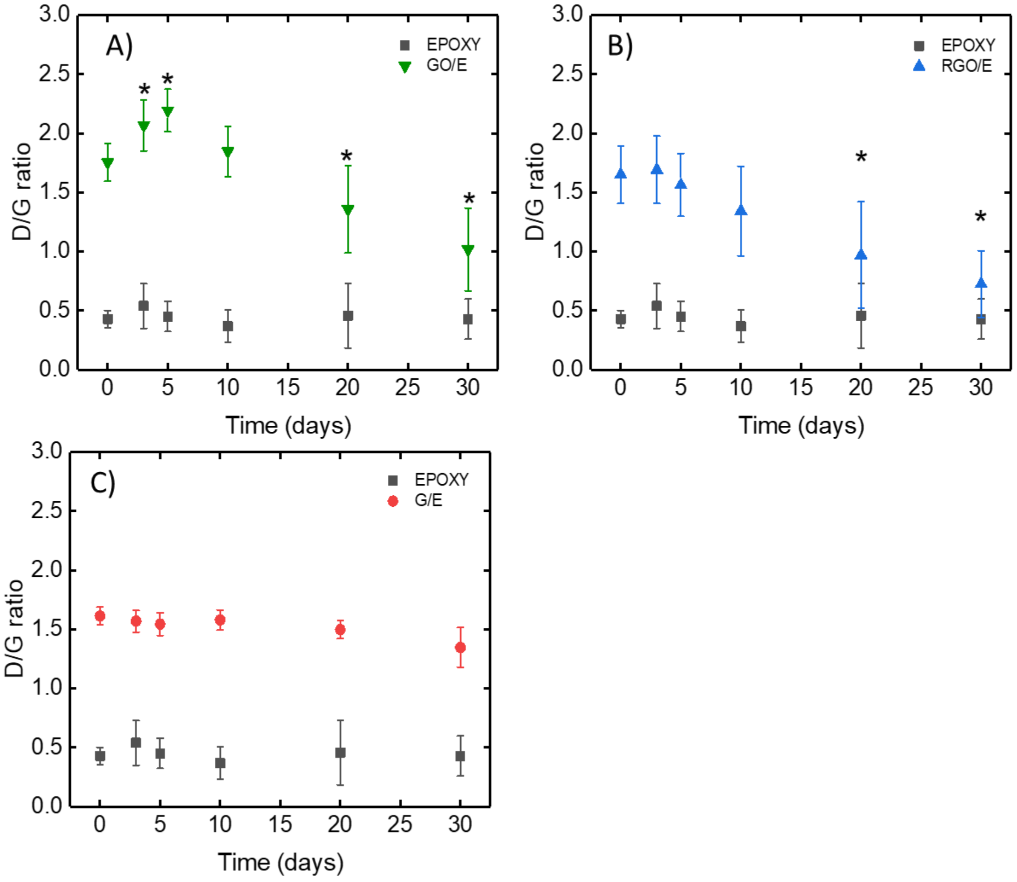

Figure 4.3. The D band (1311 cm^{-1}) to G band (1602 cm^{-1}) intensity ratio at different time points of dry UV exposure. Each data point represents the average and standard deviation of three replicate specimens, with measurements of four areas per replicate specimen.

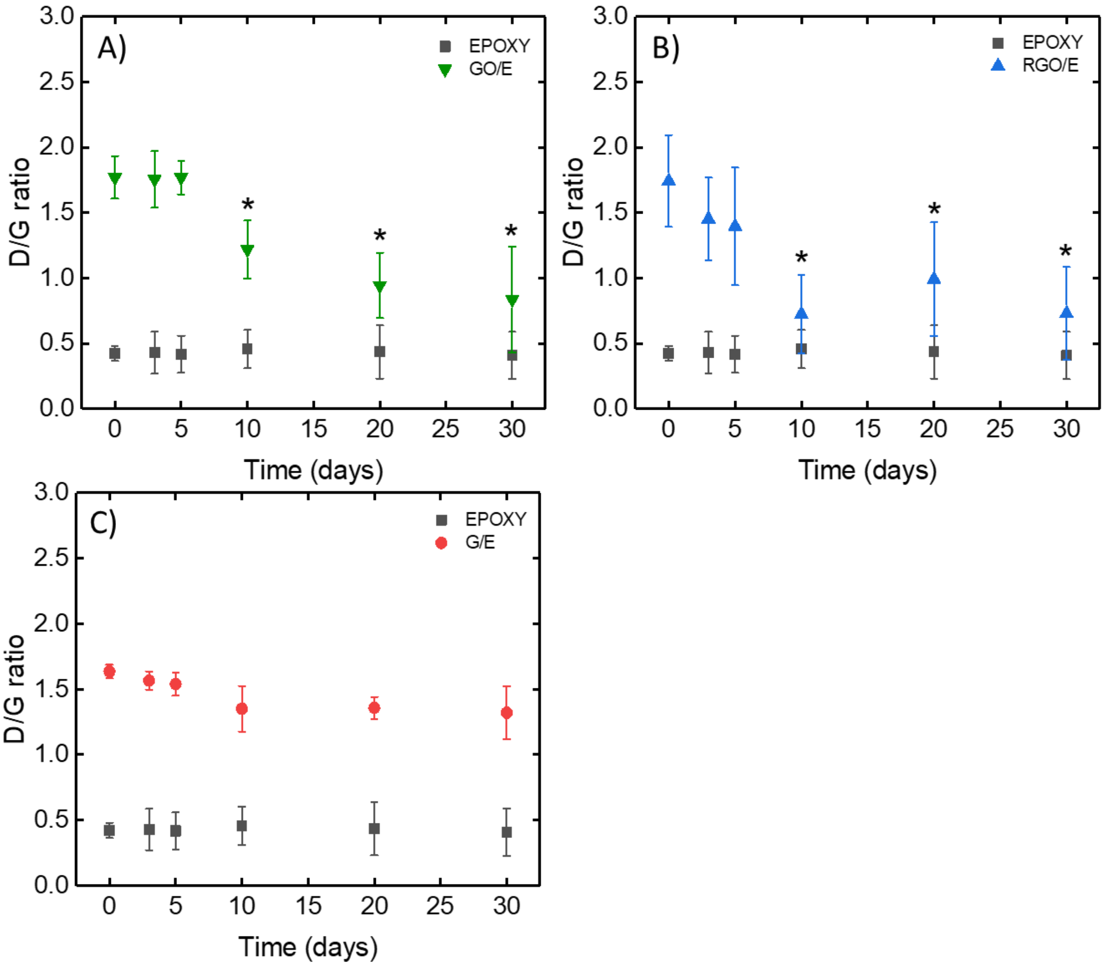

Figure 4.4. The D band (1311 cm^{-1}) to G band (1602 cm^{-1}) intensity ratio at different time points of humid UV exposure. Each data point represents the average and standard deviation of three replicate specimens, with measurements of four areas per replicate specimen.

4.4. Notable observations and trends. GB NMs have been studied as potential nanofillers in polymeric composites due to their enhanced barrier properties compared to neat polymers. However, the extent to which changes in their surface chemistries (more oxidized vs more reduced) regulate polymer degradation during exposure to a combination of UV radiation and moisture is still unknown. This study evaluated the effect of three structurally different GB NMs, namely graphene, RGO, and GO on polymer degradability under both humid UV and dry UV conditions. FTIR data indicates that under both conditions, the graphene PNCs slowed down the photodegradation of epoxy by reducing photoproduct build up. Also, due to its hydrophobic nature, both FTIR and Raman data show that it is less likely for it to be released. On the other hand, the GO PNCs seem to slow down epoxy photodegradation in dry UV conditions but not in humid UV conditions. This is attributed to the hydrophilic nature of GO, which enables it to be released to moist/humid conditions. Raman data also showed that the GO and RGO PNCs were undergoing significant photoreduction both humid and dry UV conditions as observed by a decrease in I_D/I_G, where photoreduction happened starting 10 days of humid UV exposure. Thickness loss measurements are still required to qualitatively assess the degradability of the GB PNCs compared to neat Epoxy. However, the trends observed in this study align with previous studies where: 1) new bands are formed in the carbonyl region after UV photodegradation attributed to main chain scission and the subsequent formation of photoproducts like aldehydes and ketones; 2) graphene has a higher photoproduct build up, leading to less conversion of photoproducts to gas and 3) GO and RGO are photoreduced after UV exposure; the photoreduction might be related to the oxygen functional groups present in each GB NM.

The higher stability of G/epoxy PNCs compared to neat epoxy and GB PNCs can procured by various aspects:[194]

1) Graphene is hydrophobic and upon incorporation to the polymer matrix, it can potentially reduce the number of water adsorption sites and slow down the extent of moisture-induced photodegradation of the polymeric matrix.

2) Graphene can absorb UV light and prevent absorption of UV light by the polymer matrix.

3) Graphene can potentially scavenge radicals produced in the polymer, reducing photooxidation rate.

Supporting Information

Figure C.1. The carbonyl region of the FTIR spectrum of GB PNCs of humid dark exposure. Figure C.2. The carbonyl region of the FTIR spectrum of GB PNCs of dry dark exposure. Figure C.3. The D band (1311 cm^{-1}) to G band (1602 cm^{-1}) intensity ratio at different time points of dry dark exposure. Figure C.4. The D band (1311 cm^{-1}) to G band (1602 cm^{-1}) intensity ratio at different time points of humid dark exposure.

Acknowledgements

This work was supported the National Science Foundation, through the Nanosystems Engineering Research Center for Nanotechnology-Enabled Water Treatment (EEC-1449500). A.B. acknowledges the support of a Dean's Fellowship from the Ira A. Fulton Schools of Engineering, a Scholar Award given by the International Chapter of the P.E.O. Sisterhood, and the Achievement Rewards for Collegiate Scientists Foundation.

CHAPTER 5

INCREASED BROMIDE REMOVAL IN GRAPHENE-SILVER COMPOSITES: ROLE OF PARTICLE SIZE AND CARBON STRUCTURE

Abstract

Bromide (Br^-) is a non-toxic halogen found in surface water at concentrations from 14-200 µg/L. However, in the presence of organic matter and oxidants during the water disinfection process, Br- can form cyto- and genotoxic disinfection by-products (DBPs). Current Br- removal technologies are often non-specific and costly due to the need of specialized equipment. Recently, the use of silver (Ag) to precipitate Br- as insoluble AgBr salts was proposed as an alternative to traditional adsorbents; however, the cost of Ag and competition from other ions reduce the applicability of silver for Br- removal. In this study, we report a new alternative: an Ag-impregnated graphene oxide (GO) nanocomposite that reduces the amount of silver needed for Br- removal. GO was impregnated with ionic Ag (GO-Ag^+) or nanoparticulate Ag (GO-nAg) to obtain two different nanocomposite materials and identify design properties that enhance the Br- removal efficiency. In deionized water, Ag+ and 20 nm Ag NPs had the highest Br- removal capacity (>0.89) followed by the GO-nAg (T-40) with a removal capacity of 0.77 mol Br^-/ mol Ag^+. In synthetic fresh water, the removal capacity reduced for all composites due to the presence of competing ions. Nonetheless, T-40 and the 20 nm Ag NPs had the highest removal capacities (>0.50). Similarly. In anoxic conditions, the T-40 and the 20 nm Ag NPs outperformed the ionic counterparts indicating that the dissolution of Ag NPs to Ag^+ and further complexation with Br^- was not the only mechanism taking place to remove Br^-. Jar tests show that Ag can be removed via coagulation, but the GO-nAg has the least Ag remaining in the water, thus suggesting that the carbon support facilitates Ag removal, and it is an important optimization parameter compared to the utilization of Ag NPs alone.

5.1. Introduction

Water disinfection is one of the most important achievements in public health from the last century. Disinfection provides safe drinking water and reduces the incidence of waterborne diseases like typhoid and cholera.[199] However, disinfection has a major drawback: carcinogenic and reproductive health effects have been associated with the disinfection byproducts (DBPs) formed during the process.[200] Chlorination, the most widely used disinfection process, along with chloramination and ozonation, produce potentially harmful DBPs.[201] Some of these DBPs are created when halides (Cl^-, Br^-, I^-), which occur naturally in surface waters, reacts with oxidants, natural organic matter, and disinfectants. These reactions form inorganic (bromate, BrO_3^-) and organic DBPs like trihalomethanes (THMs) and haloacetic acids (HAAs) in wastewater effluents that are relased into surface waters.[202,203] Once formed, halogenated DBPs remain in the water, reach distribution systems, and end up in the tap water used by consumers.[202] Environmental Protection Agency (EPA) regulations establish that THMs and HAAs cannot exceed concentrations of 80 µg/L and 60 µg/L, respectively.[204]

Studies have shown that brominated-DBPs (Br-DBPs) are more cyto- and genotoxic in mammalian models than their chlorinated counterparts.[25,26,205] Therefore, preventing their formation or ensuring their removal is critical for a safe drinking-water supply. Bromide (Br^-) is found in surface waters at concentrations ranging from 14-200 ug/L.[203] Other Br^- sources include seawater intrusion, with concentrations of 65,000 µg/L and anthropogenic sources like effluent from coal-fired power plants, hydraulic fracturing, and textile production.[206,207]

DBP control typically relies on removal of the organic precursors from water, either before or after disinfection. However, an alternative way to reduce DBPs is to maximize the removal of the *inorganic* precursors, such as chloride, bromide, and iodide.[208] Currently, bromide is removed from water using RO membranes, electrolysis, ion exchange, or adsorptive techniques like impregnated activated carbons.[209] These techniques have a high capital cost, especially in full-scale applications, because they require the installation of specialized units, and may lack sensitivity to Br^- and thus require high doses in real world scenarios. [210]

An alternative to the methods above would be removing bromide by adding silver salts in the drinking-water treatment plant. Silver salts form insoluble AgBr precipitates ($Ag^+ + Br^- \rightarrow AgBr(s)$, $K_{sp} = 5.2 \times 10^{-13}$). The use of silver-amended activated carbons[28], silver-amended graphene oxide[29], and silver aided coagulation practices[211] have shown good bromide removal capacity in synthetic water. Although silver is an expensive metal, silver-assisted coagulation has the advantage of not requiring any specialized equipment, making it ideal for periodic or seasonal spikes of bromide in the water. A recent study showed that silver-impregnated activated carbon is a promising technique for bromide removal.[28] However, natural organic matter and other ions in water affect the material's capacity and specificity. To eliminate this constraint, Kidd et al. used silver-impregnated graphene oxide (GO) to increase the bromide removal even in the presence of competing ions like chloride, sulfate, and organic matter. They concluded that the resulting high performance of GO was due to the more open structure of the 2-dimensional GO sheet, as compared to the activated carbon. Yet, the bromide removal capacity remained low. Thus, for efficient bromide removal in complex waters high concentrations of silver are still required.

This research investigated several design parameters for silver-impregnated graphene materials, with the objective of providing a more selective and cost-effective platform for bromide removal in complex waters. The importance of the GO structure and the form of silver added were systematically investigated. The specific objectives of the study were to: (1) functionalize GO with either silver ions or nanoparticles, (2) compare Br^- removal efficiency of GO impregnated with silver ions versus GO impregnated with silver nanoparticles, and (3) examine the effect of water chemistry on Br^- removal by GO-Ag.

5.2. Materials and Methods

5.2.1. Reagents. Graphite (CAS #7782-42-5, 99.6%), phosphorous pentoxide (P_2O_5, CAS #1314-56-3, 99.0%), sodium borohydride ($NaBH_4$, CAS #16940-66-2, 99%), and hydrochloric acid (HCl, CAS #7732-18-5, 37%) were purchased from Acros Organics. Potassium persulfate ($K_2S_2O_8$, CAS #7727-21-1, 99.0% purity), and potassium permanganate ($KMnO_4$, CAS #7722-64-7, 99.0%) were purchased from Alfa Aesar. Sodium chloride (NaCl, CAS #7647-14-5, 99.5%), potassium chlorate ($KClO_3$), and silver nitrate ($AgNO_3$, CAS #7761-88-8) were purchased from Sigma Aldrich. Sodium bromide (NaBr, CAS #7647-15-6, 99%) was purchased from EM Science and sulfuric acid (H_2SO_4, CAS #7664-93-9) from Fisher Scientific. Nanopure water was collected from a Water Purification System (18.20 MΩ·cm, Thermo Fischer Barnstead GenPure xCAD Plus Water Purification System, Art no. 50136170). Ag NPs of 20-30 nm (Product # 0118XH, 99.95%), 50-60 nm (# 0121XH, 99.95%), 100 nm (# 0115CY, 99.95%), 200-400 nm (# 0124DX, 99.9%), and 500-800 nm particles (#0125DX, 99.9) were all purchased from SkySpring Nanomaterials, Inc (Houston, TX). Unless specified, all the other reagents were purchased from Fisher Scientific.

5.2.2. Graphene oxide synthesis.

Three different methods were used to synthesize three kinds of GO: Tung (T), Marcano (M), and Staudenmaier (S). For the *modified Hummers method* described by Tung,[212] 1g of graphite powder was dispersed in 5 mL of concentrated sulfuric acid (H_2SO_4), and pre-oxidized using 1g of potassium persulfate ($K_2S_2O_8$) and 1g of phosphorous pentoxide (P_2O_5). This suspension was maintained at 80 ºC for 4.5 h, poured into 160 mL of nanopure water, and allowed to rest and cool to room temperature overnight. The pre-oxidized graphite powder was collected by vacuum filtration using a 0.45 µm Polytetrafluoroethylene (PTFE) membrane (Millipore), washed with nanopure water, and dried overnight at room temperature. Then, 40 mL of concentrated sulfuric acid, and 5g of potassium permanganate ($KMnO_4$) were slowly added to the graphite suspension, and the vessel was placed in an ice bath. Ice was added to prevent the temperature from exceeding 10 ºC. After the $KMnO_4$ addition, the mixture was heated slowly to 35 ºC and left to react for 2.5 h. Nanopure water (77.0 mL) was carefully added into the suspension, keeping the temperature $\leq$ 50 ºC. After water addition, the mixture was left to react for an additional 2 h at room temperature. The solution was poured into 240 mL of nanopure water, and 4.2 mL of H_2O_2 (30%) were added, which turned the solution bright yellow. The solution was kept at room temperature for 2 days, and the precipitate was recovered by centrifugation

(12,000 x g, 30 min), and washed twice with 100 mL of a 1:10 HCl solution, and then with nanopure water, to remove residual chemicals. The resulting material was re-suspended in DI water and dialyzed with Fisherbrand® dialysis tubing (molecular weight cut-off 3,500 Da) for 3 days for additional purification. The final dark-brown GO suspension was freeze-dried with ethanol, placed in a lyophilizer for 5 days, and stored at room temperature until use.

For the *Marcano method*[213], 1 g of graphite was added to 200 mL of a 9:1 mixture of H_2SO_4:H_3PO_4 and bath sonicated (M3800 Branson Ultrasonic Bath, Emerson, Danbury, CT) for 5 min. The reaction vessel was placed in an ice bath, and 6 g of $KMnO_4$ were slowly added to the mixture under constant stirring. The solution was heated to 50 ºC and stirred for 12 h. The temperature was strictly kept at 50 ºC because of the presence of manganese heptoxide (Mn_2O_7), which is formed by adding $KMnO_4$ to a concentrated sulfuric acid and can detonate at temperatures higher than 55 ºC. Next, the solution was cooled to room temperature overnight and poured into iced DI water (~400 mL) with 3 mL of hydrogen peroxide (H_2O_2). The precipitate was then washed in succession with 100 mL of DI water (2x), 100 mL of 1:10 HCl (2x), and 100 mL of DI water. After each washing step, the mixture was centrifuged (12,000 x g, 30 min) and the supernatant decanted until the pH was equivalent to that of the DI water (~4.0). Next, the material was purified by dialysis (3,500 Da membranes) for 72 h. The final dark-brown GO suspension was freeze-dried with ethanol, placed in a lyophilizer for 5 days, and stored at room temperature until use.

For the *Staudenmaier method*[13,214], 17.5mL of concentrated sulfuric acid (98%) and 9mL of nitric acid (>90%) were combined in a bulb-flask with a magnetic stirrer. The mixture was cooled to 0 ^oC for 15 minutes. Then, 1g of graphite was added to the mixture under vigorous stirring to prevent agglomeration. Over a 15 minute interval, 11g of $KClO_3$ was added to the mixture at 0^oC. This reaction will synthesize GO from graphite by utilizing the oxidizing potential of potassium chloride with strong acids, sulfuric and nitric. [Caution! Addition of the potassium chlorate results in the formation of chlorine dioxide gas, which can explode at high concentrations. Keeping the reaction vessel cool and adding the $KClO_3$ slowly can help minimize the risk of explosion]. After the potassium chlorate is completely dissolved, the bulb-flask was loosely capped to allow the evolution of gas, and the mixture was stirred for 96 hours at room temperature. When the reaction was complete, the mixture was added to 1L of nanopure water and washed with a 5% HCl solution. After each washing step, the mixture was centrifuged (12,000 x g, 30 min) and the supernatant decanted until the pH was equivalent to that of the DI water (~4.0). Next, the material was purified by dialysis (3,500 Da membranes) for 72 h. The final dark-brown GO suspension was freeze-dried with ethanol, placed in a lyophilizer for 5 days, and stored at room temperature until use.

5.2.3. **Silver impregnation onto graphene oxide.**

Silver ions were impregnated on all three types of GO described above. Silver nanoparticles were nucleated only on the Tung GO.

Silver ions. To impregnate the graphene oxide with silver ions, 200 mg of the GO powder were soaked in 10 mL of a high or low concentration of silver nitrate ($AgNO_3$). A

0.5 M $AgNO_3$ solution was used as a high concentration and 0.01 M $AgNO_3$ as a low. The carbon-silver slurries were stirred for two days at 150 rpm at room temperature. Then, they were centrifuged for 30 minutes at 12,000 x g. The supernatants were removed from the centrifuge tubes, using Pasteur pipettes, and replaced with 50 mL of nanopure water for rinsing. The carbon slurries with nanopure water were re-suspended with a vortex mixer and separated by repeating the centrifuge step. To ensure removal of excess silver, the resulting material was cleaned, using Fisherbrand® dialysis tubing (molecular weight cut-off 3,500 Da), for 3 days. The silver-impregnated carbons were dried at 90 ºC under vacuum and stored in a sealed container at room temperature.[28,29]

Silver nanoparticles. The GO-Ag nanocomposites were prepared following the protocol by de Faria et al.[215] and used silver nitrate ($AgNO_3$) as a salt precursor and sodium borohydride ($NaBH_4$) as a reducing agent. To test GO-Ag nanocomposites with different particle size, the reducing agent was added at different concentrations including 0.2, 0.1, 0.05, and 0.025 M. For the GO suspension, 12.5 mg of the material were dispersed in 43.75 mL of nanopure water, followed by 30 min of bath sonication (Bransonic Model M3800). Then, 8.65 mg of $AgNO_3$ were dissolved in 5 mL of DI water and added to the GO suspension.

5.2.4. Material characterization.

Pristine and silver-impregnated GOs were comprehensively characterized by spectroscopic and microscopic methods to characterize the size, oxidation degree, and graphitic nature of the GO sheets. Ultraviolet-visible spectroscopy (UV-Vis; Horiba Scientific Aqualog) was used to detect the formation of GO-Ag nanocomposites. A suspension of 50 µg/mL was bath sonicated (M3800 Branson Ultrasonic Corporation, Danbury, CT) for 1 h to ensure proper material dispersion. Raman spectroscopy was performed on a custom-built Raman spectrometer operating with a 532 nm laser in a 180° geometry at the Eyring Materials Center at ASU to verify the GO structure. X-ray photoelectron spectroscopy (XPS) was performed on a VG 220i-XL (Thermo Fisher Scientific Ltd. Hampton, NH) equipped with a monochromated Al K-alpha X-ray source. XPS was used to quantify the carbon to oxygen (C:O) ratio and data was analyzed using the CasaXPS software (version 2.3.18). For microscopy analysis, 5 µl of each GO dispersion was added to a new copper grid. Transmission electron microscopy (TEM) was performed on a CM200-FEG (Philips), operating at an acceleration voltage of 200 kV. TEM was done to determine the size and morphology of the nanoparticles. ImageJ was used to process size distribution data.

5.2.5. Bromide removal experiments and solution preparation.

The Br^- stock solution was prepared in a clean plastic bottle by dissolving sodium bromide (NaBr) in nanopure water to reach a final concentration of 20 mg/L. Fresh water was prepared in the laboratory using DI water (conductivity < 1 µs/cm) and adjusted to a pH of 7.5 with HCl. The constituents and their concentrations are shown in table D.1.

Bromide removal experiments were done in triplicate-125 mL plastic vials that were shaken using an in-house end-over-end rotational mixer (45 rpm) as per Kidd et al.[29] Bottle-point experiments used a 4-hour contact time, which represented the hydraulic residence time (HRT) for PAC treatment at water treatment plants.[216] Each material was added to a concentration of 25 mg/L and spiked with 200 µg/L Br^- in two different water matrices: 1) nanopure water, and 2) fresh water. After mixing, 10 mL of each sample were filtered using a 0.2-µm nylon filter (Thermo Scientific F2500-2) and collected in 15 mL Falcon tubes for ion analysis. Additionally, commercial Ag NPs of 20, 50, 100, 200, and 500 nm were used in the same way as the functionalized GO-Ag composites to test whether the carbon support and particle size influenced the Br^- removal capacity. These Ag NPs were used as a powder and directly added to the 125 mL plastic vials. The initial dose of Ag NPs was determined according to the initial Ag dose quantified on the GO-Ag composites. Similarly, a silver salt ($AgNO_3$) as an Ag ion source (Ag^+) was compared to test the efficiency of the Ag^+ at removing Br^- compared to any of the nanocomposites or Ag NPs.

A set of materials were selected based on their capacity at removing Br^- from aerobic conditions in both water matrices. The same set of experiments were done under anoxic conditions to test the effect of Ag NP dissolution on the Br^- removal efficiency. These experiments took place in an anaerobic glove chamber (Coy laboratory products Inc., Grass Lake, MI) in an atmosphere of 3.5% H_2 and 96.5% N_2. The dissolved oxygen in both water matrices were below 0.42 mg/L.

5.2.6 Jar Test

To simulate water treatment processes, jar testing was done using fresh water as the background matrix. Experiments were conducted in 2-L jar testers (Philips and Bird) filled with 1 L of fresh water and initially mixed for 6 min at 200 rpm, simulating coagulation (i.e. rapid mixing). During this step, 28 mg/L of alum and each carbon adsorbent or Ag NPs were added as a powder to a concentration of 25 mg/L. The mixing speed was decreased to 25 rpm for 30 min to simulate flocculation. Mixing ceased and the flocs were let to settle for 1h, simulating sedimentation. No additives were used during the slow mixing and sedimentation steps. After sedimentation, an aliquot was collected for analysis from the middle of the jar using a 50 µL plastic syringe, making sure the sediment was not disturbed. Samples were then placed in 50 mL Falcon tubes and filtered for further analysis. Experimental conditions and sample identification are depicted in Table 5.1. The sample IDs will be used throughout the manuscript.

Table 5.1. Experimental conditions and sample identification. Sample ID was determined depending on the silver loading, type of material or particle size. For silver loading: L for low (0.01 M $AgNO_3$), H for high (0.05 M $AgNO_3$); type of GO: Tung (T), Marcano (M), and Staudenmaier (S). The GO-nAg were synthesized using low silver loading and Tung GO, therefore, the ID was determined according to the particle size (40-9 nm). Commercial Ag NPs were identified according to the size stated by the manufacturer (20-500 nm).

	[$AgNO_3$]	Material	Sample ID
GO-Ag^+	0.01M (Low)	Tung	L-T
		Marcano	L-M
		Staudenmaier	L-S
	0.5 M (High)	Tung	H-T
		Marcano	H-M
		Staudenmaier	H-S
GO-nAg	0.01M	Tung - 40 nm	T-40
		Tung - 18 nm	T-18
		Tung - 25 nm	T-25
		Tung - 9 nm	T-9
		20 nm	20

Commercial Ag NPs	50 nm	50
	100 nm	100
	200 nm	200
	500 nm	500

5.2.6. Ion quantification in pristine and fresh waters.

Samples were filtered using a 0.2 µm nylon filter. Filtered samples were analyzed for Br$^-$ and Ag$^+$ using Inductively Coupled Plasma Mass Spectroscopy (ICP-MS) to measure anions remaining in solution. To determine Br$^-$ concentrations, samples were diluted by 2x with 0.1% trace metal grade NH$_4$OH, a non-acidified 100ppb Ga internal standard was used, and ^{79}Br was assessed. For Ag$^+$, samples were diluted by 10x and acidified in 2% HNO$_3$ and ^{107}Ag was measured.

5.2.7. Data analysis and statistics. All experiments were done using triplicate samples and in three independent trials. Means and standard deviations were estimated for each treatment. A one-way analysis of variance followed by a Tukey post-hoc test was used to determine significant differences across treatments with a p value ≤ 0.05.

5.3. Results and Discussion

5.3.1 Material characterization of GO-Ag composites. Table 5.2. summarizes the characterization data for the GO adsorbents before and after silver impregnation at low or high concentrations of AgNO$_3$. Raman spectroscopy detected the characteristic D and G bands of carbonaceous materials at 1320 cm^{-1} and 1570 cm^{-1}, respectively. The D band is derived from the structural imperfections or defects created by the attachment of oxygen functional groups like hydroxyl and epoxide on the GO's basal plane[217] whereas the G band is related to the sp^2-bonded carbon lattice. As such, an increase in D:G ratio indicates an increase in defects on the GO's surface. Results show that the D:G ratio is in the order of T GO> M GO> SGO, where the ratios are 0.98, 0.82, and 0.80, respectively, indicating high disorder in the oxidized carbon. A similar trend is observed for the functionalized GOs. These results correlate with the amount of oxygen functional groups present in the materials' surface as shown by the carbon to oxygen (C:O) ratio. S GO shows the highest C:O ratio of 4.31, followed by T GO and M GO with ratios of 2.15 and 2.11, respectively. Thus, S GO is the most reduced material as evidenced by the lowest D:G ratio (less defects) and highest C:O ratio (less oxygen) and TGO and MGO seem to have similar extent of oxidation and defects in their surface. These differences in the materials' surface chemistry is attributed to their particular synthesis method, where the type of graphite, acid, and oxidizing agent employed alter the composition of oxygen functionalities present.[13] Upon Ag^+ impregnation, M GO had the highest Ag loading by mass after using either a high (13%) or low (2%) dose of $AgNO_3$ compared to the other two GO adsorbents. This high Ag loading of the M GO indicates that the Ag^+ attaches to the oxygen functional groups present on GO surface. As GO's surface oxygen content increased, more Ag^+ was impregnated to the material. This is further confirmed by the increased D:G values of the functionalized GO-Ag^+ composites for both high and low $AgNO_3$ doses. This increase is due to the adsorption of Ag^+ to the carbon scaffold, disturbing the electron distribution of the material, as previously observed in other studies.[29,215]

Table 5.2. Characterization of GO composites functionalized with silver ions. Three different types of GO (Tung (T), Marcano (M), and Staudenmaier (S)) were functionalized with either high (H) or low (L) silver ions using AgNO3 as the silver precursor.

Adsorbents	Raman Defects (D:G Ratio)	XPS (C:O Ratio)	Silver content (dry mass %)
T GO	0.98	2.15	0.00 ±0.00
H-T	1.04	-	9.41±1.55
L-T	1.01	-	1.76 ± 0.42
M GO	0.82	2.11	0.00 ±0.00
H-M	0.94	-	13.0 ±3.34
L-M	0.94	-	2.11 ±0.51
S GO	0.80	4.31	0.00 ±0.00
H-S		-	4.07 ±1.58
L-S		-	1.61 ±0.32

Figures 5.1. and 5.2. show the characterization of the GO after the *in situ* formation of Ag NPs of different sizes. The Tung GO was chosen for functionalization with Ag NPs due to its performance increased performance in removing Br^- after functionalization with Ag^+ compared to powdered activated carbon (PAC).[29] However, Kidd et al. utilized high silver doses (0.05M $AgNO_3$) to impregnate both T GO and PAC. In this study, AgNPs were synthesized using a low silver dose (0.01M $AgNO_3$) to decrease the amount of residual silver in water and prevent Ag release to a greater extent. The preparation of Ag NPs on the GO scaffold (GO-nAg altogether) was first confirmed by UV-Vis spectroscopy (Fig. 5.1.). The unfunctionalized GO exhibits a characteristic absorption peak at 230 nm that is related to the electronic π- π* transitions of C-C aromatic bonds and a shoulder at 305 nm assigned to the n- π* transitions of the C=O bonds.[215] After functionalization, the presence of a surface plasmon band at 400 nm is evident in the GO-nAg synthesized with the lowest concentration of $NaBH_4$, shifting to 430 nm upon the $NaBH_4$ concentration increase. The appearance of this band in the GO-nAg nanocomposites is indicative of the

Ag NPs deposition on GO sheets.[215,218] Microscopy was another technique used to further confirm the successful preparation of GO-nAg nanocomposites. The representative TEM micrographs in Fig. 5.2. (A-D) exhibit GO sheets functionalized with Ag NPs of different sizes on the carbon scaffold. Size distribution, as shown in panels E-H, was evaluated by averaging at least 100 particles gathered from multiple images of each nanocomposite. The GO-nAg had average sizes of 40 nm, 25 nm, 18 nm, and 9 nm which decreased as the concentration of the reducing agent increased.

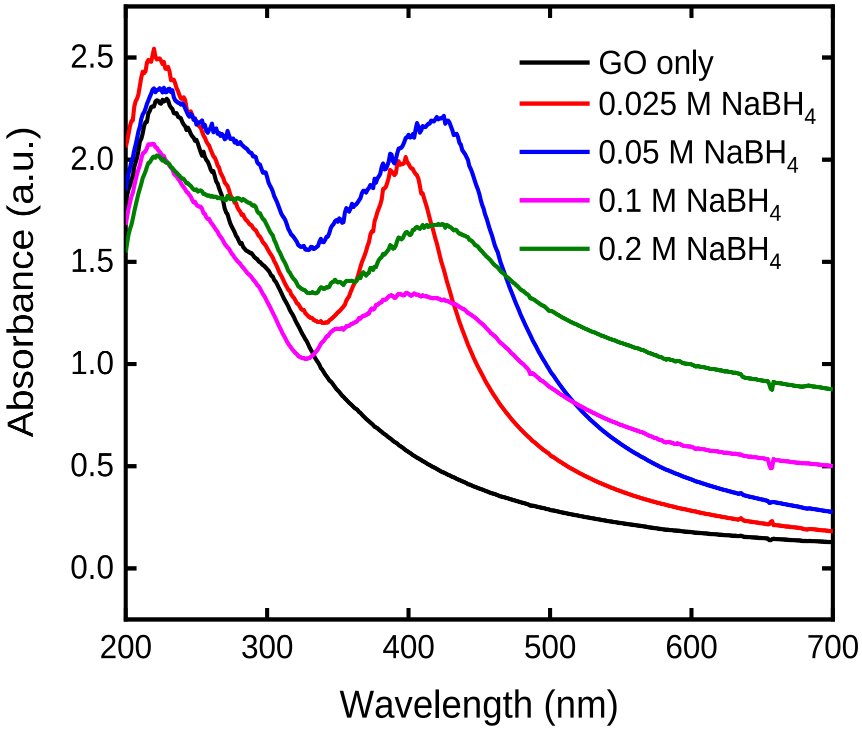

Figure 5.1. UV-Vis spectra of GO and GO-Ag nanocomposites after the addition of NaBH$_4$ at different concentrations (0.025-0.2M). The nanocomposite dispersions had a concentration of 50 ug/mL. Spectra shows evidence of the plasmonic band at 430 nm characteristic of Ag NPs formation.

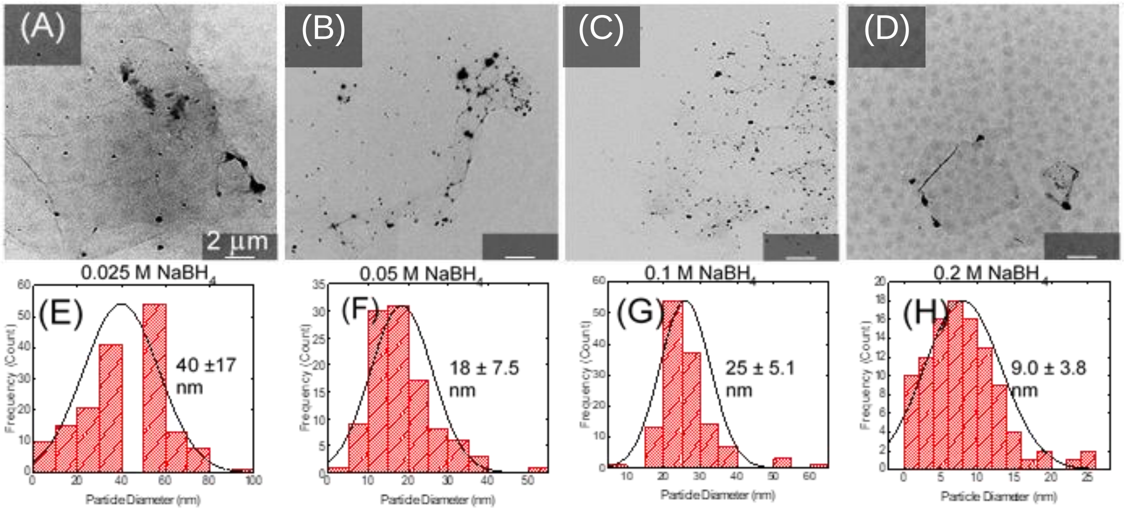

Figure 5.2. TEM micrographs of (A-D) GO-Ag sheets after the addition of 0.0.25, 0.5, 0.1 and 0.2M $NaBH_4$, respectively. Bottom panels (E-H) show size distribution of Ag NPs formed on GO sheets. More than 100 nanoparticle diameters were randomly selected from TEM images and analyzed using ImageJ software Data is shown as average ± standard deviation.

5.3.2. Effects of silver impregnation on Br^- removal in deionized water. The removal capacity of Br^- using Ag is shown in Fig. 5.3. In all scenarios, the initial spiked Br^- concentration was 200 µg/L, which is a realistic environmental concentration found in surface waters.[219,220] In ideal conditions, 1 mole of Ag^+ reacts with 1 mole of Br^- and forms 1 mole of AgBr. Thus, the stoichiometric value of 1 mol Br^-/mol Ag^+ is required to remove all the Br^- from the water.

Results show that Ag^+ (as $AgNO_3$) resulted in a 0.92 ± 0.05 mol Br^- removal/mol Ag^+ dosed, which is very close to the stoichiometric value. Similar results have been observed in the literature, where a 0.89 mol Br-/mol Ag^+ was achieved under very similar conditions.[221] If a carbon adsorbent in combination with Ag^+ is used, results indicate that a higher silver content achieves higher removal capacity as shown with H-S, H-M, and H-

T (orange bars) with removal capacities of 0.41 ± 0.15, 0.40 ± 0.11, and 0.51 ± 0.18 compared to lower silver contents as those achieved by L-S, L-M, L-T (light green bars) with capacity values of 0.12 ± 0.05, 0.10 ± 0.04, and 0.31 ±0.09, respectively. Kidd et al. had similar results, where the maximum removal capacity of Ag^+ for Br^- is no higher than 0.13 mol Br^- per mol Ag^+.[29]

Interestingly, the different surface chemistries of the graphene-based adsorbents did not impact the removal capacity of the composites when loaded with a high silver dose. The C/O ratio of the GO adsorbents follow the trend TGO<MGO<SGO, where TGO is the most oxidized material and SGO is the most reduced. Thus, one would expect that the most oxidized material would have more electrostatic interactions with the Ag^+ present in the water adsorbing them onto the carbon lattice and therefore, a higher removal capacity should be achieved. With lower silver doses loaded onto the GO adsorbents, a trend is more apparent, with L-S having the lowest removal capacity and L-T the highest. These differences indicate that the specific surface area and the extent of oxidation are parameters that plays a role when attaching Ag^+ to the carbon lattice as explained elsewhere.[29] Overall, H-T and L-T had the highest efficiency at removing spiked Br- from deionized water when compared to their individual groups (H-S, H-M and L-S, L-M). Because of this, the TGO was chosen as the GO support for functionalization with Ag NPs in further experiments.

High Ag^+ doses either applied independently or with a carbon support show higher Br^- removal capacities (>0.4 mol Br^-/mol Ag^+) compared to low Ag^+ doses, where L-T had the highest (0.3 mol Br^-/mol Ag^+). However, to reduce the risk of Ag^+ being present in the water, the TGO adsorbent was loaded with Ag NPs (GO-nAg) synthesized *in situ* using a low Ag^+ dose. Results indicate that T-40, T18, T-25, and T-9 had removal capacities of 0.72 ± 0.26, 0.60 ± 0.22, 0.42 ±0.15, and 0.47 ± 0.13, respectively (dark green bars). Overall, when compared to their ionic counterparts, GO-nAgs seem to perform better than the GO-Ag^+ using a low silver dose and slightly better than the GO-Ag^+ with a high silver dose. This trend is more evident with T-40, which had a higher capacity than H-T (0.72 vs. 0.51) and L-T (0.72 vs. 0.31). Most importantly, these results highlight that higher or similar Br^- removal capacities can be achieved using low silver doses with subsequent reduction to Ag NPs, than if a high Ag+ dose was applied. This is attributed to the fact that Ag NPs, due to their small size, have a higher surface area to volume ratio and therefore more sorption sites to where Br^- could adsorb to compared to ionic Ag. Interestingly, there was no difference on Br- removal efficiency between GO-nAgs as the size of the Ag NPs decreased.

Further testing was done with commercial Ag NPs of different sizes to evaluate whether the carbon lattice was required to remove Br^- from water or if Ag NPs alone could be used as the adsorbent. Findings reveal that Ag NPs of 20, 50, 100, 200, and 500 nm had removal capacities of 0.96 ± 0.43, 0.48 ± 0.16, 0.49 ± 0.21, 0.56 ± 0.13, and 0.26 ±0.10, respectively (gray bars). The contribution of adding Ag NPs to remove Br- is clear as the 20 nm particles achieved the highest capacity from all the materials tested. However, as the particle size increases, the removal capacity decreases, this trend being more evident with the 500 nm Ag NPs. These differences are attributed to the fact that Ag NPs, unlike Ag^+ who are dissolved in water, remain suspended in solution, and tend to form large aggregates as the particle size increases. Thus, the availability of Ag^+ to interact with Br^-

is reduced. Nonetheless, it is important to note that the T-40 performs equally well as the optimal unsupported 20 nm Ag NPs, suggesting that the carbon support can enhance the bromide removal of silver-impregnated composites in the absence of competing elements.

Figure 5.3. Removal capacity of spiked Br- (200 ug/L) in deionized water by GO-Ag composites, Ag^+ or Ag NPs. The blue bar represents the Ag^+ removal capacity; orange bars

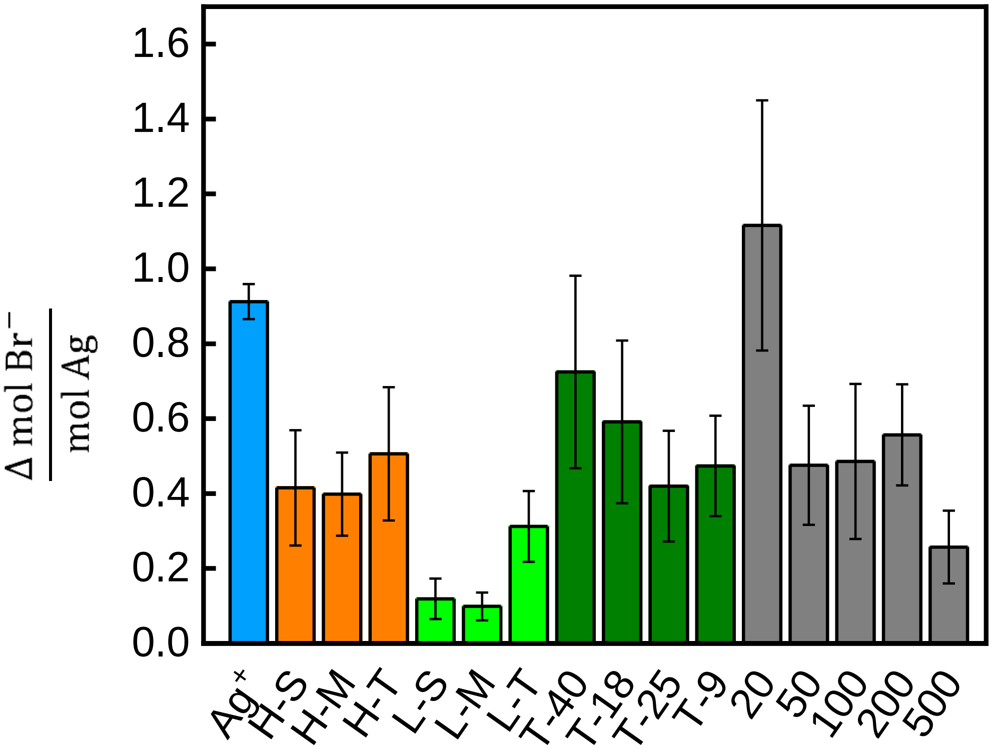

represent the $GO\text{-}Ag^+$ prepared with a high silver dose (H); light green bars represent the $GO\text{-}Ag^+$ prepared with a low silver dose (L); dark green bars represent GO-nAg of different sizes, where Ag NPs where synthesized using a low silver dose; and grey bars represent commercial Ag NPs of different sizes without any carbon adsorbent. Adsorbent dose was 25 mg/L and was applied as a powder directly. Data is shown as average ± standard deviation of triplicate experiments with three replicates each (n=9).

5.3.3. Effects of silver impregnation on Br^- removal in fresh waters. Selected materials were tested to assess the effect of competing ions in bromide removal efficiency. GO functionalized with Ag^+ were not tested since initial findings indicate that GO-nAg and Ag

NPs are more efficient at removing Br^- from water in a simple matrix. The T-40 was selected as a representative of the GO-nAgs as it showed the highest removal capacity amongst the GO-nAgs and Ag^+ was used to test the efficiency of pure Ag^+ compared to Ag in NP form (Fig. 5.4).

The Br^- removal capacity per mol of Ag^+ was highly impacted in a synthetic fresh water for all materials. This impact was particularly evident for Ag^+, which had the highest removal capacity in DI water but the lowest in fresh waters (from 0.92 to 0.10). For the T-40 the capacity was 0.63 ± 0.15 and for the Ag NPs 0.68 ± 0.20, 0.48 ± 0.14, 0.30 ± 0.13, 0.27 ± 0.11, and 0.36 ± 0.10 for 20, 50, 100, 200, and 500 nm, respectively. This decrease in capacity is attributed to the presence of competing ions in the fresh water matrix complexing with the Ag^+ that are being generated from the Ag NPs. Some of these include chloride, phosphate, and sulfate, all of which have very strong interactions with Ag^+. This has been observed in previous studies, where the Br^- removal capacity of silver-impregnated carbon adsorbents like GAC or PAC and even GO are significantly impacted by the background water characteristics.[29,221,222] Gan et al.[221] observed that chloride is the biggest competitor with Br^- due to the low solubility of AgCl and the typically much higher concentrations of chloride compared to bromide in natural waters (71 mg/L versus 200 µg/L under our conditions, see Table D.1.). It is noteworthy to emphasize that even though the removal capacity for T-40 in fresh water decreased compared to DI water, this GO-nAg still had one of the highest removal capacities in complex water, comparable to the effects observed with 20 nm Ag NPs (highest capacity), supporting the previous findings where

NPs (either in a composite or alone) are better candidates to remove Br- from water compared to Ag^+.

Another important consideration is the fact that Ag NPs dissolve to Ag^+ in aerobic environments and therefore the effects imparted by the Ag NPs as particles is difficult to assess. To evaluate the effect of NP dissolution on removal capacity, experiments using the same experimental conditions but in an anoxic environment were performed. As observed with the dashed bars in Fig. 5.4, the absence of molecular oxygen (O_2) is key to achieve a higher removal (capacities were all >0.60). The T-40 and 20 nm Ag NPs had the highest capacity amongst all the materials (>0.76 mol Br^-/mol Ag^+). Visual Minteq modeling also shows that in fresh waters with this particular composition, 100% of the Br^- should be dissolved in the water matrix and 0% of it should be precipitated, while the opposite trend is shown for Ag^+ as shown in table D.2. This introduces an interesting question: if the Ag NPs are not dissolving into Ag^+, why do we have Br^- removed from the fresh water? The answer relies on the fact that halide ions, namely Br^-, chloride, and iodide have shown to have etching capabilities on metallic NPs, including Ag NPs.[223] This property has been mostly studied during Ag NPs synthesis, particularly when trying to control the size and shape of the Ag NPs. A study by Tang et al. observed that upon the addition of halide ions to a Ag nanoprism suspension, the halide ions etch the nanoprisms subsequently converting them to nanodisks, thus indicating a direct interaction between the halide ion (i.e., Br^-) and the NPs.[224] Additionally, the ion etching reactions in both aerobic and anoxic environments have been studied. Results show that the etching abilities on Ag NPs are in the order of chloride < iodide < bromide, where Br^-, is shown to have the highest etching ability and is not oxygen dependent[224] whereas chloride is.[225,226] Other inorganic anions (phosphate, sulfate) do not show any etching abilities.

These observations help explain why the Br^- removal capacity increases upon the addition of Ag NPs in either aerobic or anoxic environments. Even in the presence of competing ions, the etching abilities of Br-, which are stronger than the main competing ion (chloride), will promote the formation of Br^--Ag NPs complexes. The proposed mechanisms for Br^- removal using Ag NPs or GO-nAg are then: 1) Br^- ions present in solution interact with Ag^+ that have been generated from Ag NPs dissolution and forms AgBr precipitates; 2) Br^- ions directly etch the Ag NPs' surface, promoting the Ag^+ etched from the Ag NP to complex with Br- and form AgBr precipitates, or 3) a synergistic mechanism where a combination of both dissolved Ag^+ and halide etching happening directly on the NPs' surface promotes AgBr formation. Even though this etching ability is not new, particularly in the Ag NP synthesis aspect (it has been used to control the shape of Ag NPs for years), it is the first time this halide property is being proposed as a key component in the mechanistical understanding of Br^- removal from water.

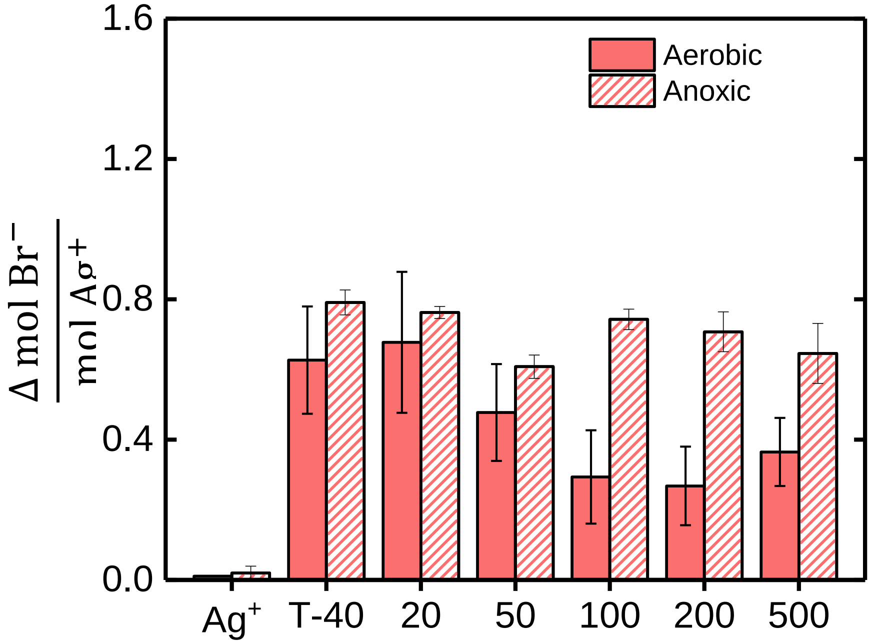

Figure 5.4. Removal capacity of spiked Br- (200 ug/L) in fresh waters by GO-nAg, Ag^+ or Ag NPs. Solid bars represent removal capacity in aerobic conditions and dashed bars represent the removal capacity in anoxic conditions. Adsorbent dose was 25 mg/L and was applied as a powder directly. Data is shown as average ± standard deviation of triplicate experiments with three replicates each (n=3).

5.3.4 Residual silver after jar testing. Another factor that will have an important effect on the applicability of these materials is the potential release of silver leaving in the water either as Ag^+ or Ag NPs. Concerns on the public health and environmental impacts of silver and nanomaterials have been identified as an important limiting factor for nano-enabled technologies in water treatment.[227] Therefore, it is important to design a process that can be used without generating additional contaminants in drinking water. To assess the amount of residual silver after Br^- removal, the solutions were filtered to remove the particulate material (which comprises a combination of Ag^+, AgNPs, GO, and AgBr particles). The amount of silver remaining in solution, which is either ionic or as very fine particulate silver, was then quantified via ICP-MS. The different silver-impregnated materials were found to leave different levels of silver in the filtered water (Figure D.1.1)

The GO materials impregnated with the highest Ag^+ dose left the highest concentrations of silver residuals (all >50,00 µg/mL of Ag), followed by GO materials with a low Ag^+ dose(including GO-nAgs) where residuals were above 10,000 µg/mL of Ag. The AgNPs left the smallest residual concentrations, particularly for the largest Ag NPs tested (500 nm) with less than 100 µg/mL of Ag . However, all materials, except the 500 nm AgNPs, left Ag^+ concentration that was higher than the secondary maximum contaminant level (SMCL) set for Ag by the EPA of 100 µg/L. Therefore, simply removing the particulate material is not enough to prevent silver leaching into drinking water. To address this concern and attempt to comply with the SMCL, a set of jar test experiments were done to simulate a traditional coagulation-flocculation-sedimentation process that would occur in a water treatment plant.

Fortunately, when the coagulant is added to the process, the residual Ag^+ concentrations for all materials are well below the regulated Ag SMCL (Figure 5.5.), with Ag^+ having the highest residual of 16.8 ± 0.01 µg/L Ag even after coagulation. The Ag NPs follow, with residual concentrations of 6.85 ± 0.02, 3.60 ± 0.44, and 1.11 ± 0.20 µg/L Ag for 50, 500, and 20 nm respectively. Last, the T-40 or GO-nAg has the least Ag residual with only 0.35 ± 0.12 µg/L Ag remaining after coagulation. These results obtained with Ag^+, arguably the hardest form of Ag to remove from water, suggest that the silver precipitates formed during Br^- removal are coagulated by alum and sediment during physicochemical treatment. Even though Ag NPs added alone show promising results with their capacity of removing Br- from water, it is the GO-Ag NPs composite, T-40, that is removed best. T-40 has demonstrated throughout to have a high Br-removal capacity in both DI and fresh water and is highly comparable to the efficiency seen with the 20 nm AgNPs. Another additional benefit of using the nanocomposite, as opposed to the Ag NPs alone, is demonstrated herein, where the carbon support, namely GO, improves the Ag residual concentration compared to the 20 nm Ag NPs. This enhancement is due to the micron-sized carbon sheet which facilitates the formation and sedimentation of flocs. Therefore, the coupling of Ag-impregnated matrixes and conventional coagulation processes is a promising approach to achieve high silver efficiency while avoiding the potential health and environmental implications of this nanocomposite.

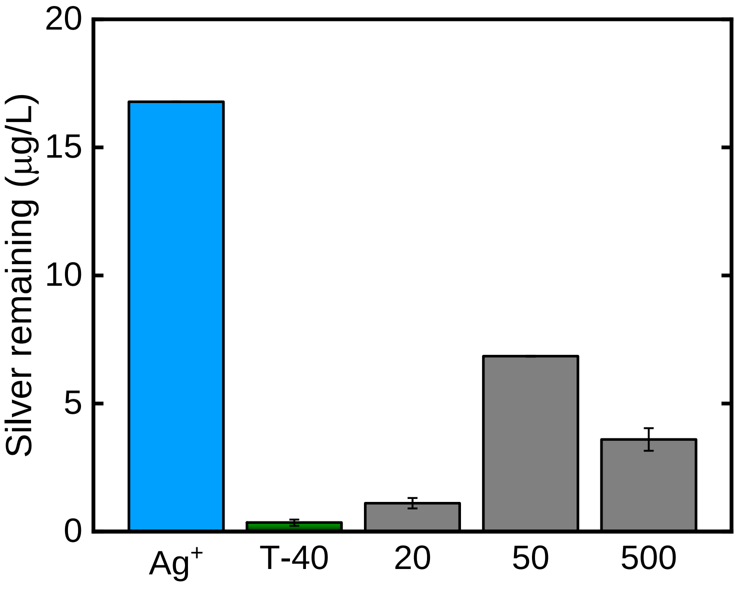

Figure 5.5. Residual silver concentrations (in µg/L) in fresh water after alum addition to simulate coagulation-flocculation-sedimentation. The alum dose was 28 mg/L. Data shown is the average ± standard deviation (n=3).

5.4. Conclusions

A new GO-nAg nanocomposite was synthesized to remove Br^- from fresh waters, consequently reducing the formation of toxic DBPs, and the amount of silver leaching into the environment. The functionalization of Ag NPs not only makes the nanocomposite more Ag efficient but also displays the highest Br- removal capacity when compared to their ionic counterpart in both DI and fresh waters but also in anoxic conditions. A new set of removal mechanisms has been proposed to remove bromide from water using Ag NPs namely: 1) Br^- ions present in solution interact with Ag^+ that have been generated from Ag NPs dissolution and forms AgBr precipitates; 2) Br^- ions directly etch the Ag NPs' surface, promoting the Ag^+ etched from the Ag NP to complex with Br- and form AgBr precipitates, or 3) a synergistic mechanism where a combination of both dissolved Ag^+ and halide etching happening directly on the NPs' surface promotes AgBr formation. This is the first study reporting such mechanism for Br- removal. Lastly, findings also support that a GO-nAg nancomposite is more effective at reducing Ag^+ leaching compared to Ag NPs due to the size of the carbon support, which is easily removed during coagulation-flocculation-sedimentation, subsequently making this nanocomposite safer by reducing the risk of silver exposure.

Supporting information

Table D.1. Fresh water composition; Table D.2. Visual Minteq calculations for fresh water constituents at pH 7.5; Figure D.1. Silver concentrations before and after Br- removal experiments for the different types of materials.

Acknowledgements

This work was supported the National Science Foundation, through the Nanosystems Engineering Research Center for Nanotechnology-Enabled Water Treatment (EEC-1449500). A.B. acknowledges the support of a Dean’s Fellowship from the Ira A. Fulton Schools of Engineering, a Scholar Award given by the International Chapter of the P.E.O. Sisterhood, and the Achievement Rewards for Collegiate Scientists Foundation.

CHAPTER 6

PROLONGING THE ANTIMICROBIAL ACTIVITY OF NANOSILVER-COATED MEMBRANES THROUGH PARTIAL SULFIDATION

Graphical Abstract

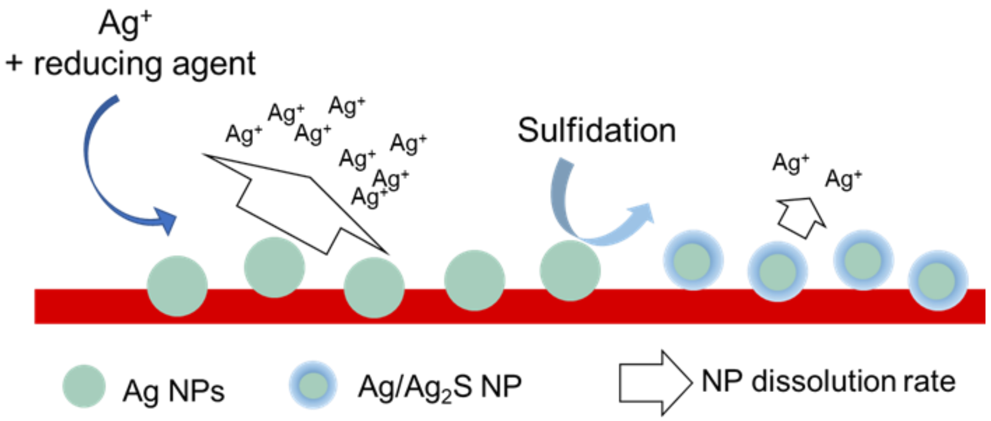

Novelty statement: Silver sulfidation in nanosilver-coated membranes slows down silver release and increase biofouling resistance without affecting the membrane's functionality.

Abstract

Biofouling is a major issue in membrane-based water treatment because it shortens membrane life and decreases the permeate flux. Silver, a known biocide, is often used for *in situ* formation of silver nanoparticles (Ag NPs) on membranes for biofouling mitigation. However, Ag NPs dissolve quickly in water, limiting their effectiveness over long periods of time. This study focuses on the modification of silver-functionalized reverse osmosis (RO) membranes with different concentrations of Na_2S (10^{-1}, 10^{-3}, and 10^{-5} M) to identify the degree of sulfidation that limits Ag release while preserving the antibacterial effect. Sulfidized membranes decreased Ag release by > 85% depending on the extent of sulfidation. Antibacterial activity was assessed using *P. aeruginosa* and *E. coli*. Results showed the highest inactivation at 73% for *P. aeruginosa* and 57% for *E. coli* for 10^{-5} and 10^{-3} M Na_2S-treated membranes, respectively, while the more sulfidized membrane treated with 10^{-1}M Na_2S treatment had the lowest antibacterial effect. Moreover, when tested in a dynamic cross-flow RO system for 24h, the flux declined by 24% for the Ag NPs and by 23%, 17%, and 19% as the extent of sulfidation increased. Additionally, the Ag remaining in the membrane was higher for the highest sulfidized membrane with 519 ng/cm^2. Therefore, retention of the silver coating over time appears to be more important for biofilm control in RO systems than high antibacterial activity. Both 10^{-5} M and 10^{-3} M Na_2S-treated membranes had the best balance between reduced dissolution rate and good antibacterial and anti-biofouling performance, respectively.

Environmental significance:

While the antibacterial activity of silver nanoparticles is widely attributed to the release of silver ions, their rapid release prevents the efficient application of Ag NPs on surfaces. One of such applications is in water treatment, where Ag NPs have been successfully functionalized onto membrane modules for biofilm reduction; however, their short-lived attachment limits the NPs usability. Here, we examine a functionalization technique that significantly slows down silver ion release through sulfidation of Ag NPs on reverse osmosis membranes. Sulfidation prolongs the antibacterial activity of the membrane while maintaining its integrity and functionality. This strategic design suggests that sulfidation is a promising technique to optimize silver usage and reduce its release in the environment.

6.1. Introduction

Each year, 2.7 billion people face severe water scarcity for at least one month per year. This dearth of freshwater arises from the rising demand driven by a growing global population and expanding international economies, as well as decreases in supply due to over-exploitation of resources and climate change.[228] To bridge the gap between freshwater supply and demand, many utilities are investing in desalination to tap into alternative water sources such as seawater, brackish groundwater, and wastewater.[229,230] Reverse osmosis (RO) is the state-of-the-art technology for desalinating water. RO is a membrane-based process that is more energy-efficient than other thermal desalination systems.[231] However, desalination by RO is still limited by considerable economic and environmental costs, both of which must be mitigated to ensure the sustainability of this increasingly vital water treatment process.

Biofouling, or the attachment and proliferation of microorganisms on a surface, reduces the efficiency of RO and contributes to the high economic and environmental costs of operating RO systems. The formation of biofilms, a heterogeneous assembly of microbial cells and extrapolymeric substances (EPS), on membranes increases the hydraulic resistance in the membrane module, resulting in higher energy requirements to maintain a constant transmembrane pressure differential.[232,233] Moreover, biofilm-enhanced osmotic pressure at the membrane interface can negatively impact the quality of the permeate.[234] To mitigate the effects of biofouling, operators must conduct extensive chemical cleaning procedures, which add to the operational expenses, damage membranes, and cause downtime in water production.[235,236] Altogether, the direct and indirect impacts of fouling, from increased energy usage to chemical and operational expenses associated with feed water pre-treatment and membrane cleaning, leads to significant economic impacts, with previous work estimating from 25 to up to 50% of the plant's total operating costs.[235,237]

For over a decade, research efforts have been made to design membranes resistant to biofouling.[238,239] One strategy involves imparting biocidal properties to membrane surfaces in an effort to reduce deposition, attachment, and adhesion of bacteria or inhibit their proliferation.[240,241] Membranes functionalized with biocidal materials such as graphene oxide, copper, selenium, or antibacterial polymer brushes have been shown to outperform control membranes in terms of flux decline and biofilm formation.[242–245] The most commonly used antibacterial compound for biofouling control is silver [9,246–252]. In its ionic form, silver is a strong antibacterial compound that inactivates cells through several pathways, including cell lysis and DNA damage.[253] Although a particle-mediated effect is generally acknowledged[37,254], the current paradigm for the antibacterial action of Ag NPs is that it is primarily driven by its capacity to release free silver ions, which is mediated by the presence of oxygen in the water.[255,256] Previous studies have shown that Ag NPs made insoluble through surface coatings on Ag NP surfaces have considerably reduced antibacterial properties.[256–258] Therefore, the focus of silver-based coatings for biofouling control has been on the more soluble zerovalent form of silver, either as Ag NPs or Ag NPs composites.[9,246–248,250,259,260]

However, the high solubility of zerovalent Ag NPs under aerobic conditions poses challenges for its implementation in water treatment systems. The fast release of silver ions from nanoparticles' coatings leads to a rapid loss of antibacterial performance over time in silver-coated membranes.[9,261] A Goldilocks conundrum thus arises, as silver must be released into its ionic form at a rate fast enough to drive concentrations to biocidal levels, but not so rapidly that the silver coating is depleted early in the membrane's life-cycle. Recent studies have proposed different approaches to prolong the antibacterial life of the silver coating on membranes. Higher silver loadings have been applied to membranes using layer-by-layer coating methods.[9] Slower release rates have been achieved using silver composites such as silver-loaded zeolites,[252] through mussel-inspired polydopamine chemistry,[260–262] or by embedding the particles into the polyamide layer of the membrane.[263] However, these chemistries can be complex or expensive, which may limit the applicability for commercial implementation.

In this report, we describe a simple and inexpensive surface modification procedure to generate a slow-release silver-based biocidal coating on RO membranes. Membranes coated with Ag NPs were partially sulfidized to Ag_2S to slow down the release of silver. Static and dynamic biofouling assays reveal that although a balance exists between antibacterial activity and silver solubility, slower release rate and higher silver longevity on the membrane are more important for dynamic conditions in membrane systems. These results provide important guidelines for the design of more cost-efficient silver-based antibacterial coatings.

6.2. Materials and Methods

6.2.1. Materials.

All chemicals and supplies were obtained from Sigma-Aldrich (Saint Louis, MO), except as noted below, and were of ACS grade or higher. Sodium borohydride powder was obtained from Acros Organics (New Jersey). A Dow FILMTEC™ BW30 membrane (Midland, MI) was used for all experiments. The bench scale RO module was constructed using Swagelok (Salon, OH) materials. Unless specified, all the solutions were prepared in deionized (DI) water from a GenPure UV xCAD plus ultrapure water purification system (Thermo Scientific, Waltham, MA).

6.2.2. Membrane modification.

6.2.2.1. *In situ* formation of Ag NPs.

Membrane modification was done following a protocol adapted from Ben-Sasson et al.[248] First, dried polysulfone RO membranes were wetted through immersion in 20% isopropanol and 80% DI water for 20 min. Then, the membranes were rinsed and soaked three times in DI water. These unfunctionalized, washed membranes were used as controls. The *in situ* formation of Ag NPs on the RO membranes was carried out as described below. The active layer of the membrane was placed in between a glass plate and a plastic frame (hole size 7.5 cm x 12 cm) to hold the solutions used for the modification. First, 50 mL of a 3 mM $AgNO_3$ solution was added to the active layer of the membrane for 10 min and agitated. Then, the $AgNO_3$ solution was discarded, leaving the active layer with a thin film of adsorbed solution wetting the surface. Next, 50 mL of a 3 mM $NaBH_4$ solution was added for 5 min to form silver nanoparticles on the membrane surface. The solution was then discarded. Finally, the membrane was rinsed with 10 mL of DI water for 10 s to remove excess reagents. All *in situ* reactions were done at room temperature.

6.2.2.2. Sulfidation of Ag NPs.

The previously prepared Ag NP membrane was sulfidized following the protocol by Levard et al.[257] Following the procedures described in 2.2.1, the membranes were kept in the frames and Ag NPs were sulfidized by adding 50 mL of either a 10^{-5}, 10^{-3}, or a 10^{-1} M sodium sulfide (Na_2S) solution, prepared in a 0.01 M $NaNO_3$ electrolyte, to the membrane surface. The membranes were agitated with the reagents for 24h at room temperature, rinsed with DI water and stored in a closed container until used. The solutions were prepared fresh for each experiment.

6.2.3. Membrane characterization.

Contact angles (CA) were taken on an Attension Theta by Biolin Scientific (Gothenburg, Sweden) using a 1001 TPLT Hamilton syringe (Reno, NV). To account for variability, at least 5 different CA measurements, from different areas of the membrane, were taken per sample. For each measurement, the software recorded ~200 data points over 10s. The CA values were averaged and reported as a final mean and displayed as average ± standard deviation. X-ray photoelectron spectroscopy (XPS) was done on a VG 220i-XL (Thermo Fisher Scientific Ltd. Hampton, NH) equipped with a monochromated Al K-alpha X-ray source. The data was analyzed using the CasaXPS software (version 2.3.18). Membrane surface roughness was analyzed by atomic force microscopy (AFM). AFM was performed using tapping mode with a Bruker Multimode 8 AFM (Digital Instruments, Plainview, NY) equipped with an NCHV (Bruker, Camarillo, CA.

Surface zeta potential was evaluated for each experimental membrane utilizing streaming potential measurements with a ZetaCAD analyzer incorporating a flat surface cell (CAD Instruments, Les Essartes-le-Roi, France) with a 0.1 mm spacer to create a stable opening during testing. An electrolyte solution comprised of 5 mM KCl and 0.1 mM HCO_3 was used throughout the analysis and measurements were taken over a pH range from 4-10, with a pressure range from 30-70 psi, and step durations of 30 and 60 seconds to determine the zeta potential of each membrane.

Membrane morphology was evaluated using scanning electron microscopy (ESEM-FEG XL-30, Philips Hitachi SU-70, Hillsboro, OR) at an acceleration voltage of 10 kV. Transmission electron microscopy (TEM) was performed on unsulfidized and sulfidized (10^{-1}M Na_2S) membranes. High and low-resolution TEM images were obtained by a JEOL 2010F coupled with an Energy Dispersive X-ray (EDX) detector for species determination at an accelerating voltage of 200 kV equipped with a CCD camera. TEM samples were prepared using the focused ion beam (FIB) FEI Nova 200 Nanolab with a Ga^+ ion beam from the Eyring Materials Center at ASU. Briefly, the membranes were placed on a SEM stub and held in place with copper tape. Then, they were carbon-coated before putting them in the FIB. An initial protective layer of Pt was deposited with an electron beam, followed by another Pt layer deposited with the ion beam. All ion beam work was done at 30 kV except for the final cleaning, which was done at 5 kV.

The transport properties of the membrane were examined in a dead-end filtration system. Each membrane type was cut in circles with a 5 cm diameter. First, the membranes were rinsed with 20% isopropyl alcohol for 20 min then in Nanopure water (Barnstead™, Thermo Fisher Scientific) for 20 min before placing it in the dead-end cell. The system was completely closed, and the membranes were compacted at 300 psi for 1hr. An aliquot was collected every 15 min and weighed with a balance to determine the flux. After compaction, the system was opened and a 2000 mg/L NaCl solution was used to assess salt rejection. Salt concentration was measured using a COM-100 HM digital conductivity meter.

6.2.4. Quantification of silver leaching.

Bench-scale batch tests were done to quantify silver release from the functionalized RO membranes. Following the protocol by Bi et al.,[264] three circular membrane coupons (⌀ = 2.5 cm, A=4.9 cm^2), from different membranes and for each membrane type were placed in 40 mL of extraction solution (deionized water) in individual 50 mL Falcon tubes and agitated continuously using a benchtop orbital shaker (Branstead Lab-Line, 80 rpm). Silver release was done at different time points: 0, 30, 60, 180, and 360 min. For each time point, the agitation was stopped, and the membranes were removed from the extraction solution. The leachates were then analyzed for silver content using Inductively Coupled Plasma-Mass Spectroscopy (ICP-MS, Thermo Scientific X Series II). The membrane was then acid digested by 10% trace metal grade HNO_3 to quantify residual Ag. The batch tests were done in triplicates at each time point. The release rate was calculated using the silver content remaining on the membrane after acid digestion in each time point mentioned above; the slope of the line was used as the release rate.

6.2.5. Antibacterial properties of functionalized membranes.

Pseudomonas aeruginosa (*P. aeruginosa*, ATCC 15692) and *Escherichia coli* (*E. coli*, W3110, ATCC 27325) were obtained from the American Type Culture Collection. Cultures were maintained on Lysogeny Broth (LB) agar plates stored at 4^{o}C and manipulated using aseptic techniques to avoid contamination. For both *E. coli* and *P.*

aeruginosa, the purity of the culture was verified using the Brilliance™ and Cetrimide agar selective media, respectively. Antibacterial properties on the pristine and functionalized membranes were assessed using a colony forming unit (CFU) assay. Before the experiments, all glassware, solutions and materials required were autoclaved for proper sterilization. Proper personal protective equipment was worn, and all the experiments were done in a biosafety cabinet under sterile conditions. Circular membrane coupons of 2.5 cm in diameter were punched and placed in plastic holders leaving the active site exposed. For each culture, a colony was selected from a plate streak prepared with either fresh *E. coli* or *P. aeruginosa* stocks (kept at 4° C) grown overnight in 25 mL of Lysogeny Broth (LB) in an Isotemp incubator (Fischer Scientific) at 37°C and placed on a shaker at 140 rpm. The cultures were then diluted in fresh LB (1:25) and cultivated in the same conditions until the optical density (OD) reached 1.0 at 600 nm. Aliquots of bacterial cells were taken and washed 3 times by centrifugation and resuspended in 0.9% NaCl to remove any cell debris. A 3 mL aliquot of the bacterial suspension (10^7 CFU/mL in 0.9% NaCl) was contacted with the membrane's active layer for 3h at room temperature. The suspension was discarded, and the membranes were washed with 0.9% NaCl to remove non-adhered cells. The coupons were placed in 50 mL falcon tubes containing 10 mL of 0.9% NaCl and bath sonicated for 10 minutes to detach bacteria from the surface. For the plating assays, 100 µL of the sonicated solution were withdrawn and diluted with 900 µL of fresh autoclaved 0.9% NaCl in Eppendorf tubes. The solution was vortexed and a 50 µL aliquot was collected and plated in an LB agar plate and incubated overnight. The CFU counts were done the next day and results were normalized with respect to the control CFU value.

6.2.6. Bench-scale RO biofouling.

Dynamic biofouling experiments were executed utilizing a bench-scale cross flow RO system with a three-cell configuration and a 15 L volume of synthetic secondary wastewater effluent (ionic strength of 15.9 mM) as feed water.[265] The composition and concentration of the synthetic secondary wastewater is as follows: NaCl at 468 mg/L, $MgSO_4 \cdot 7H_2O$ at 37 mg/L, $NaHCO_3$ at 42 mg/L, $CaCl_2 \cdot 2H_2O$ at 29 mg/L, KH_2PO_4 at 35 mg/L, NH_4Cl at 21 mg/L, $Na_3C_6H_5O_7 \cdot 2H_2O$ at 176 mg/L, and glucose at 100 mg/L. The RO system was initially loaded with control (not functionalized) or silver-functionalized BW30 brackish membranes (Dow, Midland, MI), pre-wetted for 15 min in 50% isopropanol, with an active area of 38.64 cm^2 (8.4 cm × 4.6 cm). Cell one was used for the control, while cells two and three were used for the experimental membranes. Pressure, temperature, and cross flow were controlled at a constant 325 psi, 20 °C, and 37.8 cm/s, respectively. The permeate flux for each cell was measured continuously using Sensirion SLI-2000 flow meters (Staefa, Switzerland) and the collected flux data was compiled into rolling averages of 20 data points. For each experiment, the membranes were first compacted at 325 psi until the permeate flux reached a stable value (~4 h), after which the salts were added. *Pseudomonas aeruginosa* (*P. aeruginosa*, ATCC 15692) was used as a model biofilm-forming organism. It was grown overnight in LB broth on a shaker plate at 140 rpm in an Isotemp incubator (Fisher Scientific) at 37°C. The culture was then diluted in fresh LB on a 2:25 ratio and grown in the same conditions until the OD reached 1.0 at 600 nm. The cells were then washed by centrifugation 3 times with the synthetic secondary wastewater. The bacteria were then diluted in that same medium at a 1:10 ratio. After a brief re-stabilization (~45 min), bacteria were added at a concentration of 2.5×10^6 cells/mL (50 mL) to induce biofouling of the membranes. Biofouling experiments were conducted for 24 h. After each experiment, the membranes were collected, briefly rinsed in DI water, and then digested by 10% HNO_3 to determine the amount of silver remaining on the membrane using ICP-MS.

6.2.7. Data analysis and statistics.

All treatments were prepared in at least three independent replicates. To account for the inherent variability of both membrane surface chemistry and bacterial experiments,[266–270] antimicrobial assays were performed in triplicates and repeated in three independent experiments at a minimum (i.e. n=9). Means and standard deviations were estimated for each treatment and results were normalized with respect to the control. Data was assessed for normality using the Shapiro-Wilk test and all skewness and kurtosis z-values were well within the normal range of -1.96 to +1.96. Statistical differences between control samples (no Ag NPs) and silver-functionalized membranes, were determined via a one-way analysis of variance (ANOVA), followed by a Tukey post-hoc test where a p value less than 0.05 was considered significant. Statistical analysis was done using the Statistical Package for Social Sciences software (SPSS) version 26.

6.3.Results and Discussion

6.3.1. Sulfidized membranes characterization.

The successful functionalization of the pristine membrane was confirmed by both SEM microscopy and XPS. The functionalization process was done in two stages: 1) *in situ* formation of Ag NPs on the RO membrane and 2) sulfidation of Ag NPs. The first stage only requires two reagents, silver nitrate and a reducing agent; the second stage requires a sulfidizing agent, in this case, sodium sulfide. In stage 1, $AgNO_3$ is added and eventually removed, leaving a thin film of solution covering the active layer of the membrane. The reducing agent is added to reduce the free Ag ions in the residual thin film, precipitating Ag NPs in the membrane surface. In stage 2, different concentrations of Na_2S were added so that the Ag NPs react with the inorganic sulfide in solution to from $Ag:Ag_2S$ particles.[257]

Figure 6.1 displays SEM micrographs of the control membrane, the Ag NP functionalized membrane (stage 1 only) and the sulfidized membrane (stages 1 and 2). Based on these images (Figure 6.1A-C), all the surfaces show a “ridge and valley” structure characteristic of the polyamide layer.[250,271] Although the SEM micrographs show no significant visual difference between the control (A), Ag NP-modified (B), and sulfidized membranes (C), there is an evident color change from white to a dark yellow-brown color once the Ag NPs formed on the membrane’s surface.[250] Subsequently, the color changed from yellow-brown to a dark brown after addition of the highest concentration of Na_2S.[272] The transformations from Ag NPs to $Ag:Ag_2S$ NPs were further confirmed by TEM (Figure 6.1 panels D-G). These results indicate d-spacing values of 0.257 and 0.269 nm for Ag and Ag_2S, confirming the formation of Ag_2S at the surface of the Ag NPs as supported by other studies.[273–276] EDAX spectroscopy confirms the presence of Ag (2.98 keV) and sulfur (2.31 keV) for the sulfidized membrane.

XPS measurements were done to analyze the elemental composition of the functionalized membranes (Table 6.1). As expected, silver was not detected on the control membranes. The functionalized membranes kept a constant Ag content with an average of 7.78% Ag regardless of the extent of sulfidation. Additionally, XPS shows an increase of sulfur as the concentration of Na_2S increases. The other elements detected by XPS were carbon, oxygen, and nitrogen (peaks at 281, 396, and 527 eV for C 1s, N 1s, and O 1s, respectively), which appear in all the spectra (control and *in situ* modified membranes), as these elements are constituents of the polyamide layer. According to the surface elemental analysis, the nitrogen/carbon ratio at the membrane surface was slightly reduced for the *in situ* modified membranes. This reduction, likely due to masking of the polyamide amine group by the Ag NPs, indicates a decrease in the nitrogen coverage and implies that nitrogen (from the precursor $AgNO_3$ solution) had no significant content in the formed Ag-NPs.[248] The carbon/oxygen ratio on the membrane surface exhibited an increase from 0.80 to 1.1 for the control membrane and sulfidized membrane (10^{-1}M Na_2S), respectively, indicating a decrease in oxygen content. The decrease in C/O ratio may be associated with the functionalization process, as oxygen functional groups are known to serve as anchor sites for nanoparticles during the heterogeneous nucleation process.[259,277,278] Therefore, it can be concluded that the *in situ* Ag NPs on the membrane comprised of metallic silver and Ag:Ag_2S NPs after sulfidation.

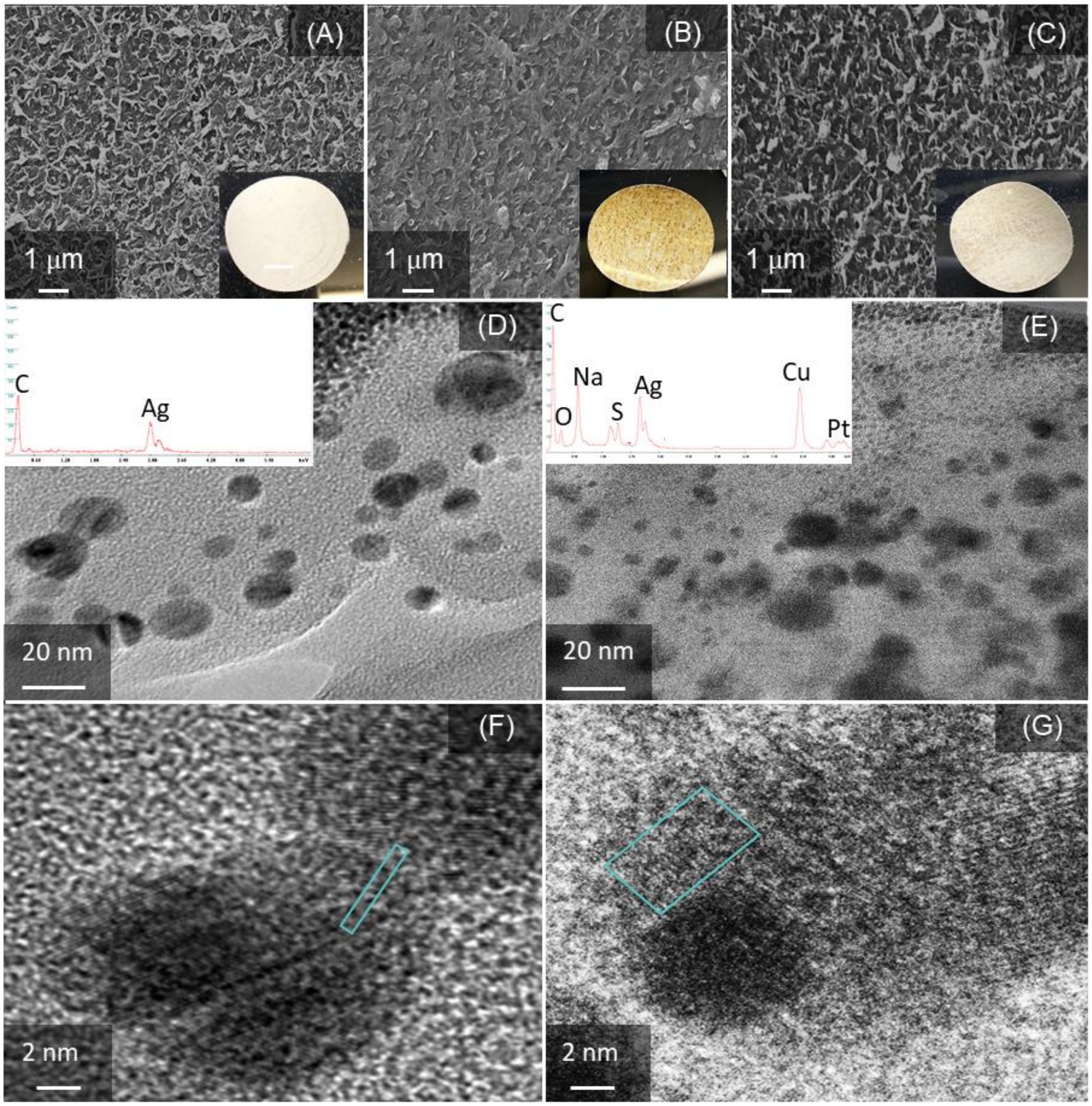

Figure 6.1. Sulfidized membranes characterization. Scanning electron microscopy imaging of A) control, B) Ag NPs functionalized, and C) sulfidized Ag NPs membranes. Inserts shows the visual change in the membrane surface. Solutions of 3 mM $AgNO_3$ and 3 mM $NaBH_4$ were used during the in situ formation reaction. Samples were sputter coated with gold and platinum and images were taken at 10 kV acceleration voltage. Low resolution TEM images of the polyamide active layer with D) Ag NPs and E) sulfidized Ag NPs. Inserts show EDAX spectra (in red) of each membrane. High resolution TEM images of F) Ag NPs and G) sulfidized Ag NPs. A concentration of 10^{-1} M Na_2S was used to sulfidize the Ag NPs. The teal colored box represents the area where the fringe analysis was done.

Table 6.1. Compiled XPS data representing atomic percent of the carbon, oxygen, nitrogen, silver, and sulfur content for the pristine and functionalized membranes.

	% C 1s	% O 1 s	% N 1s	% Ag 3d	% S 2p
Control	42.3 ± 3.7	52.7 ± 3.0	5.1 ± 0.7	n.d.	n.d.
Ag NP	42.0 ± 4.3	49.2 ± 0.7	1.27 ± 1.39	6.95 ± 4.0	0.09 ± 0.8
10^{-5} M Na_2S	40.7 ± 3.0	50.5 ± 1.4	<0.5	7.49 ± 1.6	0.83 ± 0.2
10^{-3} M Na_2S	46.4 ± 2.8	43.7 ± 0.9	<0.5	8.34 ± 1.8	1.09 ± 0.4
10^{-1} M Na_2S	46.5 ± 2.9	43.8 ± 0.8	<0.5	8.35 ± 1.8	1.21 ± 0.5

6.3.2. Functionalization alters the surface properties of control membranes.

Membrane surface properties such as roughness, permeability, or hydrophilicity will dictate the fouling propensity of the membrane.[229] As such, it is important to evaluate how functionalization may impact these surface properties compared to the control membrane. Results indicate that, except for the 10^{-3}M Na_2S treated membrane, modification significantly increased surface roughness compared to the control (Figure 6.2A). As determined by AFM, the control membrane had an average surface roughness of 22.9 nm ± 5.48, whereas the functionalized membranes had values of 49.0 nm ± 12.7 for Ag NPs, 53.6 nm ± 4.41 for 10^{-5} M Na_2S, 42.3 nm ± 17.6 for 10^{-3} M Na_2S, and 61.2 nm ± 16.6 for 10^{-1} M Na_2S. It is noteworthy that although there is no statistical difference between silver functionalized and sulfidized membranes, roughness tends to increase as the amount of Na_2S increases.

Surface wettability was assessed by measuring the water contact angle (CA). On one hand, functionalization with either Ag NPs or sulfidized Ag NPs did not impact the CA when compared to the control, which had a CA of 43.8° ± 12.8, similar to the findings of Ben-Sasson et al.[248] On the other, sulfidation of Ag NPs using all Na_2S concentrations (10^{-5} to 10^{-1}M) increased the hydrophilicity of the membranes compared to the Ag NPs, reducing the CA from 51.3° ± 3.56 to an average of 34.3° ± 7.98 for the sulfidized Ag NPs

(Figure 6.2B). Surface charge, measured as the surface streaming potential, show a slight increase to less negative values after functionalization. However, these changes were not significant (Figure 6.2C).

RO systems usually require membranes with high salt rejection and high water permeability.[279] It has been previously reported that silver functionalization on RO membranes can decrease water permeability but has minimal impact on salt selectivity.[248]In this study, none of these parameters were affected even after the sulfidation of silver at different concentrations (Figure S1). Previous studies show that hydrophilicity and surface roughness are major factors that impact the membrane's antifouling properties.[9,36,239,240,271,280] Typically, studies report that hydrophilic surfaces that have low surface roughness are less prone to fouling. This assumption is reasonable because if the membrane is more hydrophobic, hydrophobic organic molecules will interact more with the membrane's surface, which facilitates surface contamination.[239] Similarly, increasing roughness can have a negative impact on the antifouling properties because foulants, like proteins, are more likely to be adsorbed in the valleys of the membrane, and as such, there is a greater surface area to which foulants can be attached.[9,271] In this study, the sulfidized membranes are more hydrophilic but show an increase in surface roughness. The overall fouling propensity of a surface is difficult to predict, even after the individual assessment of the surface properties. Therefore, dynamic bacteria deposition assays were done to elucidate which membrane will have the highest fouling resistance.

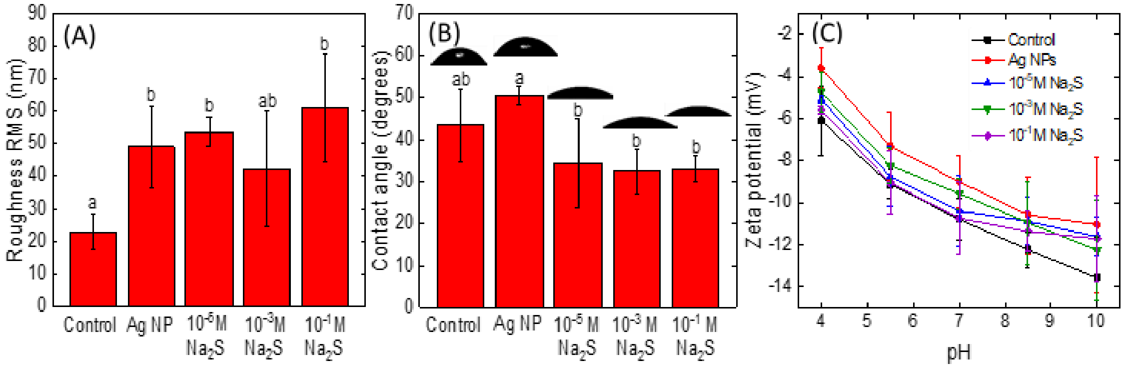

Figure 6.2. Membrane surface properties of control and functionalized membranes. (A) Surface roughness (root mean square) measured by AFM (B) CA measured by surface contact angles, and (C) zeta potential measured at acidic, neutral, and basic pHs. Different letters indicate statistical difference ($p < 0.05$).

6.3.3. Sulfidation slows down silver leaching.

An important question in this work concerns how sulfidation affects the Ag NPs behavior in natural systems. Ag NPs dissolve in aqueous solutions and release silver ions (Ag^+). Although this property is expected and desirable for biofouling control, the continuous dissolution of Ag NPs reduces the antifouling efficacy of the membrane during use and adds to the cost of membrane operation.[264] Furthermore, the release of silver into concentrated brines is an additional challenge to consider. In this study, silver sulfidation is proposed as a mean to extend the service life of Ag NP-enabled membranes and control silver release.

The release of Ag^+ is an important parameter to consider for risk assessment as it relates to the toxicity imparted by Ag NPs. Figure 3 shows the Ag^+ release rate of the functionalized membranes according to their sulfur to silver (S/Ag) ratio. The silver remaining on each membrane after each time interval (0-6h) is shown in Figure S2. The silver membrane (no sulfur) has a Ag^+ release rate of 157.5 ± 54.9 ng/ cm^2-hr whereas the sulfidized membranes have a release rate of 80.9 ± 57.1, 31.9 ± 37.7, and 20.6 ± 16.9 for the 10^{-5}M Na_2S, 10^{-3}M Na_2S, and 10^{-1}M Na_2S respectively. This trend suggests that the sulfidation of Ag NPs can decrease by > 85% the mass of silver released depending on the sulfidizing agent's concentration, as similarly observed in previous studies[273,281] The sulfidation of metals influence their toxicity in natural environments due to the low solubility of metal sulfide species; the decrease in silver release after sulfidation is consistent with the low solubility constant for Ag_2S ($K_{sp} = 10^{-50}$).[257,282]

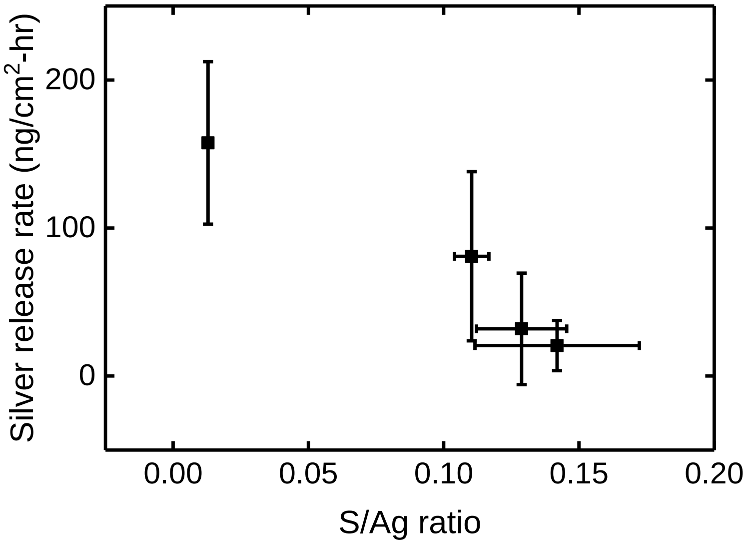

Figure 6.3. Effect of sulfidation (S/Ag ratio) on the silver release from the membrane. Silver release was calculated based on the silver remaining on the membrane over time, after acid digestion, by ICP-MS.

6.3.4. Sulfidation preserves the antibacterial activity.

The antibacterial properties of silver ions are attributed to three main mechanisms: i) Interaction with sulfhydryl groups on the cell surface, which may block respiration and electron transfer to lead to the de-energizing of the membrane and cell death; ii) A small ionic radius (0.115 nm) allowing Ag ions to travel through transmembrane proteins like porins (1-3 nm) and react with thiol functional groups in proteins and nucleic acids, which interfere with DNA replication or deactivate multiple enzymes; and iii) Increase ROS levels due to the deactivation of thiol-containing and antioxidative enzymes.[37,41] Ag NPs are efficient antibacterial agent because they exhibit enhanced silver ion release per unit mass due to an increased surface area to volume ratio.

Even though Ag NPs can offer strong antibacterial properties, their rapid dissolution in aqueous matrices limits their applications and promotes a faster release into the environment. Sulfidation of Ag NPs is a promising technique to maintain the efficiency of Ag NPs' toxicity while slowing down silver release. Viability of *P. aeruginosa* and *E. coli* was measured via CFU counts by exposing functionalized coupons to a bacteria solution for 3h. *E. coli* was used due to its widespread use as a model for the testing of antimicrobial surfaces. Figure 6.4 results show a significant CFU reduction for both bacteria. *P. aeruginosa*, a model biofilm bacterium, reduced cell viability to 39.5 ± 17.2, 26.9 ± 12.6, 44.0 ± 20.3, and 55.7 ± 23.7% for coupons functionalized with Ag NPs, 10^{-5}, 10^{-3}, and 10^{-1} M Na_2S. Similar results were observed with *E. coli*, where cell viability reduced to 50.0 ± 20.4% when exposed to coupons functionalized with Ag NPs and to 48.5 ± 19.1, 42.9 ± 15.1, and 75.4 ± 32.5%, for coupons coated with 10^{-5}, 10^{-3}, and 10^{-1} M Na_2S, respectively, compared to the control. The highest antibacterial activity for *P. aeruginosa* was achieved with the 10^{-5} M Na_2S coupon, where cell viability reduced by 73% whereas for *E. coli* viability was lowest at 57% after exposure to 10^{-3} M Na_2S. These results indicate that *P. aeruginosa* has a higher sensitivity to silver compared to *E. coli*, as observed in a similar study by Ben-Sasson et al.[248] In both bacterial assays, both Ag NP-coated and sulfidized membranes reduced cell viability in a statistically significant way except for the most sulfidized membrane (10^{-1} M Na_2S) which was not statistically different from the control. However, there is no statistical difference between the Ag NP-functionalized and sulfidized membranes. Based on these results and in agreeance with Levard et al.[273], we observe a threshold of Ag NP sulfidation where the antibacterial activity is reduced.

Similar results have been observed in the literature, where Ag NPs decrease cell viability in *P. aeruginosa*[36,245] and Ag NP sulfidation decreases toxicity towards *E. coli,*[272] nitrifying bacteria,[283] and *C. elegans.*[284] Reinsch et al.[272] observed that higher Ag_2S/Ag^0 ratio resulted in less growth inhibition of *E. coli* over 6h of exposure. Devi et al.[285] observed that Ag NPs enhanced oxidative stress whereas Ag NP sulfidation alleviated changes in oxidative stress, detoxification enzymes and brain acetylcholinesterase activity in adult zebrafish. All of these findings were attributed to the lower solubility of Ag_2S compared to Ag^0 NPs.

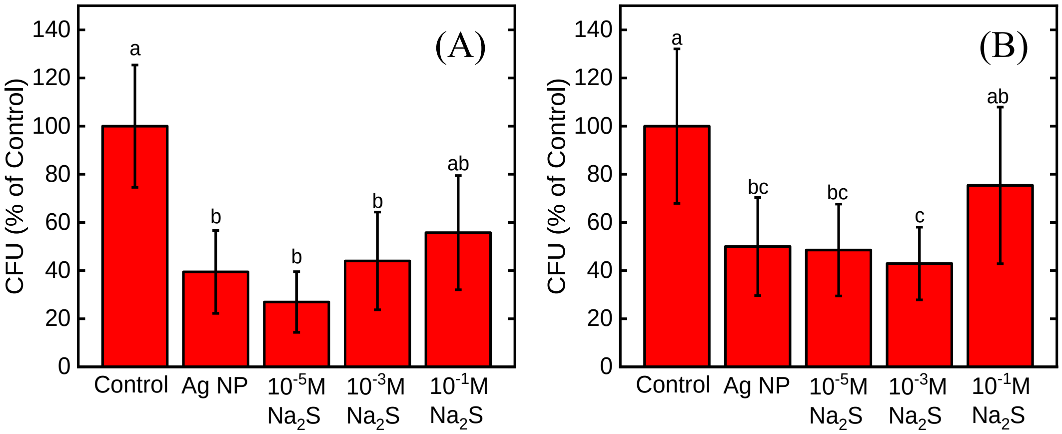

Figure 6.4. Number of viable colony forming units (CFU) on a 4.9 cm^2 coupon after 3h of contact with 10^7 CFU/mL of (A) *P. aeruginosa* and (B) *E. coli*. Results have been normalized with respect to the control. Different letters indicate statistical difference ($p < 0.05$), n=9.

6.3.5 Biofouling experiments and residual silver after biofouling.

To determine the biofouling mitigation potential of functionalized membranes, a set of experiments using a bench-scale RO fouling system were done using a synthetic secondary wastewater spiked with *P. aeruginosa*. This bacterium was chosen as a model organism for membrane biofouling studies due to its biofilm forming ability.[286] Additionally, this bacterium produces at least three extracellular polysaccharides, which are a constituent of EPS which in turn have been suggested to be the predominant culprit for biofouling of RO membranes.[234,235] Over a course of 24h, a gradual decline in the permeate flux was observed due to biofilm development for all samples (Figure 6.5A). The control membrane had a flux decline of 29% ± 0.8. When compared to the control membrane, the Ag NPs, and all sulfidized membranes (10^{-5} M, 10^{-3} M, and 10^{-1} M Na_2S) resulted in a significantly lower permeate flux decline with a 24% ± 0.7, 23% ± 1, 17% ± 2, and 19% ± 1 decline, respectively (Figure 6.5B). Silver functionalization and further sulfidation was able to reduce the effect of biofouling under dynamic biofouling conditions. Even though there is less silver being released from the sulfidized membranes, the toxicity of the Ag NPs and Ag ions led to a reduction of live bacteria on the membrane, consequently leading to an increased fouling resistance.[36,248] This can be attributed to the fact that very low doses of Ag are required to impart a biocidal effect. Additionally, the sulfidized membranes have more silver remaining which leads to more silver released over longer periods of time and thus, prevent bacterial attachment. This effect is better observed with the 10^{-1}M Na_2S membrane, where the slower release of Ag^+ is sufficient to impart biofouling resistance.

Residual silver was measured to assess the Ag^+ release potential after biofouling (Figure 6.5C). In agreement with the release rates discussed above, it is observed that the sulfidized membranes with the highest S/Ag ratio retain more silver than the Ag NPs. The 10^{-1} M Na_2S membrane had 519 ± 209 ng/cm^2 of Ag compared to 132 ± 209 ng/cm^2 from the Ag NPs membrane. These results show that sulfidation is a promising technique for membrane technologies: it slows down silver release, while retaining the Ag NPs biocidal properties. More importantly, these results highlight that silver retention on the surface is more important for biofouling resistance than biocidal properties measured under static conditions.

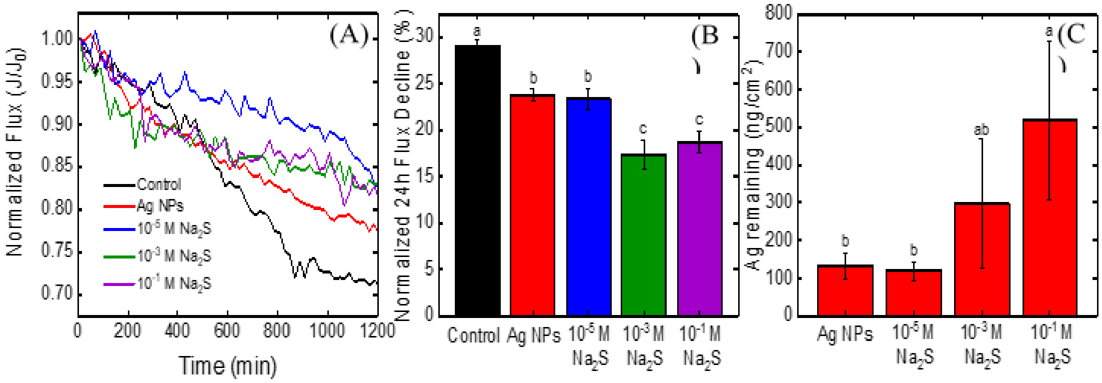

Figure 6.5. (A) Normalized average flux decline over 24h of RO modules tested with the control and each of the functionalized membranes. The initial *P. aeruginosa* concentration in the synthetic secondary wastewater medium was 2.5 × 10^6 cells/mL. (B) Normalized flux decline of each bench-scale RO run (n=3). The final permeate flux was calculated from the average of the flux for the last 20 min of the experiment. (C) Ag remaining after 24 h of RO modules tested with the control and each of the functionalized membranes. Ag was quantified using ICP-MS. Different letters indicate statistical difference ($p < 0.05$) n=9.

6.4. Conclusions

Biocidal coatings using silver have been shown to impart biofouling control on membranes. However, one of the main drawbacks of silver is its rapid ion release and eventual depletion from the membrane, which affect its performance and antibacterial activity. This study provides insights into how sulfidation of Ag NPs can overcome the aforementioned barriers. Different extents of sulfidation were studied to assess the antibacterial activity, silver release and biofouling resistance of the *in situ* Ag:Ag_2S particles. Sulfidation of Ag NPs can decrease silver release by > 85% without affecting the antibacterial activity, however, there is a threshold of sulfidation where the antibacterial activity can be lost. In addition, this study demonstrates that static biocidal performance does not predict biofouling resistance and that even for the sulfidized Ag:Ag_2S particles showing reduced antibacterial activity, high biofouling resistance is observed due to the higher retention of silver on the membrane surface. Overall, sulfidation is a simple and effective way to prolong the lifetime of anti-biofouling Ag NP coatings. Future research should focus at testing the membrane performance for longer periods of time and under real water conditions to evaluate the effect of the complex water matrix in natural waters.

Acknowledgements

This work was supported the National Science Foundation, through the Nanosystems Engineering Research Center for Nanotechnology-Enabled Water Treatment (EEC-1449500), and the NASA STTR program (contract no. 80NSSC19C0566). We acknowledge the contribution of Naiara Mottim Justino for her assistance in the membrane performance characterization. A.B. acknowledges the support of a Dean’s Fellowship from the Ira A. Fulton Schools of Engineering and a Scholar Award given by the International Chapter of the P.E.O. Sisterhood. We acknowledge the use of TEM facilities within the Eyring Materials Center at Arizona State University supported in part by NNCI-ECCS-1542160.

CHAPTER 7

CONCLUDING REMARKS

Given the promising applications of NMs in multiple fields, particularly environmental engineering, environmental and human health risks will be unavoidable. Scientists and engineers have been studying and utilizing the principles of green chemistry to design materials with the aim to minimize or eliminate their risk. This framework is not necessarily based by controlling exposure, but through the design and use of materials that are inherently nonhazardous. For NMs, there is a general knowledge gap regarding the intrinsic structures and physicochemical properties that link these properties with a desired functionality or cause an unintended harm. Not to mention that there is often uncertainty in the ability to predict and reduce potential risks for NMs throughout their life cycles. As such, it is important to evaluate the structure-property-function and structure-property-hazard relationships of NMs to better contribute to the development of a rational design framework. This way, materials with enhanced functionalities can be designed with minimal toxicity.

This dissertation covered three aspects that contribute to the safer design of NMs. The first aspect was related to the structure-property-hazards, where the toxicity of GB NMs with different surface chemistries was evaluated towards bacteria, cyanobacteria, algae, and invertebrates. Results emphasize a strong correlation between oxygen content and toxicity; however, this relationship is species-dependent. Bacteria and invertebrates were less susceptible to the highly oxidized GO whereas both photosynthetic organisms showed higher sensitivity, as demonstrated by the calculated EC_{50} concentrations (Ch. 1

and 2). These results highlight that the same material can have a different impact across species further studies are required to evaluate these relationships with other materials and other organisms.

The second aspect covered was related to understanding the structure-property-function of NMs to optimize a desired functionality. This was evaluated by employing GB NMs with different surface chemistries as either nanofillers in a polymeric composite to slow down photodegradation or as a support in a nanocomposite to remove a contaminant from water using Ag. Both projects emphasized that by understanding the materials' properties, their intended functionalities can be enhanced. In Ch. 4, it was demonstrated that graphene, RGO, and GO, have different effects after UV exposure and that oxidized GB NMs are more prone to photoreduction than graphene. Additionally, in humid UV conditions, oxidized GB NMs are more susceptible to being released due to moisture-induced degradation. Thus, graphene, being more photostable and a hydrophobic nature, is a better material to slow down photodegradation. Ch. 5 compared a GO support functionalized with Ag^+ or Ag NPs to remove Br^- from water eventually reducing the formation of DBPs. A highly oxidized GO functionalized with Ag NPs were the best candidates to remove the halogen. GO worked as a support for the AgNPs, providing stability, whereas the AgNPs had a higher surface area and more sorption sites. Not to mention, that this nanocomposite yielded less Ag remaining in water, reducing the exposure risk.

The last aspect covered was a combination of understanding both, the structure-function AND structure-hazard relationships of NMs. Sulfidation of Ag NPs was proven to be an efficient way to slow down Ag^+ release while at the same time reducing biofouling. Overall, the combination of these results support that the establishment of parametric relationships between ENM properties and their functional efficacy and hazard profile will enable the development of appropriate characterization factors used to evaluate environmental impact.

REFERENCES

1 D. R. Paul and L. M. Robeson, *Polymer (Guildf).*, 2008, **49**, 3187–3204.

2 Nano 101: What it is and how it works, https://www.nano.gov/nanotech-101/what.

3 T. H. E. Perspectives, C. Is, A. R. Series, D. To, E. Potentially and C. Viewpoints, 2015, **34**, 954–958.

4 H. Lu, J. Wang, M. Stoller, T. Wang, Y. Bao and H. Hao, .

5 F. Liu, J. Yang, J. Zuo, D. Ma, L. Gan, B. Xie, P. Wang and B. Yang, *JES*, 2014, **26**, 1751–1762.

6 W. Tang, G. Zeng, J. Gong, J. Liang, P. Xu, C. Zhang and B. Huang, *Sci. Total Environ.*, 2014, **468–469**, 1014–1027.

7 J. Yan, L. Han, W. Gao, S. Xue and M. Chen, *Bioresour. Technol.*, 2015, **175**, 269–274.

8 A. F. Faria, C. Liu, M. Xie, F. Perreault, L. D. Nghiem, J. Ma and M. Elimelech, *J. Memb. Sci.*, , DOI:10.1016/j.memsci.2016.10.040.

9 M. S. Rahaman, H. Thérien-Aubin, M. Ben-Sasson, C. K. Ober, M. Nielsen and M. Elimelech, *J. Mater. Chem. B*, 2014, **2**, 1724–1732.

10 O. Zaytseva and G. Neumann, *Chem. Biol. Technol. Agric.*, 2016, 1–26.

11 Y. Wang and L. M. Gilbertson, *Green Chem.*, 2017, **19**, 2826–2838.

12 F. Perreault, A. Fonseca De Faria and M. Elimelech, *Chem. Soc. Rev.*, 2015, **44**, 5861–5896.

13 H. L. Poh, F. Šaněk, A. Ambrosi, G. Zhao, Z. Sofer and M. Pumera, *Nanoscale*, 2012, **4**, 3515–3522.

14 X. Zou, L. Zhang, Z. Wang and Y. Luo, *J. Am. Chem. Soc.*, 2016, **138**, 2064–2077.

15 F. Perreault, A. F. de Faria, S. Nejati, M. Elimelech, A. Fonseca, S. Nejati, M. Elimelech, E. Engineering, N. Haven and U. States, *ACS Nano*, 2015, **9**, 7226–7236.

16 H. E. Karahan, Y. Wang, W. Li, F. Liu, L. Wang, X. Sui, M. A. Riaz and Y. Chen, *Biomater. Sci.*, 2018, **6**, 766–773.

17 F. Perreault, A. Fonseca De Faria and M. Elimelech, *Chem. Soc. Rev.*, 2015, **44**, 5861–5896.

18 K. Hu, D. D. Kulkarni, I. Choi and V. V Tsukruk, *Prog. Polym. Sci.*, 2014, **39**, 1934–1972.

19 H. Kim, A. A. Abdala and C. W. Macosko, 2010, 6515–6530.

20 A. Fairbrother, H. C. Hsueh, J. H. Kim, D. Jacobs, L. Perry, D. Goodwin, C. White, S. Watson and L. P. Sung, *Polym. Degrad. Stab.*, 2019, **165**, 153–160.

21 A. Deriszadeh, F. Shahraki, D. M. Kalhori and O. M. Jazani, *Prog. Org. Coatings*, 2019, **136**, 105292.

22 V. Mittal and A. U. Chaudhry, 510–521.

23 M. Nonahal, M. R. Saeb, S. H. Jafari, H. Rastin, H. A. Khonakdar, F. Najafi and F. Simon, 2018, 1–12.

24 P. Haghdadeh, M. Ghaffari, B. Ramezanzadeh and G. Bahlakeh, 2018, **86**, 199–212.

25 Y. Yang, Y. Komaki, S. Y. Kimura, H. Y. Hu, E. D. Wagner, B. J. Mariñas and M. J. Plewa, *Environ. Sci. Technol.*, 2014, **48**, 12362–12369.

26 S. D. Richardson, F. Fasano, J. J. Ellington, F. G. Crumley, K. M. Buettner, J. J. Evans, B. C. Blount, L. K. Silva, T. J. Waite, G. W. Luther, A. B. Mckague, R. J. Miltner, E. D. Wagner and M. J. Plewa, *Environ. Sci. Technol.*, 2008, **42**, 8330–8338.

27 M. J. Plewa, Y. Kargalioglu, D. Vankerk, R. A. Minear and E. D. Wagner, *Environ. Mol. Mutagen.*, 2002, **40**, 134–142.

28 C. Chen, O. G. Apul and T. Karanfil, *Water Res.*, 2017, **113**, 223–230.

29 J. Kidd, A. Barrios, O. Apul, F. Perreault and P. Westerhoff, *Environ. Eng. Sci.*, 2018, **35**, 988–995.

30 C. Marambio-Jones and E. M. V. Hoek, *J. Nanoparticle Res.*, 2010, **12**, 1531–1551.

31 M. Ema, N. Kobayashi, M. Naya, S. Hanai and J. Nakanishi, *Reprod. Toxicol.*, 2010, **30**, 343–352.

32 S. Dewasthale, I. Mani and K. Vasdev, *J. Appl. Biotechnol. Bioeng.*, 2018, **5**, 156–160.

33 M. H. Muhammad, A. L. Idris, X. Fan, Y. Guo, Y. Yu, X. Jin, J. Qiu, X. Guan and T. Huang, *Front. Microbiol.*, 2020, **11**, 1–20.

34 K. Mijnendonckx, N. Leys, J. Mahillon, S. Silver and R. Van Houdt, *BioMetals*, 2013, **26**, 609–621.

35 M. Ben-Sasson, X. Lu, E. Bar-Zeev, K. R. Zodrow, S. Nejati, G. Qi, E. P. Giannelis and M. Elimelech, *Water Res.*, 2014, **62**, 260–270.

36 D. Rice, A. C. Barrios, Z. Xiao, A. Bogler, E. B. Zeev and F. Perreault, *Water Res.*, 2018, **145**, 599–607.

37 L. M. Stabryla, K. A. Johnston, J. E. Millstone and L. M. Gilbertson, *Environ. Sci. Nano*, 2018, **5**, 2047–2068.

38 M. A. Radzig, V. A. Nadtochenko, O. A. Koksharova, J. Kiwi, V. A. Lipasova and I. A. Khmel, *Colloids Surfaces B Biointerfaces*, 2013, **102**, 300–306.

39 N. Durán, M. Durán, M. B. de Jesus, A. B. Seabra, W. J. Fávaro and G. Nakazato, *Nanomedicine Nanotechnology, Biol. Med.*, 2016, **12**, 789–799.

40 A. Ivask, A. Elbadawy, C. Kaweeteerawat, D. Boren, H. Fischer, Z. Ji, C. H. Chang, R. Liu, T. Tolaymat, D. Telesca, J. I. Zink, Y. Cohen, P. A. Holden and H. A. Godwin, *ACS Nano*, 2014, **8**, 374–386.

41 C. Levard, E. M. Hotze, B. P. Colman, A. L. Dale, L. Truong, X. Y. Yang, A. J. Bone, G. E. Brown, R. L. Tanguay, R. T. Di Giulio, E. S. Bernhardt, J. N. Meyer, M. R. Wiesner and G. V. Lowry, *Environ. Sci. Technol.*, 2013, **47**, 13440–13448.

42 D. He, S. Garg, Z. Wang, L. Li, H. Rong, X. Ma, G. Li, T. An and T. D. Waite, *Environ. Sci. Nano*, 2019, **6**, 1674–1687.

43 S. Wang, Z. Liu, W. Wang and H. You, *RSC Adv.*, 2017, **7**, 37065–37075.

44 M. I. Katsnelson, *Rev. Lit. Arts Am.*, 2007, **10**, 20–27.

45 K. S. Novoselov, A. K. Geim, S. V Morozov, D. Jiang, Y. Zhang, S. V Dubonos, I. V Grigorieva and A. A. Firsov, *Science (80-.).*, 2004, **306**, 666–669.

46 A. A. Balandin, *Nat. Mater.*, 2011, **10**, 569–581.

47 L. R. De Jesus, R. V. Dennis, S. W. Depner, C. Jaye, D. A. Fischer and S. Banerjee, *J. Phys. Chem. Lett.*, 2013, **4**, 3144–3151.

48 M. D. Rojas-Andrade, G. Chata, D. Rouholiman, J. Liu, C. Saltikov and S. Chen, *Nanoscale*, 2017, **9**, 994–1006.

49 H. Enis Karahan, Y. Wang, W. Li, F. Liu, L. Wang, X. Sui, M. A. Riaz and Y. Chen, *Biomater. Sci.*, 2018, **6**, 766–773.

50 A. Al-Jumaili, S. Alancherry, K. Bazaka and M. V. Jacob, *Materials (Basel).*, 2017, **10**, 1–26.

51 I. E. Mejías Carpio, C. M. Santos, X. Wei and D. F. Rodrigues, *Nanoscale*, 2012, **4**, 4746–4756.

52 H. M. Hegab, A. Elmekawy, L. Zou, D. Mulcahy, C. P. Saint and M. Ginic-Markovic, *Carbon N. Y.*, 2016, **105**, 362–376.

53 M. Di Giulio, R. Zappacosta, S. Di Lodovico, E. Di Campli, G. Siani, A. Fontana and L. Cellini, *Antimicrob. Agents Chemother.*, , DOI:10.1128/AAC.00547-18.

54 S. Gurunathan, J. W. Han, A. Abdal Dayem, V. Eppakayala and J. H. Kim, *Int. J. Nanomedicine*, 2012, **7**, 5901–5914.

55 S. Romero-Vargas Castrillón, F. Perreault, A. F. De Faria and M. Elimelech, *Environ. Sci. Technol. Lett.*, 2015, **2**, 112–117.

56 S. Liu, M. Hu, T. H. Zeng, R. Wu, R. Jiang, J. Wei, L. Wang, J. Kong and Y. Chen, *Langmuir*, 2012, **28**, 12364–12372.

57 O. Akhavan, E. Ghaderi and A. Esfandiar, *J. Phys. Chem. B*, 2011, **115**, 6279–6288.

58 L. M. Pasquini, R. C. Sekol, A. D. Taylor, L. D. Pfefferle and J. B. Zimmerman, *Environ. Sci. Technol.*, 2013, **47**, 8775–8783.

59 C. D. Vecitis, K. R. Zodrow, S. Kang and M. Elimelech, *ACS Nano*, 2010, **4**, 5471–5479.

60 G. Jia, H. Wang, L. Yan, X. Wang, R. Pei, T. Yan, Y. Zhao and X. Guo, *Environ. Sci. Technol.*, 2005, **39**, 1378–1383.

61 L. M. Pasquini, S. M. Hashmi, T. J. Sommer, M. Elimelech and J. B. Zimmerman, *Environ. Sci. Technol.*, 2012, **46**, 6297–6305.

62 L. M. Gilbertson, D. G. Goodwin, A. D. Taylor, L. Pfefferle and J. B. Zimmerman, *Environ. Sci. Technol.*, , DOI:10.1021/es500468y.

63 L. R. Arias and L. Yang, *Langmuir*, 2009, **25**, 3003–3012.

64 M. M. Falinski, D. L. Plata, S. S. Chopra, T. L. Theis, L. M. Gilbertson and J. B. Zimmerman, *Nat. Nanotechnol.*, 2018, **13**, 708–714.

65 E. J. Petersen and T. B. Henry, *Environ. Toxicol. Chem.*, 2012, **31**, 60–72.

66 L. M. Gilbertson, J. B. Zimmerman, D. L. Plata, J. E. Hutchison and P. T. Anastas, *Chem. Soc. Rev.*, 2015, **44**, 5758–5777.

67 M. Hofmann, J. Wei, Y. Chen, S. Liu, T. H. Zeng, M. Hofmann, E. Burcombe, J. Wei and R. Jiang, 2011, 6971–6980.

68 O. Akhavan and E. Ghaderi, *ACS Nano*, 2010, **4**, 5731–5736.

69 I. Zucker, J. R. Werber, Z. S. Fishman, S. M. Hashmi, U. R. Gabinet, X. Lu, C. O. Osuji, L. D. Pfefferle and M. Elimelech, *Environ. Sci. Technol. Lett.*, 2017, **4**, 404–409.

70 S. T. Odonkor and J. K. Ampofo, *Microbiol. Res. (Pavia).*, 2013, **4**, 2.

71 A. K. Chatterjee, R. Chakraborty and T. Basu, *Nanotechnology*, , DOI:10.1088/0957-4484/25/13/135101.

72 Z. Chen, R. Bertin and G. Froldi, *Food Chem.*, 2013, **138**, 414–420.

73 S. P. Melegari, F. Perreault, R. H. R. Costa, R. Popovic and W. G. Matias, *Aquat. Toxicol.*, 2013, **142**–**143**, 431–440.

74 R. H. Regel, J. M. Ferris, G. G. Ganf and J. D. Brookes, *Aquat. Toxicol.*, 2002, **59**, 209–223.

75 F. Perreault, A. Oukarroum, S. P. Melegari, W. G. Matias and R. Popovic, *Chemosphere*, 2012, **87**, 1388–1394.

76 G. L. Ellman, *Arch. Biochem. Biophys.*, 1959, **82**, 70–77.

77 A. Ganguly, S. Sharma, P. Papakonstantinou and J. Hamilton, *J. Phys. Chem. C*, 2011, **115**, 17009–17019.

78 C. A. Amadei, P. Arribas and C. D. Vecitis, *Carbon N. Y.*, 2018, **133**, 398–409.

79 D. Yang, A. Velamakanni, G. Bozoklu, S. Park, M. Stoller, R. D. Piner, S. Stankovich, I. Jung, D. A. Field, C. A. Ventrice and R. S. Ruoff, *Carbon N. Y.*, 2009, **47**, 145–152.

80 C. Mattevi, G. Eda, S. Agnoli, S. Miller, K. A. Mkhoyan, O. Celik, D. Mastrogiovanni, G. Granozzi, E. Carfunkel and M. Chhowalla, *Adv. Funct. Mater.*, 2009, **19**, 2577–2583.

81 A. Lerf, H. He, M. Forster and J. Klinowski, 1998, **5647**, 4477–4482.

82 O. Akhavan and E. Ghaderi, *Carbon N. Y.*, 2012, **50**, 1853–1860.

83 V. C. Sanchez, A. Jachak, R. H. Hurt and A. B. Kane, *Chem. Res. Toxicol.*, 2012, **25**, 15–34.

84 S. S. Nanda, D. K. Yi and K. Kim, *Sci. Rep.*, 2016, **6**, 1–12.

85 X. Lu, X. Feng, J. R. Werber, C. Chu, I. Zucker, J.-H. Kim, C. O. Osuji and M.

Elimelech, *Proc. Natl. Acad. Sci.*, 2017, **114**, E9793–E9801.

86 K. Krishnamoorthy, M. Veerapandian, L. H. Zhang, K. Yun and S. J. Kim, *J. Phys. Chem. C*, 2012, **116**, 17280–17287.

87 S. L. Hempel, G. R. Buettner, Y. Q. O'Malley, D. A. Wessels and D. M. Flaherty, *Free Radic. Biol. Med.*, 1999, **27**, 146–159.

88 N. M. Franklin, M. S. Adams, J. L. Stauber and R. P. Lim, *Arch. Environ. Contam. Toxicol.*, 2001, **40**, 469–480.

89 N. M. Franklin, J. L. Stauber and R. P. Lim, *Environ. Toxicol. Chem.*, 2001, **20**, 160–170.

90 N. Miyazawa, M. Hakamada and M. Mabuchi, *Sci. Rep.*, 2018, **8**, 1–8.

91 J. Chen, H. Peng, X. Wang, F. Shao, Z. Yuan and H. Han, *Nanoscale*, 2014, **6**, 1879–1889.

92 A. F. Faria, F. Perreault and M. Elimelech, *ACS Appl. Nano Mater.*, , DOI:10.1021/acsanm.7b00332.

93 X. Liu, S. Sen, J. Liu, I. Kulaots, D. Geohegan, A. Kane, A. A. Puretzky, C. M. Rouleau, K. L. More, G. T. R. Palmore and R. H. Hurt, *Small*, 2011, **7**, 2775–2785.

94 C. M. Santos, M. C. R. Tria, R. A. M. V. Vergara, F. Ahmed, R. C. Advincula and D. F. Rodrigues, *Chem. Commun.*, 2011, **47**, 8892–8894.

95 J. D. Mangadlao, C. M. Santos, M. J. L. Felipe, A. C. C. De Leon, D. F. Rodrigues and R. C. Advincula, *Chem. Commun.*, 2015, **51**, 2886–2889.

96 V. Palmieri, M. C. Lauriola, G. Ciasca, C. Conti, M. De Spirito and M. Papi, *Nanotechnology*, 2017, **28**, 1–18.

97 Y. Li, H. Yuan, A. von dem Bussche, M. Creighton, R. H. Hurt, A. B. Kane and H. Gao, *Proc. Natl. Acad. Sci.*, 2013, **110**, 12295–12300.

98 L. Hui, J. G. Piao, J. Auletta, K. Hu, Y. Zhu, T. Meyer, H. Liu and L. Yang, *ACS Appl. Mater. Interfaces*, 2014, **6**, 13183–13190.

99 J. Xue, S. BinAhmed, Z. Wang, N. G. Karp, B. L. Stottrup and S. Romero-Vargas Castrillón, *Environ. Sci. Technol. Lett.*, 2018, **5**, 14–19.

100 Y. Zhang, T. R. Nayak, H. Hong and W. Cai, *Nanoscale,* 2012, **4**, 3833–3842.

101 Y. Huang, J. Liang and Y. Chen, *Small*, 2012, **8**, 1805–1834.

102 Report, *Graphene Market Size, Share & Trends Analysis Report By Application (Electronics, Composites, Energy), By Product (Graphene Nanoplatelets, Graphene Oxide), By Region, And Segment Forecasts, 2020 - 2027*, 2020, vol. 2027.

103 D. R. Dreyer, S. Park, C. W. Bielawski and R. S. Ruoff, *Chem. Soc. Rev.*, 2010, **39**, 228–240.

104 A. Bianco, H. M. Cheng, T. Enoki, Y. Gogotsi, R. H. Hurt, N. Koratkar, T. Kyotani, M. Monthioux, C. R. Park, J. M. D. Tascon and J. Zhang, *Carbon N. Y.*, 2013, **65**, 1–6.

105 Y. Zhang, T. Meng, L. Shi, X. Guo, X. Si, R. Yang and X. Quan, *Sci. Total Environ.*, 2019, **649**, 163–171.

106 A. B. Seabra, A. J. Paula, R. De Lima, O. L. Alves and N. Durán, *Chem. Res. Toxicol.*, 2014, **27**, 159–168.

107 H. E. Karahan, L. Wei, K. Goh, Z. Liu, Ö. Birer, F. Dehghani, C. Xu, J. Wei and Y. Chen, *Nanoscale*, 2016, **8**, 17181–17189.

108 H. N. Nguyen, S. L. Castro-Wallace and D. F. Rodrigues, *Environ. Sci. Nano*, 2017, **4**, 160–169.

109 C. Hu, Q. Wang, H. Zhao, L. Wang, S. Guo and X. Li, *Chemosphere*, 2015, **128**, 184–190.

110 T. Mesarič, K. Sepčič, V. Piazza, C. Gambardella, F. Garaventa, D. Drobne and M. Faimali, *Chem. Ecol.*, 2013, **29**, 643–652.

111 M. Chen, J. Yin, Y. Liang, S. Yuan, F. Wang, M. Song and H. Wang, *Aquat. Toxicol.*, 2016, **174**, 54–60.

112 X. Yang, Q. Yang, G. Zheng, S. Han, F. Zhao, Q. Hu and Z. Fu, *Environ. Toxicol.*, 2019, **34**, 415–423.

113 H. Li, F. Cao, F. Zhao, Y. Yang, M. Teng, C. Wang and L. Qiu, *Chemosphere*, 2018, **207**, 781–790.

114 B. Khan, A. S. Adeleye, R. M. Burgess, S. M. Russo and K. T. Ho, *Aquat. Toxicol.*, 2019, **216**, 105297.

115 B. Khan, A. S. Adeleye, R. M. Burgess, R. Smolowitz, S. M. Russo and K. T. Ho, *Environ. Toxicol. Chem.*, 2019, **38**, 820–830.

116 S. Du, P. Zhang, R. Zhang, Q. Lu, L. Liu, X. Bao and H. Liu, *Chemosphere*, 2016, **164**, 499–507.

117 S. Loureiro, S. Filipe, G. Gonçalves, M. Jesús, S. Rebelo, M. Carmona and M. Vila, *Ecotoxicol. Environ. Saf.*, 2018, **162**, 192–200.

118 X. Lv, Y. Yang, Y. Tao, Y. Jiang, B. Chen, X. Zhu, Z. Cai and B. Li, *Environ. Pollut.*, 2018, **234**, 953–959.

119 Y. Liu, W. Han, Z. Xu, W. Fan, W. Peng and S. Luo, *Environ. Pollut.*, 2018, **237**, 218–227.

120 A. C. Barrios, Y. Wang and L. M. Gilbertson, , DOI:10.1021/acs.est.9b05057.

121 A. R. Deline, B. P. Frank, C. L. Smith, L. R. Sigmon, A. N. Wallace, M. J. Gallagher, D. G. Goodwin, D. P. Durkin and D. Howard Fairbrother, *Chem. Rev.*, 2020, **120**, 11651–11697.

122 P. Radix, M. Léonard, C. Papantoniou, G. Roman, E. Saouter, S. Gallotti-Schmitt, H. Thiébaud and P. Vasseur, *Ecotoxicol. Environ. Saf.*, 2000, **47**, 186–194.

123 A. Chalifour, A. LeBlanc, L. Sleno and P. Juneau, *Ecotoxicology*, 2016, **25**, 1822–1831.

124 H. K. Lichtenthaler, *Chlorophylls Carotenoids Pigment. Photosynth. Biomembr.*, 1987, **148**, 350–382.

125 ISO 6341, 2012, **6341**, 11.

126 ABNT. Associação Brasileira de Normas Técnicas, 2016, 1–23.

127 M. A. Hamilton, R. C. Russo and R. V Thurston, 1975, **566**, 714–719.

128 H. Aebi, *Methods Enzymol.*, 1984, **105**, 121–126.

129 E. Ann Ellis, *Micros. Today*, 2006, **14**, 32–33.

130 N. Hanaichi, T., Sato, T., Iwamoto, T., Malavasi-Yamashiro, J., Hoshing, M., Mizuno, *J. Electron Microsc. (Tokyo).*, 1986, **35**, 304–306.

131 Y. Liu, W. Fan, Z. Xu, W. Peng and S. Luo, *Environ. Pollut.*, 2018, **236**, 962–970.

132 Y. Wang, Y. Basdogan, T. Zhang, R. S. Lankone, A. N. Wallace, D. H. Fairbrother, J. A. Keith and L. M. Gilbertson, *ACS Appl. Mater. Interfaces*, 2020, **12**, 45753–45762.

133 E. Cruces, A. C. Barrios, Y. P. Cahue, B. Januszewski, L. M. Gilbertson and F. Perreault, *Chemosp*, 2020, in press.

134 M. Baalousha, *NanoImpact*, 2017, **6**, 55–68.

135 I. Chowdhury, N. D. Mansukhani, L. M. Guiney, M. C. Hersam and D. Bouchard, *Environ. Sci. Technol.*, 2015, **49**, 10886–10893.

136 N. Ye, Z. Wang, S. Wang, H. Fang and D. Wang, *Environ. Sci. Pollut. Res.*, 2018, **25**, 10956–10965.

137 K. Yang, B. Chen, X. Zhu and B. Xing, *Environ. Sci. Technol.*, 2016, **50**, 11066–11075.

138 M. Wang, Y. Niu, J. Zhou, H. Wen, Z. Zhang, D. Luo, D. Gao, J. Yang, D. Liang and Y. Li, *Nanoscale*, 2016, **8**, 14587–14592.

139 S. D. Story, S. Boggs, L. M. Guiney, M. Ramesh, M. C. Hersam, C. J. Brinker and S. L. Walker, *J. Colloid Interface Sci.*, 2020, **561**, 849–853.

140 Y. Jiang, R. Raliya, J. D. Fortner and P. Biswas, *Environ. Sci. Technol.*, 2016, **50**, 6964–6973.

141 J. Zhao, Z. Wang, J. C. White and B. Xing, *Environ. Sci. Technol.*, 2014, **48**, 9995–10009.

142 J. Yin, W. Fan, J. Du, W. Feng, Z. Dong, Y. Liu and T. Zhou, *Environ. Pollut.*, 2020, **260**, 113847.

143 Y. Tang, J. Tian, S. Li, C. Xue, Z. Xue, D. Yin and S. Yu, *Sci. Total Environ.*, 2015, **532**, 154–161.

144 Z. Zeng, K. Yang and D. Lin, *Aquat. Toxicol.*, 2019, **216**, 105323.

145 A. Baun, N. B. Hartmann, K. Grieger and K. O. Kusk, *Ecotoxicology*, 2008, **17**, 387–395.

146 Y. Liu, W. Fan, Z. Xu, W. Peng and S. Luo, *Environ. Pollut.*, 2018, **236**, 962–970.

147 L. M. Skjolding, K. Kern, R. Hjorth, N. Hartmann, S. Overgaard, G. Ma, J. G. C. Veinot and A. Baun, *Ecotoxicology*, 2014, **23**, 1172–1183.

148 F. R. Khan, G. M. Kennaway, M. N. Croteau, A. Dybowska, B. D. Smith, A. J. A. Nogueira, P. S. Rainbow, S. N. Luoma and E. Valsami-Jones, *Chemosphere*, 2014, **100**, 97–104.

149 S. S. Nanda, S. S. A. An and D. K. Yi, *Int. J. Nanomedicine*, 2015, **10**, 549–556.

150 P. F. M. Nogueira, D. Nakabayashi and V. Zucolotto, *Aquat. Toxicol.*, 2015, **166**, 29–35.

151 H. Xin, Y. Tang, S. Liu, X. Yang, S. Xia, D. Yin and S. Yu, *ACS Omega*, 2018,

16969–16975.

152 T. Dutta, R. Sarkar, B. Pakhira, S. Ghosh, R. Sarkar, A. Barui and S. Sarkar, *RSC Adv.*, 2015, **5**, 80192–80195.

153 D. J. Dwyer, M. A. Kohanski and J. J. Collins, *Curr. Opin. Microbiol.*, 2009, **12**, 482–489.

154 L. Barhoumi, A. Oukarroum, L. Ben Taher, L. S. Smiri, H. Abdelmelek and D. Dewez, *Arch. Environ. Contam. Toxicol.*, 2015, **68**, 510–520.

155 D. L. Berglund and S. Eversman, *Cytometry*, 1988, **9**, 150–155.

156 L. Giannuzzi, B. Krock, M. C. C. Minaglia, L. Rosso, C. Houghton, D. Sedan, G. Malanga, M. Espinosa, D. Andrinolo and M. Hernando, *Comp. Biochem. Physiol. Part - C Toxicol. Pharmacol.*, 2016, **189**, 22–30.

157 A. Latifi, M. Ruiz and C. Zhang, 2009, **33**, 258–278.

158 C. M. Rico, J. Hong, M. I. Morales, L. Zhao, A. C. Barrios, J. Y. Zhang, J. R. Peralta-Videa and J. L. Gardea-Torresdey, *Environ. Sci. Technol.*, 2013, **47**, 5635–5642.

159 J. Zhao, X. Cao, Z. Wang, Y. Dai and B. Xing, *Water Res.*, 2017, **111**, 18–27.

160 Y. Wu, H. Ge and Z. Zhou, *Environ. Sci. Pollut. Res.*, 2015, **22**, 8471–8479.

161 J. Li, D. Ou, L. Zheng, N. Gan and L. Song, *Phycol. Res.*, 2011, **59**, 200–207.

162 F. Schwab, T. D. Bucheli, L. P. Lukhele, A. Magrez, B. Nowack, L. Sigg and K. Knauer, *Environ. Sci. Technol.*, 2011, **45**, 6136–6144.

163 E. Hoiczyk and A. Hansel, *J. Bacteriol.*, 2000, **182**, 1191–1199.

164 J. F. Rabek, *Appl. Sci.*

165 W. Sansbury, .

166 M. Rajabi, G. R. Rashed and D. Zaarei, *Corros. Eng. Sci. Technol.*, 2015, **50**, 509–516.

167 Y. Cui, S. I. Kundalwal and S. Kumar, 1–57.

168 M. C. Carrera, E. Erdmann and H. A. Destéfanis, .

169 B. M. Yoo, H. J. Shin, H. W. Yoon and H. B. Park, 2014, **39628**, 1–23.

170 B. Ramezanzadeh, E. Ghasemi, M. Mahdavian and E. Changizi, *Carbon N. Y.*, 2015,

93, 555–573.

171 H. Yang, C. Shan, F. Li, Q. Zhang, D. Han and L. Niu, 2009, 8856–8860.

172 K. C. Chang, M. H. Hsu, H. I. Lu, M. C. Lai, P. J. Liu, C. H. Hsu, W. F. Ji, T. L. Chuang, Y. Wei, J. M. Yeh and W. R. Liu, *Carbon N. Y.*, 2014, **66**, 144–153.

173 Y. Dang, N. Xie, A. Kessel, E. McVey, A. Pace and X. Shi, *Constr. Build. Mater.*, 2014, **55**, 128–135.

174 L. Wu, S. V Hoa and H. Wang, 2007, 323–330.

175 L. F. Cole, *Epoxy resins and polyurethane foams for low pressure injection crack repair*, 2000.

176 A. Ghasemi-Kahrizsangi, J. Neshati, H. Shariatpanahi and E. Akbarinezhad, *Prog. Org. Coatings*, 2015, **85**, 199–207.

177 Z. Iskanderova, J. Kleiman, Y. Gudimenko, R. C. Tennyson and W. D. Morison, *Surf. Coatings Technol.*, 2000, **127**, 18–23.

178 T. Nguyen, B. Pellegrin, L. Mermet, A. Shapiro, X. Gu and J. Chin, 2009, **1**, 90–93.

179 B. Pellegrin, T. Nguyen, L. Mermet, A. Shapiro, X. Gu and J. Chin, 2009, **1**, 94–97.

180 G. B. Olowojoba, S. Eslava and E. S. Gutierrez, *Appl. Nanosci.*, 2016, **6**, 1015–1022.

181 D. G. Goodwin, I. Boyer, T. Devahif, C. Gao, B. P. Frank, X. Lu, L. Kuwama, T. B. Gordon, J. Wang, J. F. Ranville, E. J. Bouwer and D. H. Fairbrother, *Environ. Sci. Technol.*, 2018, **52**, 40–51.

182 D. G. Goodwin, A. S. Adeleye, L. Sung, K. T. Ho, R. M. Burgess and E. J. Petersen, , DOI:10.1021/acs.est.7b04938.

183 T. Bernard, C., Goodwin, D.G., Gu, X., Celina, M., Nyden, M., Jacobs, D., Sung, L., Nguyen, *J. Coat. Technol. Res.*, 2020, **17**, 255–269.

184 J. Chin, E. Byrd, N. Embree, J. Garver, B. Dickens, T. Finn and J. Martin, *Rev. Sci. Instrum.*, 2004, **75**, 4951–4959.

185 L. Goodwin, David G.; Lyu, Yadong; Lu, Chen Yuan; Campos, Alejandro; Reipa, Vytas; Nguyen, Tinh; Sung, *TBD*.

186 D. G. Goodwin, S. Shen, Y. Lyu, R. Lankone and A. C. Barrios, 2020, 1–35.

187 Y. D. C. De Oliveira, L. G. Amurin, F. C. F. Valim, G. J. M. Fechine and R. J. E.

Andrade, *Polymer (Guildf).*, 2019, **176**, 146–158.

188 F. Shehzad, M. I. Ahmad and M. A. Al-Harthi, *J. Appl. Polym. Sci.*, 2019, **136**, 1–9.

189 K. Hu, D. D. Kulkarni, I. Choi and V. V. Tsukruk, *Prog. Polym. Sci.*, 2014, **39**, 1934–1972.

190 B. P. Singh, S. Nayak, K. K. Nanda, S. Bhattacharjee, L. Besra and B. Kumar, *Carbon N. Y.*, 2013, **61**, 47–56.

191 N. T. Kirkland, T. Schiller, N. Medhekar and N. Birbilis, *Corros. Sci.*, 2012, **56**, 1–4.

192 W. Wohlleben, C. Kingston, J. Carter, E. Sahle-demessie, B. Acrey, C. Chen and E. Walton, 2017, **113**, 346–360.

193 J. F. Rabek, in *Polymer Degradation*, 1995, pp. 269–273.

194 D. G. Goodwin, S. J. Shen, Y. Lyu, R. Lankone, A. C. Barrios, S. Kabir, F. Perreault, W. Wohlleben, T. Nguyen and L. Sung, *Polym. Degrad. Stab.*, , DOI:10.1016/j.polymdegradstab.2020.109365.

195 D. G. Goodwin, T. Lai, Y. Lyu, C. Y. Lu, A. Campos, V. Reipa, T. Nguyen and L. Sung, *NanoImpact*, 2020, **19**, 100249.

196 J. Bin Wu, M. L. Lin, X. Cong, H. N. Liu and P. H. Tan, *Chem. Soc. Rev.*, 2018, **47**, 1822–1873.

197 W. C. Hou, I. Chowdhury, D. G. Goodwin, W. M. Henderson, D. H. Fairbrother, D. Bouchard and R. G. Zepp, *Environ. Sci. Technol.*, 2015, **49**, 3435–3443.

198 M. Shams, L. M. Guiney, L. Huang, M. Ramesh, X. Yang, M. C. Hersam and I. Chowdhury, *Environ. Sci. Nano*, 2019, **6**, 2203–2214.

199 D. Cutler and G. Miller, *Demography*, 2005, **42**, 1–22.

200 Y. Kurokawa, A. Maekawa, M. Takahashi and Y. Hayashi, *Environ. Health Perspect.*, 1990, **87**, 309–335.

201 G. Hua and D. A. Reckhow, *Water Res.*, 2007, **41**, 1667–1678.

202 U. Von Gunten, *Water Res.*, 2003, **37**, 1469–1487.

203 R. McTigue, N.E.; Cornwell, D.A.; Graf, K.; Brown, *Am. Water Work. Assoc.*

204 Environmental Protection Agency (EPA), *Fed. Regist.*, 2006, **71**, 388–493.

205 S. D. Plewa, M.J.; Wagner, E.D.; Muellner, M.G.; Hsu, K.; Richardson, in *ACS Symposium Series*, 2008, vol. 995, pp. 36–50.

206 G. L. Minear, R.A.; Amy, *Disinfection by-products in water treatment: the chemistry of their formation and control*, Boca Raton: Lewis Publishers, 1996.

207 J. Davis, S.N.; Whittemore, D.O.; Fabryka-Martin, *Groundwater*, 1998, **36**, 338–350.

208 S. D. Richardson and C. Postigo, *Liquid Chromatography–Mass Spectrometry of Emerging Disinfection By-products*, Elsevier Ltd, 2018, vol. 79.

209 K. Watson and K. Watson, *Disinfection By - Products in Transformation and R Emoval Strategies .*, 2014.

210 M. S. Amy, G.L.; Siddiqui, *Strategies to control bromate and bromide*, 1991.

211 P. Gan, W.; Venkatesan, A.J.; Apul, O.G.; Perreault, F.; Yang, X.; Westerhoff, *Am. Water Work. Assoc.*, 2018, **110**, 13–24.

212 V. C. Tung, M. J. Allen, Y. Yang and R. B. Kaner, *Nat. Nanotechnol.*, 2009, **4**, 25–29.

213 D. C. Marcano, D. V. Kosynkin, J. M. Berlin, A. Sinitskii, Z. Sun, A. Slesarev, L. B. Alemany, W. Lu and J. M. Tour, *ACS Nano*, 2010, **4**, 4806–4814.

214 L. Staudenmaier, *Mittheilungen*, 1898, **14**, 1481–1487.

215 A. F. De Faria, F. Perreault, E. Shaulsky, L. H. Arias Chavez and M. Elimelech, *ACS Appl. Mater. Interfaces*, 2015, **7**, 12751–12759.

216 P. Westerhoff, Y. Yoon, S. Snyder and E. Wert, *Environ. Sci. Technol.*, 2005, **39**, 6649–6663.

217 W. Shao, X. Liu, H. Min, G. Dong, Q. Feng and S. Zuo, *ACS Appl. Mater. Interfaces*, 2015, **7**, 6966–6973.

218 M. R. Das, R. K. Sarma, R. Saikia, V. S. Kale, M. V. Shelke and P. Sengupta, *Colloids Surfaces B Biointerfaces*, 2011, **83**, 16–22.

219 N. E. Mctigue, D. A. Cornwell, K. Graf and R. Brown, *J. - Am. Water Work. Assoc.*, **106**, E492–E508.

220 D. Kim, G. L. Amy and T. Karanfil, *Water Res.*, 2015, **81**, 343–355.

221 W. Gan, A. K. Venkatesan, O. G. Apul, F. Perreault, X. I. N. Yang and P. Westerhoff, *Am. Water Work. Assoc.*, 2018, **110**, 13–24.

222 C. Chen, O. G. Apul and T. Karanfil, *Water Res.*, 2017, **113**, 223–230.

223 S. Ghosh and L. Manna, , DOI:10.1021/acs.chemrev.8b00158.

224 B. Tang, S. Xu, J. An, B. Zhao and J. R. Lombardi, *Phys. Chem. Chem. Phys.*, 2009, **11**, 10286–10292.

225 B. Wiley, T. Herricks, Y. Sun and Y. Xia, *Nano Lett.*, 2004, **4**, 1733–1739.

226 J. An, B. Tang, X. Zheng, J. Zhou, F. Dong, S. Xu, Y. Wang, B. Zhao and W. Xu, *J. Phys. Chem. C*, 2008, **112**, 15176–15182.

227 P. Westerhoff, P. Alvarez, Q. Li, J. Gardea-Torresdey and J. Zimmerman, *Environ. Sci. Nano*, 2016, **3**, 1241–1253.

228 A. Y. Hoekstra, M. M. Mekonnen, A. K. Chapagain, R. E. Mathews and B. D. Richter, *PLoS One*, , DOI:10.1371/journal.pone.0032688.

229 M. Elimelech and W. A. Phillip, *Science (80-.).*, 2011, **333**, 712–717.

230 J. R. Werber, C. O. Osuji and M. Elimelech, *Nat. Rev. Mater.*, , DOI:10.1038/natrevmats.2016.18.

231 G. Amy, N. Ghaffour, Z. Li, L. Francis, R. V. Linares, T. Missimer and S. Lattemann, *Desalination*, 2017, **401**, 16–21.

232 J. S. Baker and L. Y. Dudley, *Desalination*, 1998, **118**, 81–89.

233 C. Dreszer, H. C. Flemming, A. Zwijnenburg, J. C. Kruithof and J. S. Vrouwenvelder, *Water Res.*, 2014, **50**, 200–211.

234 M. Herzberg and M. Elimelech, *J. Memb. Sci.*, 2007, **295**, 11–20.

235 H. Flemming, *Exp. Therm. Fluid Sci.*, , DOI:10.1007/978-94-011-1824-8.

236 S. S. Madaeni, T. Mohamamdi and M. K. Moghadam, *Desalination*, 2001, **134**, 77–82.

237 F. Ridgeway, Harry, *Biological fouling of separation membranes used in water treatment applications*, AWWA Research Foundation, 2003.

238 V. Kochkodan and N. Hilal, *Desalination*, 2015, **356**, 187–207.

239 D. Rana and T. Matsuura, *Chem. Rev.*, 2010, **110**, 2448–71.

240 A. Bogler, S. Lin and E. Bar-Zeev, *J. Memb. Sci.*, 2017, **542**, 378–398.

241 M. R. Hibbs, L. K. McGrath, S. Kang, A. Adout, S. J. Altman, M. Elimelech and C. J. Cornelius, *Desalination*, 2016, **380**, 52–59.

242 N. Akar, B. Asar, N. Dizge and I. Koyuncu, *J. Memb. Sci.*, 2013, **437**, 216–226.

243 A. Inurria, P. Cay-Durgun, D. Rice, H. Zhang, D. K. Seo, M. L. Lind and F. Perreault, *Desalination*, 2019, **451**, 139–147.

244 G. Ye, J. Lee, F. Perreault and M. Elimelech, *ACS Appl. Mater. Interfaces*, , DOI:10.1021/acsami.5b06647.

245 M. Ben-Sasson, K. R. Zodrow, Q. Genggeng, Y. Kang, E. P. Giannelis and M. Elimelech, *Environ. Sci. Technol.*, 2014, **48**, 384–393.

246 A. Soroush, W. Ma, Y. Silvino and M. S. Rahaman, *Environ. Sci. Nano*, 2015, **2**, 395–405.

247 A. Soroush, W. Ma, M. Cyr, M. S. Rahaman, B. Asadishad and N. Tufenkji, *Environ. Sci. Technol. Lett.*, 2016, **3**, 13–18.

248 M. Ben-Sasson, X. Lu, E. Bar-Zeev, K. R. Zodrow, S. Nejati, G. Qi, E. P. Giannelis and M. Elimelech, *Water Res.*, 2014, **62**, 260–270.

249 A. F. Faria, C. Liu, M. Xie, F. Perreault, L. D. Nghiem, J. Ma and M. Elimelech, *J. Memb. Sci.*, 2017, **525**, 146–156.

250 J. Yin, Y. Yang, Z. Hu and B. Deng, *J. Memb. Sci.*, 2013, **441**, 73–82.

251 K. Zodrow, L. Brunet, S. Mahendra, D. Li, A. Zhang, Q. Li and P. J. J. Alvarez, *Water Res.*, 2009, **43**, 715–723.

252 A. Zirehpour, A. Rahimpour, A. Arabi Shamsabadi, M. G. Sharifian and M. Soroush, *Environ. Sci. Technol.*, 2017, **51**, 5511–5522.

253 S. Prabhu and E. K. Poulose, *Int. Nano Lett.*, 2012, 1–10.

254 I. Kurvet, A. Kahru, O. Bondarenko, A. Ivask and A. Ka, , DOI:10.1371/journal.pone.0064060.

255 W. Li, X. Xie and Q. Shi, 2010, 1115–1122.

256 Z. M. Xiu, Q. B. Zhang, H. L. Puppala, V. L. Colvin and P. J. J. Alvarez, *Nano Lett.*, , DOI:10.1021/nl301934w.

257 C. Levard, E. M. Hotze, G. V. Lowry and G. E. Brown, *Environ. Sci. Technol.*, 2012, **46**, 6900–6914.

258 J. Liu, D. A. Sonshine, S. Shervani and R. H. Hurt, *ACS Nano*, 2010, **4**, 6903–6913.

259 A. F. De Faria, D. S. T. Martinez, S. M. M. Meira, A. C. M. de Moraes, A. Brandelli, A. G. S. Filho and O. L. Alves, *Colloids Surfaces B Biointerfaces*, 2014, **113**, 115–124.

260 L. Tang, K. J. T. Livi and K. L. Chen, *Environ. Sci. Technol. Lett.*, 2015, **2**, 59–65.

261 Z. Liu and Y. Hu, *ACS Appl. Mater. Interfaces*, 2016, **8**, 21666–21673.

262 L. Qi, Y. Hu, Z. Liu, X. An and E. Bar-Zeev, *Environ. Sci. Technol.*, 2018, **52**, 9684–9693.

263 Z. Liu, L. Qi, X. An, C. Liu and Y. Hu, *ACS Appl. Mater. Interfaces*, 2017, **9**, 40987–40997.

264 Y. Bi, B. Han, S. Zimmerman, F. Perreault, S. Sinha and P. Westerhoff, *Water Res.*, 2018, **143**, 77–86.

265 P. Glueckstern, M. Priel, E. Gelman and N. Perlov, *Desalination*, 2008, **222**, 151–164.

266 M. D. Johnston, E. Simons and R. J. W. Lambert, 2000, 237–242.

267 K. P. Koutsoumanis and A. Lianou, 2013, **79**, 2294–2301.

268 K. P. Koutsoumanis, 2015, **45**, 216–221.

269 J. A. Brant, K. M. Johnson and A. E. Childress, *Colloids Surfaces A Physicochem. Eng. Asp.*, 2006, **280**, 45–57.

270 Y. Kim, S. Lee, J. Kuk and S. Hong, *Desalination*, 2015, **367**, 154–160.

271 E. M. V. Hoek, S. Bhattacharjee and M. Elimelech, *Langmuir*, 2003, **19**, 4836–4847.

272 B. C. Reinsch, C. Levard, Z. Li, R. Ma, A. Wise, K. B. Gregory, G. E. Brown and G. V. Lowry, *Environ. Sci. Technol.*, 2012, **46**, 6992–7000.

273 C. Levard, B. C. Reinsch, F. M. Michel, C. Oumahi, G. V. Lowry and G. E. Brown, *Environ. Sci. Technol.*, 2011, **45**, 5260–5266.

274 M. Pang, J. Hu and H. C. Zeng, *J. Am. Chem. Soc.*, 2010, **132**, 10771–10785.

275 S. M. Magaña, P. Quintana, D. H. Aguilar, J. A. Toledo, C. Ángeles-Chávez, M. A. Cortés, L. León, Y. Freile-Pelegrín, T. López and R. M. T. Sánchez, *J. Mol. Catal. A Chem.*, 2008, **281**, 192–199.

276 L. Li, Y. Wang, Q. Liu and G. Jiang, *Environ. Sci. Technol.*, 2016, **50**, 188–196.

277 G. Goncalves, P. A. A. P. Marques, C. M. Granadeiro, H. I. S. Nogueira, M. K. Singh and J. Grácio, *Chem. Mater.*, 2009, **21**, 4796–4802.

278 K. Spilarewicz-Stanek, A. Kisielewska, J. Ginter, K. Bałuszyńska and I. Piwoński, *RSC Adv.*, 2016, **6**, 60056–60067.

279 K. P. Lee, T. C. Arnot and D. Mattia, *J. Memb. Sci.*, 2011, **370**, 1–22.

280 E. M. Vrijenhoek, S. Hong and M. Elimelech, *J. Memb. Sci.*, 2001, **188**, 115–128.

281 S. W. Lee, S. Y. Park, Y. Kim, H. Im and J. Choi, *Sci. Total Environ.*, 2016, **553**, 565–573.

282 D. Ma, X. Hu, H. Zhou, J. Zhang and Y. Qian, *J. Cryst. Growth*, 2007, **304**, 163–168.

283 O. Choi, T. E. Clevenger, B. Deng, R. Y. Surampalli, L. Ross and Z. Hu, *Water Res.*, 2009, **43**, 1879–1886.

284 D. L. Starnes, J. M. Unrine, C. P. Starnes, B. E. Collin, E. K. Oostveen, R. Ma, G. V. Lowry, P. M. Bertsch and O. V. Tsyusko, *Environ. Pollut.*, 2015, **196**, 239–246.

285 G. P. Devi, K. B. A. Ahmed, M. K. N. S. Varsha, B. S. Shrijha, K. K. S. Lal, V. Anbazhagan and R. Thiagarajan, *Aquat. Toxicol.*, 2015, **158**, 149–156.

286 R. J. Barnes, R. R. Bandi, F. Chua, J. Hui, T. Aung, N. Barraud, A. G. Fane, S. Kjelleberg and S. A. Rice, *J. Memb. Sci.*, 2014, **466**, 161–172.

287 S. Gurunathan, J. W. Han, A. A. Dayem, V. Eppakayala, M. R. Park, D. N. Kwon and J. H. Kim, *J. Ind. Eng. Chem.*, 2013, **19**, 1280–1288.

288 W. Hu, C. Peng, W. Luo, M. Lv, X. Li, D. Li, Q. Huang and C. Fan, *ACS Nano*, 2010, **4**, 4317–4323.

289 S. Liu, T. H. Zeng, M. Hofmann, E. Burcombe, J. Wei, R. Jiang, J. Kong and Y. Chen, *ACS Nano*, 2011, **5**, 6971–6980.

290 A. Ray Chowdhuri, S. Tripathy, S. Chandra, S. Roy and S. K. Sahu, *RSC Adv.*, 2015, **5**, 49420–49428.

291 H. Khawaja, E. Zahir, M. A. Asghar and M. A. Asghar, *Colloids Surfaces A Physicochem. Eng. Asp.*, 2018, **555**, 246–255.

292 L. Sun, T. Du, C. Hu, J. Chen, J. Lu, Z. Lu and H. Han, *ACS Sustain. Chem. Eng.*, 2017, **5**, 8693–8701.

293 J. Tang, Q. Chen, L. Xu, S. Zhang, L. Feng, L. Cheng, H. Xu, Z. Liu and R. Peng, *ACS Appl. Mater. Interfaces*, 2013, **5**, 3867–3874.

294 Y. Tu, M. Lv, P. Xiu, T. Huynh, M. Zhang, M. Castelli, Z. Liu, Q. Huang, C. Fan, H. Fang and R. Zhou, *Nat. Nanotechnol.*, 2013, **8**, 594–601.

295 A. C. Barrios, Y. Wang, L. M. Gilbertson and F. Perreault, *Environ. Sci. Technol.*, 2019, **53**, 14679–14687.

296 C. Li, N. Zhang, J. Chen, J. Ji, X. Liu, J. Wang, J. Zhu and Y. Ma, *Environ. Pollut.*, 2019, **255**, 113150.

297 D. S. T. Castro, Vera L; Clemente, Zaira; Johnson, Claudio; Silva, Mariana; Vallim, José Henrique; Zigiotto de Medeiros, Aline Maria; Martinez, 2018, **37**, 1998–2012.

298 Y. Ni, Lingfeng; Li, *RSC Adv.*, 2018, **8**, 41358–41367.

299 Y. Liu, W. Fan, Z. Xu, W. Peng and S. Luo, , DOI:10.1016/j.carbon.2017.06.087.

300 N. Ye, Z. Wang, S. Wang, W. J. G. M. Peijnenburg, N. Ye, Z. Wang, S. Wang and W. J. G. M. Peijnenburg, *Nanotoxicology*, 2018, **12**, 423–438.

301 A. M. Cano, J. D. Maul, M. Saed, S. A. Shah, M. J. Green and J. E. Cañas-Carrell, 2017, **36**, 2199–2204.

302 S. Li, X. Pan, L. K. Wallis, Z. Fan, Z. Chen and S. A. Diamond, 2014, **112**, 62–69.

303 C. Hu, N. Hu, X. Li and Y. Zhao, *Ecotoxicol. Environ. Saf.*, 2016, **132**, 360–365.

304 Y. Zhang, T. Meng, X. Guo, R. Yang, X. Si and J. Zhou, *Chemosphere*, 2018, **197**, 749–758.

305 Y. Tang, J. Tian, S. Li, C. Xue, Z. Xue, D. Yin and S. Yu, *Sci. Total Environ.*, 2015, **532**, 154–161.

306 S. Pei and H. M. Cheng, *Carbon N. Y.*, 2012, **50**, 3210–3228.

APPENDIX A

SUPPLEMENTARY INFORMATION FOR CHAPTER 2: STRUCTURE-PROPERTY-TOXICITY RELATIONSHIPS OF GRAPHENE OXIDE: ROLE OF SURFACE CHEMISTRY ON THE MECHANISM OF INTERACTION WITH BACTERIA

Tables

Table A.1. Impurities in as received GO (ARGO) and thermally annealed GO (TGOs) samples by XPS analysis. Different letters represent statistical differences between materials at $p \leq 0.05$.

Samples	%N 1s	%Na 1s	%S 2p	%Si 2p
ARGO	0.76 ± 0.15 a	0.23 ± 0.07 c	0.52 ± 0.04 a	0.31 a
TGO200	0.59 ± 0.14 a	0.24 ± 0.07 c	0.51 ± 0.03 a	0.22 a
TGO500	1.13 ± 0.65 a	1.28 ± 0.28 b	0.17 ± 0.01 b	0.46 a
TGO800	nd	4.92 ± 0.34 a	0.29 ± 0.17 c	nd

Table A.2. EC_{50} values of ARGO and annealed GO at different temperatures, for *E. coli* after 3 hours of exposure in 0.9% NaCl. The R^2 of the sigmoidal fit used for the dose-response curve is given for all materials. Different letters represent statistical significance between materials at $p \leq 0.05$.

Samples	EC_{50} (µg/mL)	R^2
ARGO	183 ± 33.9 a	0.95
TGO200	143 ± 24.8 b	0.95
TGO500	127 ± 11.0 b	0.98
TGO800	86.3 ± 28.9 c	0.96

Table A.3. Statistical data and parameters for ARGO, TGO200, TGO500, and TGO800 after Sigmoidal dose-response fit. Calculations were done using average or individual data points for each material using GO concentrations from 0 to 500 µg/mL after a 3h exposure using *E. coli*.

		ARGO		TGO200		TGO500		TGO800	
		Average	Individual	Average	Individual	Average	Individual	Average	Individual
Statistics	Number of Points	7	60	6	49	6	53	6	72
	Degrees of Freedom	5	58	4	47	4	51	4	70
	Reduced Chi-Square	0.163	2331.3	0.129	357.4	0.081	285.6	0.936	280.7
	Residual Sum of Squares	0.813	135216.9	0.516	16799.5	0.323	14566.9	3.743	19652.9
	R-Square (COD)	0.955		0.958		0.988		0.971	
	Adj. R-Square	0.946	0.196	0.948	0.61	0.985	0.754	0.964	0.745
	Fit Status	100%	100%	100%	100%	100%	100%	100%	100%
Parameters	A1	0 ± 0	0 ± 0	0 ± 0	0 ± 0	0 ± 0	0 ± 0	0 ± 0	0 ± 0
	A2	100 ± 0	100 ± 0	100 ± 0	100 ± 0	100 ± 0	100 ± 0	100 ± 0	100 ± 0
	LOGx0	2.26 ± 0.08	2.29 ± 0.17	2.15 ± 0.08	2.21 ± 0.08	2.10 ± 0.04	2.09 ± 0.05	1.94 ± 0.14	1.97 ± 0.05
	p	-2.04 ± 0.51	-0.78 ± 0.38	-0.85 ± 0.13	-0.79 ± 0.15	-1.22 ± 0.12	-1.16 ± 0.18	-1.37 ± 0.35	-0.96 ± 0.12
	span	100 ± 0	100	100 ± 0	100	100 ± 0	100	100 ± 0	100
	EC_{20}	360 ± 56.1	666	729 ± 225	959	394 ± 51.9	403	237 ± 57.5	395
	EC_{50}	183 ± 33.8	193	143 ± 24.8	164	127 ± 11.0	122	86.3 ± 28.9	93.3
	EC_{80}	92.6 ± 29.5	56.2	27.9 ± 8.36	28.1	40.7 ± 5.98	37.2	31.5 ± 17.2	22

Table A.4. Dye fluorescence in percent out of control of SYTO9, PI, FDA, BODIPY, and ROS after a 3h exposure of GO to E.coli using their respective EC_{50}. A 5 mM $CuCl_2$ was used as a positive control depicted as (+) whereas the negative control (Ctrl) had no GO. Data is shown as an average ± standard deviation of three independent experiments with triplicate samples. Different letters indicate statistical differences between materials at $p \leq 0.05$ (n=9).

Material	FDA	BODIPY	ROS
+	83.7 ± 10.1 b	93.4 ± 2.26 c	119 ± 9.56 b
Ctrl	100 ± 9.11 b	100 ± 2.19 a	100 ± 4.76 d
ARGO	85.8 ± 3.93 b	97.9 ± 2.28 ab	158 ± 18.7 a
TGO200	97.6 ± 8.46 b	96.2 ± 2.67 bc	101 ± 4.30 cd
TGO500	130 ± 22.5 a	97.6 ± 2.97 ab	114 ± 3.60 b
TGO800	142 ± 26.1 a	96.82 ± 2.57 b	113 ± 7.61 bc

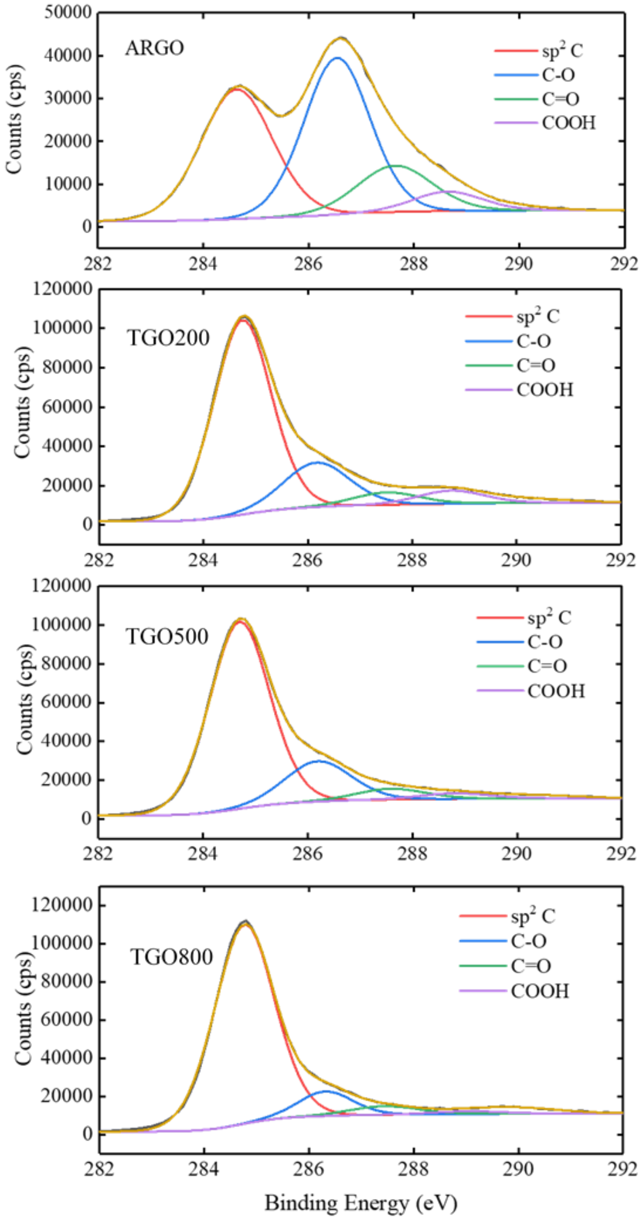

Figure A.1. Deconvolution of C1s resulting in four peaks approximately located at binding energies of 284.8, 286.3, 287.5, and 288.8 eV which are assigned to single and double carbon bonds (sp^2 C), epoxide and hydroxyl (C-O), carbonyl (C=O), and carboxylate (COOH) functional groups.

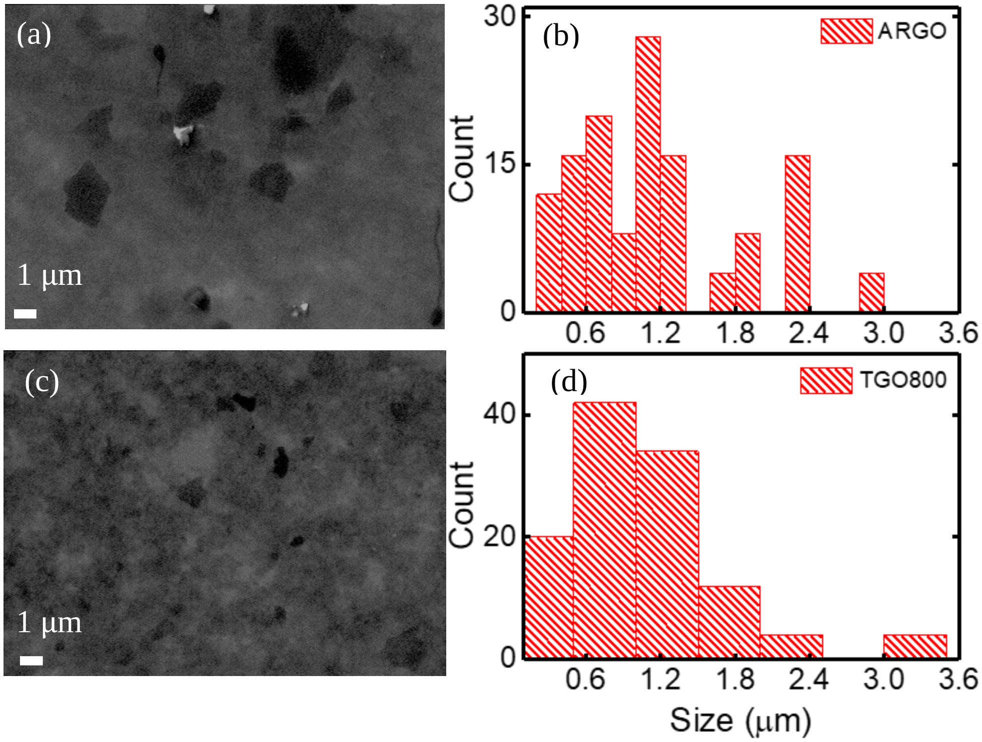

Figure A.2. SEM micrographs and histogram to determine the lateral size of each sample by counting >100 sheets of (a-b) ARGO drop-casted on a clean silicon wafer and (c-d) TGO800 drop-casted on a clean silicon wafer.

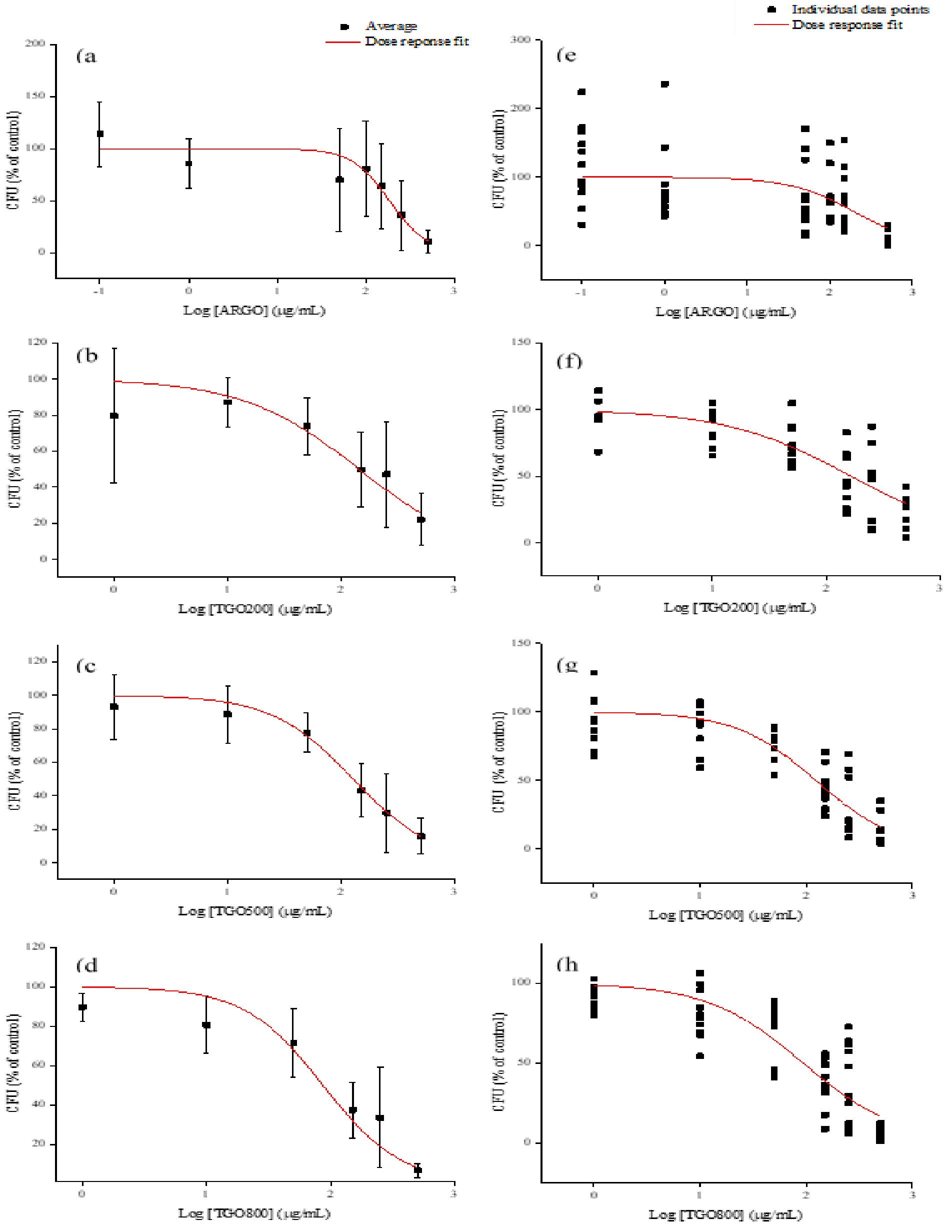

Figure A.3. Sigmoidal fit of dose-response curves of ARGO, TGO200, TGO500 and TGO800. Figures (a-d) represent average data points of three independent experiments and (e-g) represent individual data points.

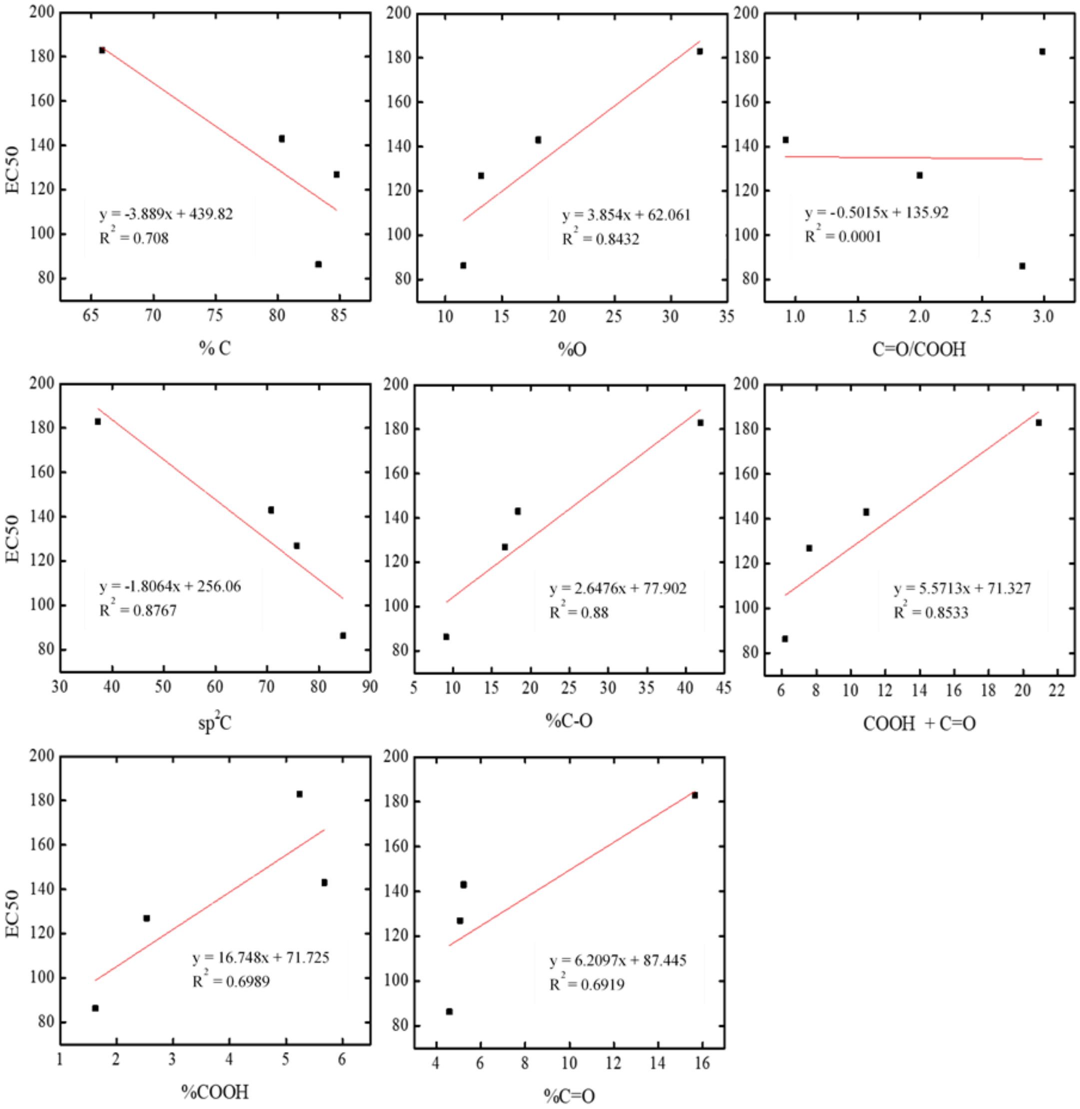

Figure A.4. Linear fit of EC_{50} values for ARGO and annealed TGOs with respect to oxygen functional groups according to the XPS data.

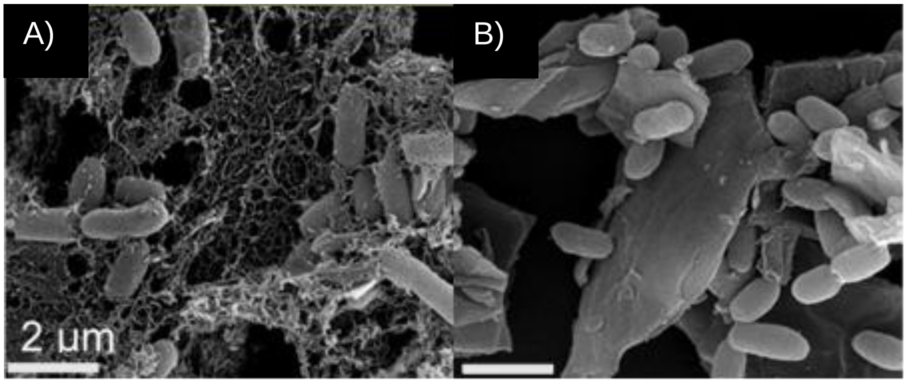

F**igure A.5.** Representative SEM images of *E. coli* cells after 3 h of exposure to 250 µg/mL A) ARGO and B)TGO800, respectively.

APPENDIX B

A MULTISPECIES ANALYSIS OF THE RELATIONSHIP BETWEEN OXYGEN CONTENT AND TOXICITY IN GRAPHENE OXIDE

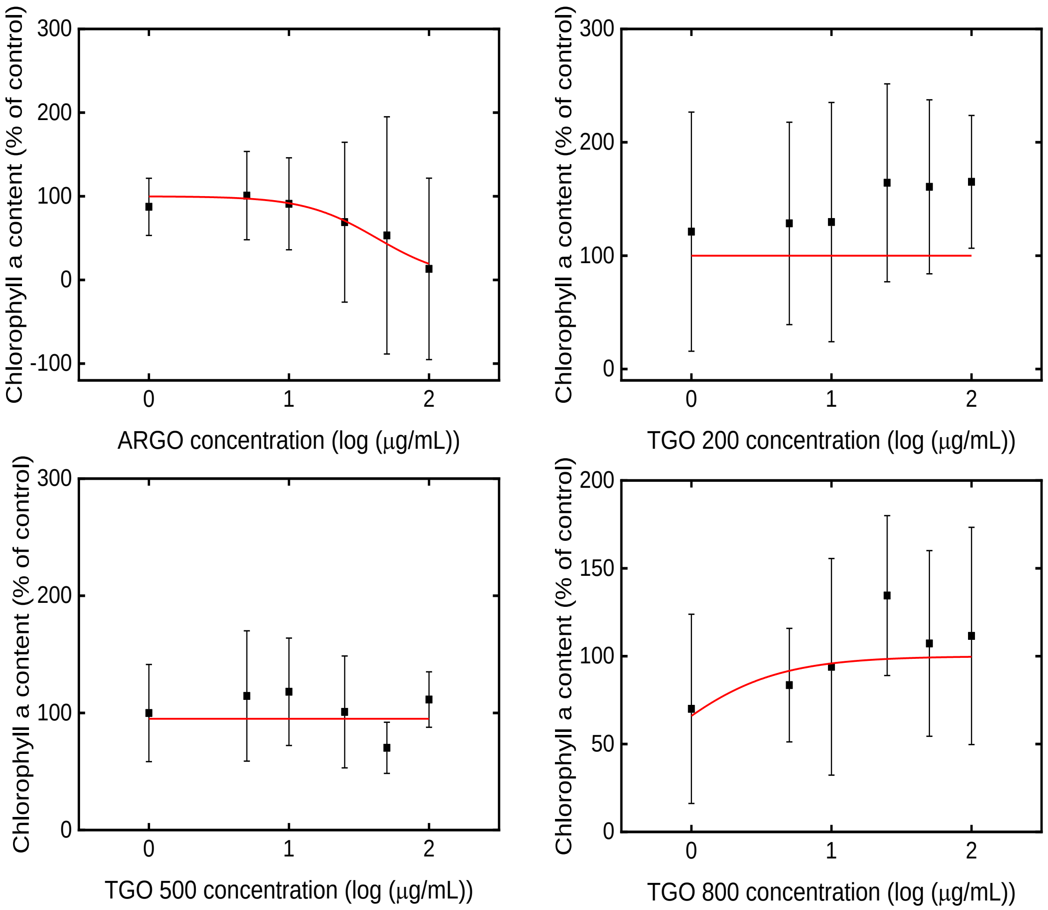

Figure B.1. Dose response curves of *S. obliquus* after exposure to GBNMs at different concentrations after 96h (n=9). A sigmoidal fit was conducted on each dose-response curve but only ARGO had a successful fit and a calculated EC_{50} concentration.

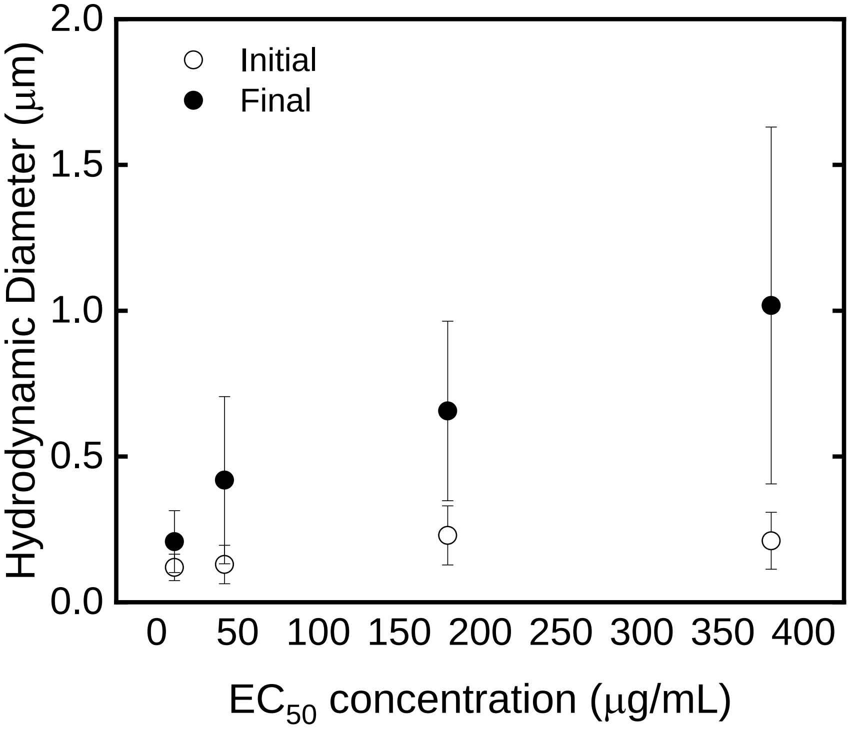

Figure B.2. Relationship between GBNMs' hydrodynamic diameter and EC_{50} concentration after the initial and final aggregation measurements for each media. The ARGO EC_{50} concentrations used were 11, 42, 180, and 380 µg/mL for *M. aeruginosa*, *S. obliquus*, *E. coli*, and *D. magna*, respectively. Data is shown as average ± standard deviation of three measurements.

Table B.1. Compiled literature comparing graphene-based nanomaterials' characteristics, experimental conditions, and toxicity effects to *Escherichia coli*, *Daphnia magna*, *Scenedesmus obliquus*, and *Microcystis aeruginosa*.

	Organism	Material	C/O	Another characteristic	ime of exposure (h	C_{50} (mg/L	Other toxicity endpoint	Reference
Bacteria	*E. coli*	GO	2-4*	D/G ratio: 1	2	100		287
	E. coli	rGO		D/G ratio: 1.9	2	100		287
	E. coli	GO	2-4*	Thickness: 1.1nm, 1.0 nm	2		98.5% viability loss at 85 mg/L**	288
	E. coli	rGO		Thickness: 1.1nm, 1.0 nm	2		90% viability loss at 85 mg/L**	288
	E. coli	GO	2-4*	D/G ratio: 1.36	2	30		289
	E. coli	rGO			2	40		289
	E. coli	GO	5.1		2	5		56
	E. coli	GO	2-4*	Size: 0.01 μm^2; D/G ratio: 1.03	3		20% viability loss at 200 mg/L**	15
	E. coli	GO	2-4*		24		MIC = 100 mg/L	290
	E. coli	GO	2-4*	D/G ratio: 0.92	48		65% viability loss at 65 mg/L	57
	E. coli	GO	2-4*		3	38		86
	E. coli	GO	1.9		12		MIC = 35 mg/L	291
	E. coli	GO	2-4*		2		20% viability loss at 100 mg/L	292
	E. coli	GO	2-4*		2.5		15% viability loss at 5 mg/L	293
	E. coli	GO	2.23		3		25% viability loss at 100 mg/L	107
	E. coli	GO	2-4*	Size: 205 µm; Thickness: 1 nm	2.5	25		294
	E. coli	GO	2	Thickness: 1.08 nm	3		75% inhibition at 50 mg/mL	92
	E. coli	dfGO	3.1	Thickness: 3.09 nm	3	50		92
	E. coli	GO	2	Size: 1 µm	3	183		295
	E. coli	TGO200	4.4	Size: 1.1 µm	3	143		295
	E. coli	TGO500	6.5	Size: 1.1 µm	3	127		295
	E. coli	TGO800	7.1	Size: 1.1 µm	3	86.3		295
Invertebrate	*D. magna*	TPGO	2.44		24, 48		No effect at 200 mg/L	296
	D. magna	GO	2.11	D/G ratio: 1.04	96	0.58		297
	D. magna	GO	2-4*	D/G ratio: 1.02; Size: 1108 nm	48	84.3		105
	D. magna	GO	3.27	Size: 0.9-5.2 µm; Thickness: 0.72 nm	48	150.8		131
	D. magna	GO	1.2		72	44.3	LC_{50} = 45.4 mg/L	118
	D. magna	GO-PEG	2-4*		48		No effect at 1 mg/L	117
	D. magna	GO	2.4	D-G ratio: 1.3; Size: 1.1 µm; Thickness: 1.02 nm	48	75	LC_{50} = 145 mg/L	119
	D. magna	GO	2-4*	Thickness: 1.0-1.77 nm	72			298
	D. magna	rGO	8.33		48		20% immobilization at 30 mg/L	299
	D. magna	GO	2-4*	Size: 0.5-3 µm Thickness: 0.55-1.20 nm	48	21		300
	D. magna	GO	2-4*		24	.18 (MHF); 0.31 (HF		301
	D. magna	GO	2-4*		48		No effect at 100 mg/L	302
	D. magna	GO	2.5	Size: 1 µm	48	383		This study
	D. magna	TGO200	4.7	Size: 1.1 µm	48	187		This study
	D. magna	TGO500	7.5	Size: 1.1 µm	48	320		This study
	D. magna	TGO800	12	Size: 1.1 µm	48	263		This study

Algae/ Cyanobacteria	*S. obliquus*	GO	2-4*	D/G ratio: 1.02; Size: 1108 nm	72	20.6		105
	S. obliquus	GO	2-4*	Size: 0.5-3 µm; Thickness: 0.55-1.20 nm	96	11		105
	S. obliquus	GO	2	Size: 3-8 µm; Thickness: 1.34 nm	96	10		142
	S. obliquus	rGO	2.8	Size: 0.2-5 µm; Thickness: 0.5-3 nm	72	148		116
	S. obliquus	GO	2.1	Size: 1-10 µm; Thickness: 0.7 nm	96	21.2		303
	S. obliquus	G	-	Size: 0.5-2 µm; Thickness: 0.8-1.2 nm	96	8.2		304
	S. obliquus	GO	2-4*	Size: 0.5-5 µm; Thickness: 0.8-1.2 nm	96	20.6		304
	S. obliquus	GO	2		96	42.4		This study
	S. obliquus	TGO200	4.6		96		EC_{50} of the TGO200 was not reached at 100 mg/L	This study
	S. obliquus	TGO500	7.6		96		EC_{50} of the TGO500 was not reached at 100 mg/L	This study
	S. obliquus	TGO800	12		96		EC_{50} of the TGO800 was not reached at 100 mg/L	This study
	M. aeruginosa	GO	2	Size: 3-8 µm; Thickness: 1.34 nm	96		35% growth inhibition at 10 mg/L	142
	M. aeruginosa	GO	2-4*	Size: 0.5-5 µm; Thickness: 0.8-1.2 nm	96		20% chl-*a* reduction at 50 mg/L	305
	M. aeruginosa	GO	2		96	52.3		151
	M. aeruginosa	GO	2	Size: 1.0 µm	96	11.1		This study
	M. aeruginosa	TGO200	4.6	Size: 1.1 µm	96	16.3		This study
	M. aeruginosa	TGO500	7.6	Size: 1.1 µm	96	126		This study
	M. aeruginosa	TGO800	12	Size: 1.1 µm	96		EC_{50} of TGO800 was not reached at 100 mg/L	This study

Abbreviations:

E. coli: Escherichia coli
D. magna: Daphnia magna
S. obliquus: Scenedesmus obliquus
M. aeruginosa: Microcystis aeruginosa
G: graphene
GO: graphene oxide
rGO: reduced graphene oxide
dfGO: debris-free graphene oxide
TGO: thermally-annealed graphene oxide
TPGO: thermal and pH dual-sensitive graphene oxide
PEG-GO: pegylated graphene oxide
MHF: moderately hard freshwater
HF: hard freshwater
C/O: carbon to oxygen ratio
EC_{50}: Effective concentration at 50%
MIC: Minimum inhibitory concentration

* an estimated C/O value between 2-4 was used for GO prepared using the Modified Hummers method and a value of 8-246 for rGO [12,306]

**Cell viability tested at only one concentration.

Table B.2. Compiled XPS data representing the atomic percent of the carbon and oxygen content and relative atomic percentage of carbon-oxygen functional groups determined from the component fitting of the C 1s envelope for all GBNMs. A new batch was synthesized per species (n=3) and three measurements were done per material for each batch.

	Material	%C	%O	%C-C/C-H	%C-O	%C=O	%COOH
Bacteria	ARGO	65.8 ± 0.80	32.5 ± 0.54	37.2 ± 1.14	41.9 ± 0.66	15.7 ± 2.09	5.24 ± 0.29
	TGO200	80.4 ± 0.21	18.2 ± 0.10	70.8 ± 0.01	18.3 ± 0.30	5.22 ± 0.08	5.68 ± 0.23
	TGO500	84.8 ± 1.39	13.2 ± 1.09	75.7 ± 1.43	16.7 ± 1.62	5.06 ± 0.18	2.53 ± 0.01
	TGO800	83.3 ± 0.44	11.6 ± 0.18	84.7 ± 0.22	9.19 ± 0.36	4.58 ± 0.37	1.62 ± 0.24
Algae/ Cyanobacteria	ARGO	66.1 ± 0.78	32.8 ± 0.67	45.3 ± 1.82	35.8 ± 2.16	13.8 ± 0.77	5.06 ± 0.51
	TGO200	81.7 ± 0.51	17.6 ± 0.25	73.8 ± 0.63	15.0 ± 0.09	5.81 ± 0.31	5.40 ± 0.45
	TGO500	88.4 ± 0.33	11.6 ± 0.33	80.3 ± 0.44	11.8 ± 0.58	5.53 ± 0.32	2.44 ± 0.12
	TGO800	91.5 ± 1.27	7.89 ± 1.11	86.7 ± 2.53	8.18 ± 2.64	3.53 ± 0.14	1.60 ± 0.44
Invertebrate	ARGO	70.8 ± 1.82	28.0 ± 2.20	55.5 ± 2.84	26.5 ± 4.36	12.9 ± 1.23	5.05 ± 0.30
	TGO200	82.0 ± 0.42	17.4 ± 0.38	75.1 ± 0.91	13.9 ± 1.27	6.16 ± 0.24	4.90 ± 0.45
	TGO500	87.8 ± 1.49	11.8 ± 0.77	79.9 ± 0.36	12.1 ± 0.50	5.38 ± 0.25	2.64 ± 0.12
	TGO800	90.2 ± 0.77	7.54 ± 0.60	85.1 ± 0.48	9.75 ± 0.41	3.67 ± 0.09	1.49 ± 0.05

Table B.3. Compiled XPS data representing the relative atomic percent of trace elements found in GBNMs. Trace amounts of impurities were also found and shown as atomic percent of sulfur, nitrogen, sodium, and calcium. A new batch was synthesized per species (n=3) and three measurements were done per material for each batch.

	Material	S%	N%	Na%	Ca%
Bacteria	ARGO	0.52 ± 0.04	0.76 ± 0.15	0.23 ± 0.07	nd
	TGO200	0.51 ± 0.03	0.59 ± 0.14	0.24 ± 0.07	nd
	TGO500	0.17 ± 0.01	1.13 ± 0.65	1.28 ± 0.28	nd
	TGO800	0.29 ± 0.17	nd	4.92 ± 0.34	nd
Algae	ARGO	1.04 ± 0.11	nd	nd	nd
	TGO200	0.54 ± 0.04	0.52 ± 0	nd	nd
	TGO500	nd	nd	nd	nd
	TGO800	nd	0.63 ± 0	0.22 ± 0.05	nd
Invertebrate	ARGO	0.79 ± 0.05	nd	nd	0.64 ± 0.12
	TGO200	0.58 ± 0.06	nd	nd	nd
	TGO500	0.62 ± 0.01	nd	nd	nd
	TGO800	1.16 ± 0.12	nd	0.39 ± 0.08	0.62 ± 0.05

nd = not detected

Table B.4. Responses of *D. magna* immobilization after exposure to GBNMs at different concentrations after 48h (n=3). The EC_{50} concentrations were calculated using the Trimmed Spearman-Karber method. Data is shown as mean ± standard deviation.

Material:	**ARGO**	**TGO200**	**TGO500**	**TGO800**
Concentration (mg/L)	Mean immobilization (%)	Mean immobilization (%)	Mean immobilization (%)	Mean immobilization (%)
12.5	0.0 ± 0.0	0.0 ± 0.0	0.0 ± 0.0	0.0 ± 0.0
25	1.7 ± 2.9	8.3 ± 2.9	0.0 ± 0.0	8.3 ± 2.9
50	6.7 ± 2.9	13.3 ± 2.9	6.7 ± 2.9	11.7 ± 2.9
100	15.0 ± 5.0	25.0 ± 10.0	13.3 ± 2.9	16.7 ± 2.9
200	23.3 ± 7.6	38.3 ± 10.4	23.3 ± 2.9	28.3 ± 7.6
400	51.7 ± 2.9	81.7 ±17.6	63.3 ± 5.8	78.3 ± 2.9
EC_{50}	383 ± 29.9	187 ± 18.3	320 ± 14.4	263 ± 17.0

Table B.5. Chemical composition and concentrations to prepare stock solutions for each media. A 0.9% NaCl media was used for bacteria experiments, ISO media for invertebrate studies (D. magna) according to the International Organization for Standardization, and Bold's Basal Media (BBM) for green alga and cyanobacteria studies. All medias were prepared in DI water and their pH was adjusted with HCl or KOH as required. Aggregation studies were done using the GBNMs suspended in each media, with no organisms present.

0.9% NaCl		ISO*		BBM**	
Chemical	Concentration (g/L)	Chemical	Concentration (g/L)	Chemical	Concentration (g/L)
NaCl	9.0	$CaCl_2{\bullet}2H_2O$	11.8	KH_2PO_4	17.5
		$MgSO_4{\bullet}7H_2O$	4.93	$CaCl_2{\bullet}2H_2O$	25
		$NaHCO_3$	2.59	$MgSO_4{\bullet}7H_2O$	75
		KCl	0.23	$NaNO_3$	250
				K_2HPO_4	75
				NaCl	25
				$Na_2EDTA{\bullet}2H_2O^{a}$	
				$FeSO_4{\bullet}7H_2O^{b}$	
				Trace metal solution (TMS)^{c}	(see below)
				H_3BO_3	11.5 g/L
				TMS^{c}	
				H_3BO_3	2.86
				$MnCl_2{\bullet}4H_2O$	1.81
				$ZnSO_4{\bullet}7H_2O$	0.22
				$Na_2MoO_4{\bullet}2H_2O$	0.39
				$CuSO_4{\bullet}5H_2O$	0.08
				$Co(NO_3)_2{\bullet}6H_2O$	0.05

*Mix 25 mL of each of the four stock solutions and make up to 1 L with DI water.

**Mix 1 mL of each of the stock solutions (10 mL for KH_2PO_4) in the order shown above to avoid salt precipitation. Make up to 1 L with DI water. Adjust pH and then autoclave.

[a] The $Na_2EDTA{\bullet}2H_2O$ solution was prepared in 1 L of a KOH (6.2 g/L).

[b] The $FeSO_4{\bullet}7H_2O$ solution was prepared in 1 L of concentrated H_2SO_4 (1 mL/L).

[c] The Trace Metal Solution (TMS) was prepared separately, and all salts were added to 1 L of water. Then, 1 mL of the TMS was added to 1 L of BBM media.

Table B.6. Solution chemistry characteristics of the different media. Bacteria experiments were done in 0.9% NaCl, alga experiments in BBM and invertebrates' studies were done according to the International Organization for Standardization (ISO).

Media	pH	Ionic Strength (mM)	Divalent Cations (mM)	Monovalent Cations (mM)
0.9% NaCl	7.0	147.90	0.00	154.00
BBM	6.8	7.10	0.30	5.68
ISO	7.8	6.74	2.00	0.68

APPENDIX C

DECOUPLING STRUCTURE AND SURFACE CHEMISTRY IMPACTS OF GRAPHENE/BASED EPOXY NANOCOMPOSITES AFTER ULTRAVIOLET LIGHT DEGRADATION

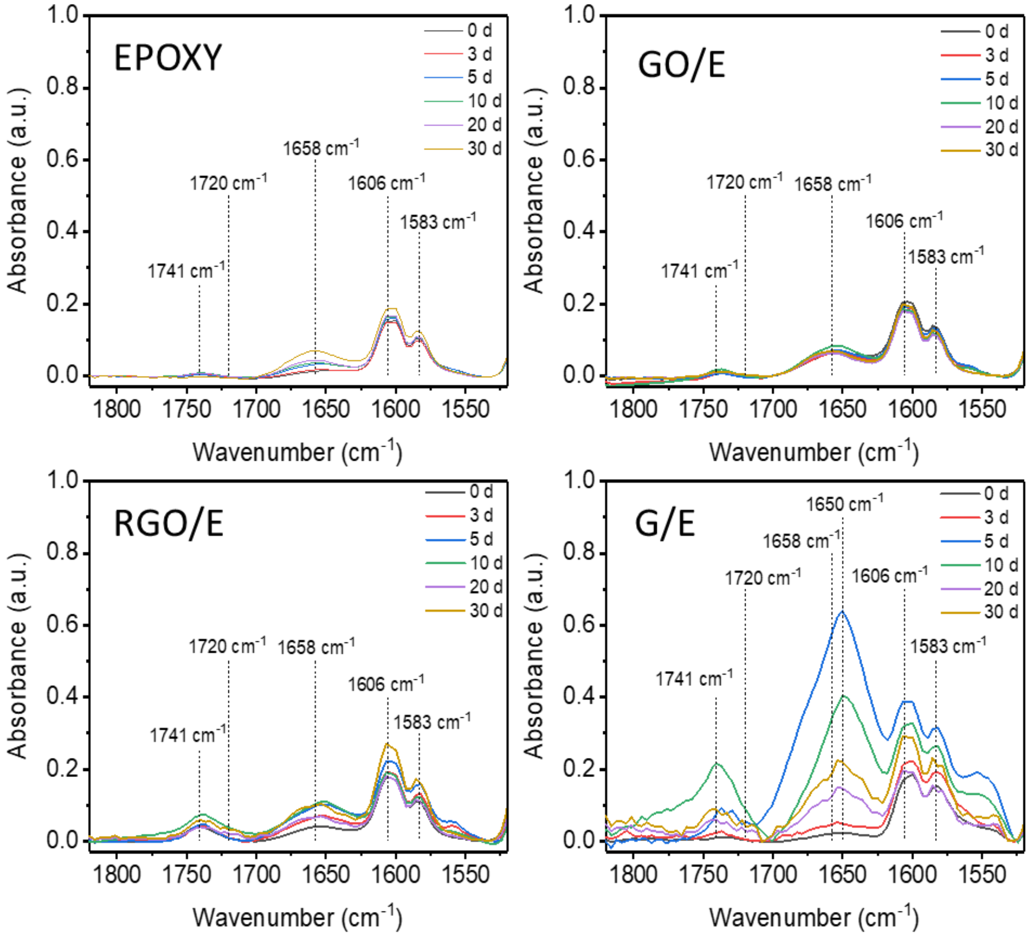

Figure C.1. The carbonyl region in the FTIR Spectrum of neat Epoxy and GB/E PNCs at different time points of humid dark exposure.

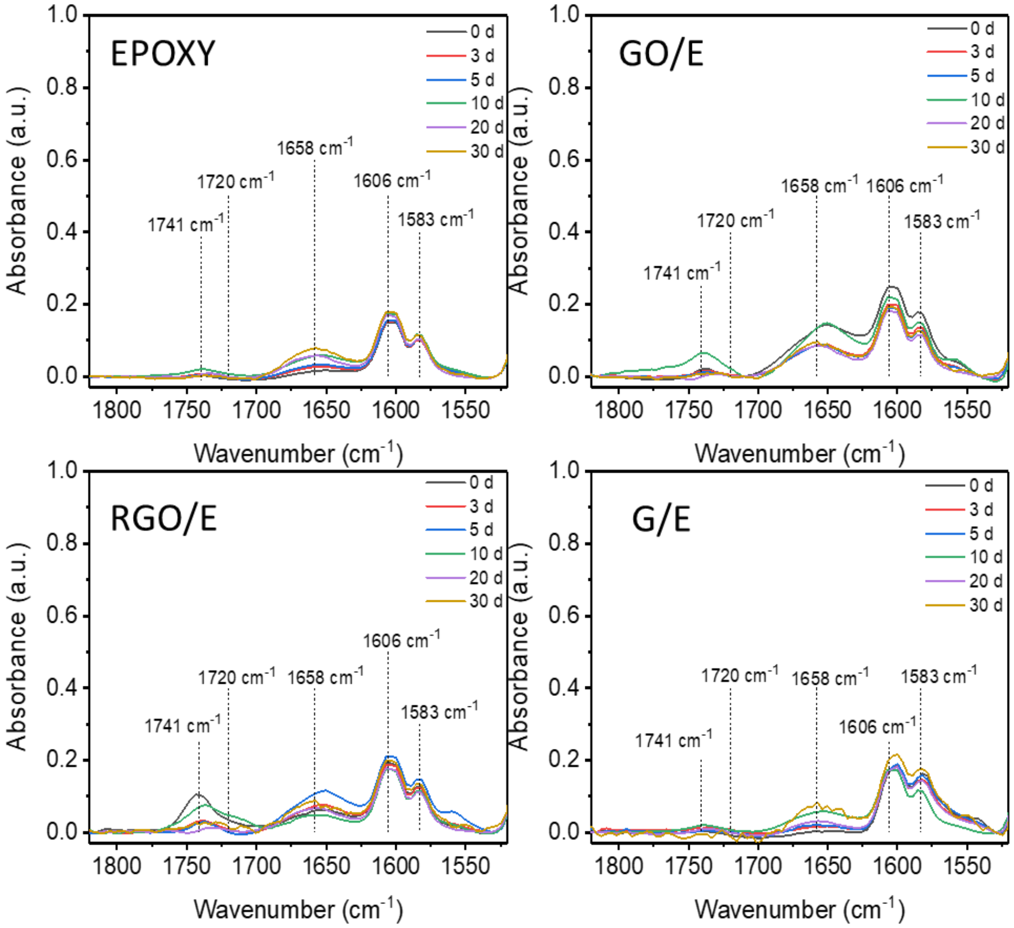

Figure C.2. The carbonyl region in the FTIR Spectrum of neat Epoxy and GB/E PNCs at different time points of dry dark exposure.

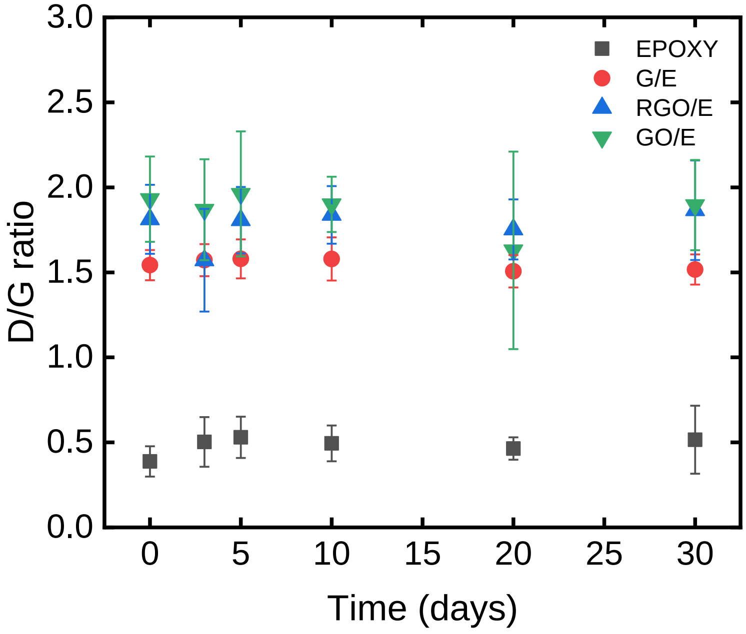

Figure C.3. The D band (1311 cm^{-1}) to G band (1602 cm^{-1}) intensity ratio at different time points of dry dark exposure. Each data point represents the average and standard deviation of three replicate specimens, with measurements of four areas per replicate specimen.

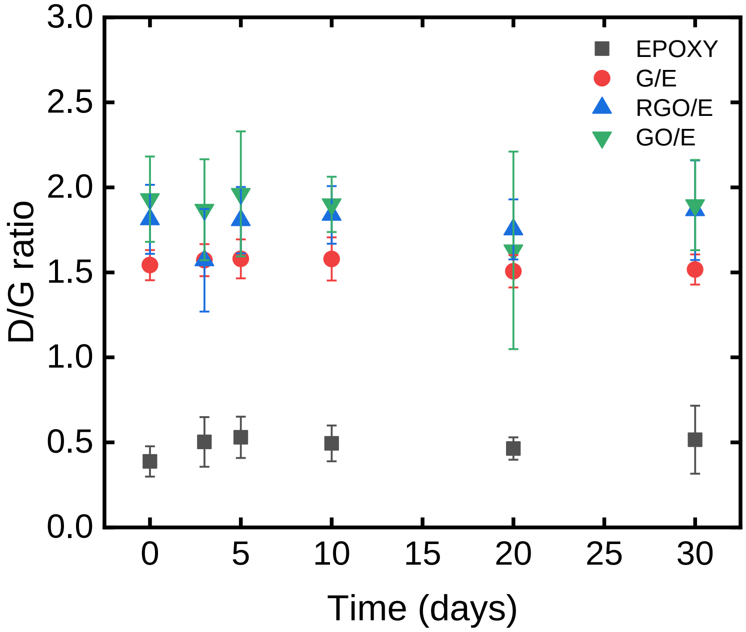

Figure C.4. The D band (1311 cm^{-1}) to G band (1602 cm^{-1}) intensity ratio at different time points of humid dark exposure. Each data point represents the average and standard deviation of three replicate specimens, with measurements of four areas per replicate specimen.

APPENDIX D

INCREASED BROMIDE REMOVAL IN GRAPHENE-SILVER NANOCOMPOSITES: ROLE OF PARTICLE SIZE AND CARBON STRUCTURE

Table D.1. Fresh water composition. The recipe was obtained from the Nano-Enabled Water Treatment (NEWT) Engineering Research Center.

General Parameters	**Specification**	
Water Source	De-ionized water (conductivity < 1 µS/cm)	
pH adjusted with HCl	7.5 ± 0.25	
Temperature	20 ± 2.5 °C	
Constituents	***Concentration (mg/L)***	***Concentration (mM)***
Bicarbonate (HCO_{3-}, initial)	183	3.0
Calcium (Ca^{2+})	40	1.0
Chloride (Cl^-)	71	2.0
Fluoride (F^-)	1.0	0.053
Magnesium (Mg^{2+})	12	0.50
Nitrate (NO_{3-})	8.9 (2.0 as N)	0.14
Phosphate (PO_4^{3-})	0.12 (0.04 as P)	0.0013
Silica (SiO_2)	20 as SiO_2	0.33
Sodium (Na^+)	89	3.86
Sulfate ($SO4^{2-}$)	48	0.50
Total Dissolved Solids (TDS)	478	-
Ionic Strength	-	8.5

Table D.2. Visual Minteq calculations for freshwater constituents at pH 7.5 modeling the behavior of silver and bromide in fresh waters.

Component	% dissolved	% precipitated
Ag^+	0.15	99.85
Br^-	100	0
Cl^-	81.478	18.522
SO_4^{2-}	100	0

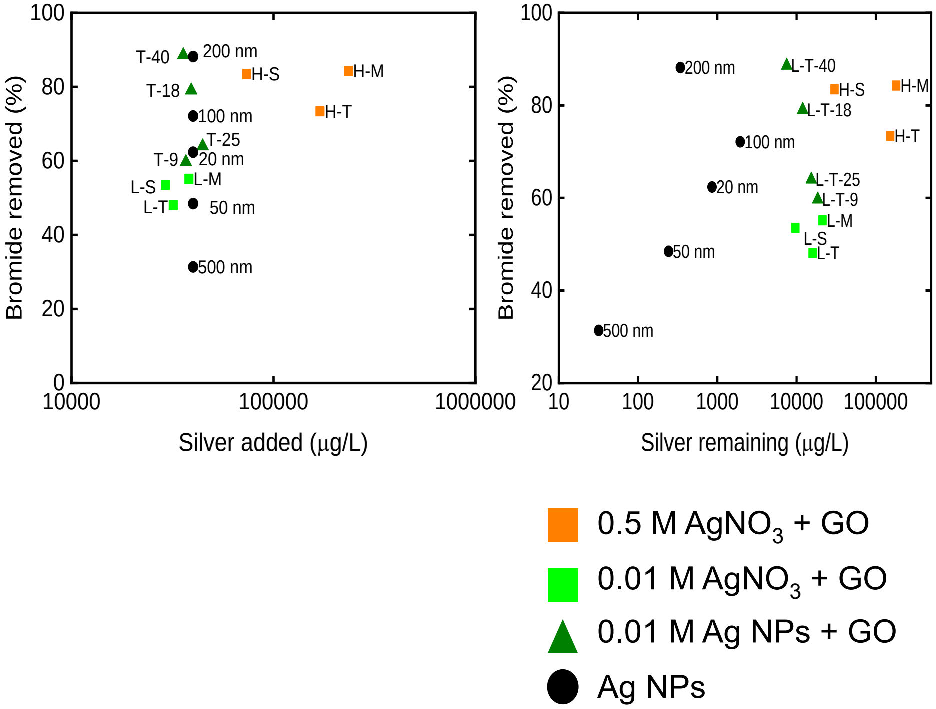

Figure D.1. Silver concentration before and after Br$^-$ removal for the different types of GO-Ag and Ag NPs without coagulation-flocculation-sedimentation.

APPENDIX E

PUBLICATIONS

First author:

1) **Barrios, A.C.**, Carrillo, D., Waag, T.R., Bi, Y., Islam, R., Perreault, F. **2020**. Prolonging the antimicrobial activity of nanosilver-coated membranes through partial sulfidation. *Environ. Science: Nano* in July 2020.

2) Montenegro-Ayo, R.[1], **Barrios, A.C.[1]**, Mondal, I., Bhagat, K., Morales-Guerrero, J.C., Abbaszadegan, M., Westerhoff, P., Perreault, F., Garcia-Segura, S. **2020**. Portable point-of-use photoelectrocatalytic device provides rapid water disinfection. *Sci. Total Environ.* 737, 140044.

3) **Barrios, A.C.,** Wang, Y., Gilbertson, L.M., Perreault, F. **2019**. Structure-toxicity relationships of graphene oxide: Role of surface chemistry on the mechanisms of interaction with bacteria. *Environ. Sci. Technol*. 53 (24), 14679-14687.

4) **Barrios, A.C.,** Cahue, P.Y., Wang, Y., Puerrari, R.C., Gilbertson, L.M., Gerson Matias, W., Pedroso Melegari, S., Perreault, F. **2021**. A multispecies analysis of the relationship between oxygen content and toxicity in graphene oxide. Submitted to *Environ. Sci: Nano* in December 2020. Under revision.

5) **Barrios, A.C.**, Goodwin, D., Perreault, F. **2021**. Decoupling graphene structure and surface chemistry impacts on ultraviolet degradation of graphene-based/epoxy nanocomposites. To be submitted to *Carbon*.

6) **Barrios, A.C.,** Kidd, J., Apul, O., Westerhoff, P., Perreault, F. **2021**. Silver impregnated graphene oxide for bromide removal from surface water: ionic silver versus nano-silver. To be submitted to *Environ. Sci. Technol*.

Other publications:

1) Goodwin, D., Shen, S., Lyu, Y., Lankone, R., **Barrios A.C.,** Kabir, S., Perreault, F., Wohlleben, W., Nguyen, T., Sung, L. **2020**. Graphene/Polymer nanocomposite degradation by ultraviolet light: the effects of graphene nanofillers and their potential for release. *Polymer Degradation and Stability.*, 182, 109365.

2) Cruces, E., **Barrios, A.C.**, Cahue, Y.P., Januszewski, B., Gilbertson, L.M., Perreault, F. **2020**. Similar toxicity mechanisms between graphene oxide and oxidized multi-walled carbon nanotubes in *Microcystis aeruginosa*. *Chemosphere*, 265, 129137.

3) Rajwade, K., **Barrios, A.C.**, Garcia-Segura S., Perreault, F. **2020**. Pore wetting in membrane distillation treatment of municipal wastewater desalination brine and its mitigation by foam fractionation. *Chemosphere*, 127214.

4) Rice, D., Ghadimi, S.J., **Barrios, A.C.**, Henry, S., Walker, S.W., Li, Q., Perreault, F. **2020**. Scaling resistance in nanophotonics-enabled solar membrane distillation. *Environ. Sci. Technol*., 54(4), 2548-2555.

5) Falinski, M.M., Turley, R.L., Kidd, L., Lounsbury, A.W., Lanzarini-Lopes, M., Backhaus, A., Rudel, H., Lane, M.K.M., Fausey, C.L., **Barrios, A.C.**, Loyo, J., Perreault, F., Walker, S., Stadler, L., Elimelech, M., Gardea-Torresdey, J.L., Westerhoff, P., Zimmerman, J.B. **2020**. Doing nano-enabled water treatment right: sustainability considerations from design and research through development and implementation. *Environ. Science: Nano*, 7 (11), 3255-3278.

6) Rice, D., **Barrios, A.C.,** Xiao, Z., Bogler, A., Bar-Zeev, E., Perreault, F. **2018**. Development of anti-biofouling feed spacers to improve performance of reverse osmosis modules. *Water Research*, 145, 599-607.

7) Zheng, X**., Barrios, A.C.**, Perreault, F., Yun, T.S., Jang, J. **2018**. Interfacial tension and contact angle in CO_2-water/nanofluid-quartz system. *Greenh. Gases* 8 (4), 734-746.

8) Kidd, J., **Barrios, A.C.,** Apul, O., Perreault F., Westerhoff, P. **2018**. Removal of bromide from surface water: A comparison between silver-impregnated graphene oxide and silver-impregnated powdered activated carbon. *Environ. Eng. Sci*., 35(9), 647-653.